



**UNIVERSIDAD DE CHILE**  
**FACULTAD DE CIENCIAS FISICAS Y MATEMATICAS**  
**DEPARTAMENTO DE GEOFISICA**

**ATMOSPHERIC FORCING OF THE SURFACE OCEAN OFF CENTRAL CHILE**

**TESIS PARA OPTAR AL GRADO DE DOCTORA EN**  
**CIENCIAS DE LA INGENIERÍA MENCIÓN FLUIDODINÁMICA**

**MARÍA CATALINA AGUIRRE GALAZ**

**PROFESOR GUIA:**  
RENÉ GARREAUD SALAZAR

**PROFESOR CO-GUIA**  
JOSÉ RUTLLANT COSTA

**MIEMBROS DE LA COMISION:**  
OSCAR PIZARRO ARRIAGADA  
ALDO TAMBURRINO TAVANTZIS

SANTIAGO DE CHILE  
JULIO 2012

## Resumen

En esta tesis se estudian los mecanismos físicos involucrados en el forzamiento atmosférico del océano superficial a escala estacional y sinóptica frente a Chile central. Para esto, se utilizaron observaciones disponibles (*in-situ* y derivadas de satélite) y simulaciones numéricas. Este trabajo está particularmente enfocado en el forzamiento del viento.

El ciclo estacional de la circulación superficial frente a Chile central fue analizada utilizando altimetría satelital y un modelo oceánico. Para evaluar el rol que cumple el rotor del esfuerzo del viento sobre la circulación se realizaron dos simulaciones idénticas excepto por el forzamiento del viento: la “simulación control” utilizó una climatología mensual del esfuerzo del viento y la “simulación sin rotor” utilizó un campo de esfuerzo similar pero con rotor nulo. Las corrientes superficiales observadas y simuladas (simulación control) mostraron un ciclo estacional importante y un flujo bien definido hacia el ecuador con una estructura de chorro. Esta corriente en chorro se desarrolla durante la primavera y el verano consistente con la presencia de un chorro atmosférico de baja altura. Al sur de Punta Lavapie (~37°S) la corriente superficial hacia el ecuador permanece junto a la costa, pero luego que el flujo pasa esta punta se separa de la costa convirtiéndose en un chorro oceánico. A diferencia de esto, en la “simulación sin rotor” la separación en Punta Lavapie no ocurre y el chorro oceánico no se observa, lo que evidencia la importancia del rotor del esfuerzo del viento en la dinámica de este flujo superficial. A pesar de que el transporte de Sverdrup integrado es similar al transporte simulado, la corriente en chorro oceánica no se localiza donde el rotor del esfuerzo del viento es máximo. Por el contrario, la posición del chorro sigue aproximadamente el contorno cero del rotor del esfuerzo del viento, el cual corresponde a la posición climatológica del eje del chorro atmosférico. Estos resultados ilustran la importancia de la surgencia/hundimiento que ocurre fuera de la costa asociadas al bombeo de Ekman, el cual inclina las isopícnas hacia arriba (abajo) al este (oeste) del chorro atmosférico, forzando un flujo oceánico hacia el norte a través de un balance de viento térmico.

Por otra parte, el efecto de la variabilidad sinóptica del viento y los flujos de calor sobre el océano superficial frente a Chile centro-sur fueron investigados utilizando un modelo oceánico. Este análisis se concentra durante el verano austral, cuando el viento regional experimenta una variabilidad sinóptica importante sobre una media favorable a la surgencia. Para evaluar la naturaleza y la magnitud de estos efectos, se realizaron tres simulaciones idénticas excepto por el forzamiento superficial: la *climatologica*, con esfuerzo del viento y flujos de calor climatológicos; la *parcialmente sinóptica*, con esfuerzo del viento diario y flujos de calor climatológicos; y la *completamente sinóptica*, con esfuerzos del viento y flujos de calor diarios. Las corrientes medias y la EKE geostrofica superficial no muestran importantes diferencias entre simulaciones, y ambas se ajustan a lo documentado para el Pacífico Sureste. Sin embargo, se observa mayor EKE ageostrofica en las simulaciones que consideran variabilidad sinóptica del esfuerzo del viento, impactando en la cantidad de EKE superficial total y la difusividad, particularmente al sur de Punta Lavapie, donde hay ausencia de corrientes importantes lo que implica bajos niveles de EKE geostrofica. El promedio de verano de la SST es similar en las simulaciones y se ajusta a las observaciones, pero la variabilidad de la SST a lo largo de la costa es mayor en las corridas que incluyen variabilidad sinóptica del esfuerzo del viento, lo que sugiere una respuesta más bien lineal del océano a los ciclos de intensificación y relajación del viento sur. Se encontró que la variabilidad de la SST costera no cambia significativamente cuando se incluyen flujos de calor diarios, indicando un rol prominente de los ciclos de surgencia. Sin embargo, en la región más alejada de la costa es necesario incluir la variabilidad sinóptica de los flujos de calor para obtener una variabilidad de la SST realista.

## Abstract

This thesis is concerned with the study of the physical mechanisms involved in the atmospheric forcing of the surface ocean at seasonal and synoptic scales off central Chile. In doing so, we have made use of available measurements (*in-situ* and satellite derived) and numerical simulations. We are particularly interested in the wind forcing.

The seasonal cycle of the near-surface circulation off central Chile was analyzed using satellite altimetry and an oceanic model. To evaluate the role of the wind-stress curl on the circulation we performed two identical simulations except for the wind forcing: the “control run” used long-term monthly mean wind-stress and the “no-curl run” used a similar wind-stress field, but without curl. The observed and modeled (control run) surface currents showed an important seasonal cycle and a well defined equatorward flow with a jet-like structure. This jet develops during spring and summer consistent with the presence of a low-level wind jet. South of Punta Lavapie ( $\sim 37^{\circ}\text{S}$ ) the equatorward surface current remains close to the coast, but after the flow passes this cape, it separates to become an offshore jet. In contrast, in the no-curl simulation the separation at Punta Lavapie is not observed and the offshore jet farther north is not present, evidencing the importance of the wind-stress curl on the dynamics of this flow. Although the offshore integrated Sverdrup transport was similar to the model transport, the offshore jet was not located where the wind stress curl was maximum. In contrast, the position of the jet followed approximately the zero wind stress curl, which corresponds to the climatological location of the low-level wind jet axis. These results illustrate the importance of the offshore upwelling/downwelling associated with the Ekman pumping, which tilts isopycnals upward (downward) toward the east (west) of the wind jet, forcing a northward flow through thermal wind balance.

On the other hand, the effect of the high frequency (synoptic) variability of wind and heat fluxes upon the surface ocean off south-central Chile is investigated using an ocean model. We focus our analysis in austral summer, when the regional wind experiences significant day-to-day variability superimposed on a mean, upwelling favorable flow. To evaluate the nature and magnitude of these effects, we performed three identical simulations except for the surface forcing: the *climatological*, with long-term monthly mean wind-stresses and heat fluxes; the *partial-synoptic*, with daily wind stresses and climatological heat fluxes; and the *full-synoptic*, with daily wind-stresses and daily fluxes. The mean currents and surface geostrophic EKE show no major differences between simulations, and both agree well with those documented for the Southeast Pacific. Nevertheless, more ageostrophic EKE is found in the simulations which include synoptic variability of wind-stresses, impacting the total surface EKE and diffusivities, particularly south of Punta Lavapie ( $\sim 37^{\circ}\text{S}$ ), where the lack of major currents implies low levels of geostrophic EKE. Summer mean SSTs are similar in simulations and agree with observations, but SST variability along the coast is larger in the runs including wind-stress synoptic variability, suggesting a rather linear response of the ocean to cycles of southerly wind strengthening and relaxation. We found that coastal SST variability does not change significantly when including daily heat fluxes, highlighting the prominent role of wind-driven upwelling cycles. In contrast, in the offshore region it is necessary to include synoptic variability in the heat fluxes to account for a realistic SST variability.

**Dedicada a mis Padres, Juan Pablo, Erick y Matilda**

## Acknowledgements

I gratefully thank my advisors, René Garreaud and José Rutllant, for their patience in guiding me and their confidence in my work. I would also like to thank Oscar Pizarro for sharing with me interesting discussions about ocean dynamics and for being always available to attend my questions. Thanks are also due to Aldo Tamburrino for their constructive comments and suggestions that improved this thesis.

My recognition also to several researchers and technicians from the University of Concepción (COPAS, PROFCE and DGEO) and to the Danish Centre for Earth Science Studies (DCESS, Denmark), who collected and processed the *in-situ* ocean current data used in this research. My warm thanks to everyone at the DGF-MET, in particular to Rodrigo Sanchez, for his key contribution in the model set up, and to my partners at the student's office for the pleasure to work there.

This research was made possible by the economic support from MECESUP UCH-0310 and CONICYT Doctoral Grants. I am also indebted to project ECOS-CONICYT for allowing me to visit the Laboratoire d'Études en Géophysique et Océanographie Spatiales (LEGOS, France) and to The South American Climate Change Consortium and Vicerrectoría de Asuntos Académicos, Universidad de Chile that supported an internship abroad at the College of Oceanic and Atmospheric Sciences of the Oregon State University (USA). Projects FONDECYT N° 1090791 and FONDECYT N°1090492 also contributed to support this study and associated publications.

Finally, special and warm thanks are due to my parents and my brother for their continuous support in this long time, and to my new family Erick and Matilda for encouraging me to complete this Ph. D thesis.

# Contents

<b>Introduction</b>	<b>1</b>
1.1. Mean field and variability of the surface wind off Chile	1
1.2. Eastern Boundary Current System Dynamics	3
1.3. Upper-ocean regional circulation in the Eastern South Pacific	6
1.4. Outline	7
<b>Methods</b>	<b>8</b>
2.1 Datasets and data processing	8
2.2 The Regional Ocean Model	12
2.3 Equations resolved by the Regional Ocean Model	13
2.4 Model Validation	14
<b>Seasonal dynamics of the near-surface alongshore flow off central Chile</b>	<b>20</b>
3.1 Introduction	20
3.2 Model setup	21
3.3 Seasonal variability of the upwelling and surface currents	21
3.4 Vertical structure of the coastal transition zone (CTZ) jet	26
3.5 The role of wind stress curl in the CTZ jet variability	28
3.6 Discussion	31
3.7 Conclusions	32
<b>Surface ocean response to synoptic-scale variability in wind stress and heat fluxes off south-central Chile</b>	<b>34</b>
4.1 Introduction	34
4.2. Model configuration and experimental setup	35
4.3. Inter-simulations comparison	36
4.3.1 Mean circulation	36
4.3.2. Eddy Kinetic Energy (EKE)	38

4.3.3. Lagrangian properties of the surface flow	40
4.3.4. Sea surface temperature	43
<b>4.4. Discussion</b>	<b>46</b>
<b>4.5. Conclusions</b>	<b>49</b>
<b>General conclusions and future work</b>	<b>51</b>
<b>References</b>	<b>53</b>

# Chapter 1

## Introduction

### 1.1. Mean field and variability of the surface wind off Chile

Major eastern boundary current systems are driven by predominant equatorward winds, which force upwelling of cold and nutrient-rich subsurface water near the coast, equatorward surface flows with a complex spatial and temporal structure, and a poleward undercurrent [e.g., Hill *et al.*, 1998]. The coastal upwelling along much of the eastern boundaries induces high primary productivity associated with the richest fisheries in the world. Seasonal changes in the wind field modulate the upwelling variability and the different surface and subsurface flows observed in these regions [Strub *et al.*, 1998]. In the vast region comprising the Peru-Chile Current system, the seasonal cycle of the wind shows contrasts between its northern and southern portions. In the northern region off Peru ( $\sim 5^\circ - 15^\circ\text{S}$ ) winds are upwelling favorable all year-round with maximum speeds in the austral winter (June, July and August) [Bakun and Nelson, 1991]. Off northern Chile ( $\sim 18^\circ\text{S}-28^\circ\text{S}$ ) upwelling winds also prevail throughout the year, but they are rather weak and stable, with very low synoptic and seasonal variability [Pizarro *et al.*, 1994]. In contrast, off central Chile ( $\sim 30^\circ - 40^\circ\text{S}$ ) winds show a large seasonal cycle (Figure 1.1). During austral winter, the Southeast Pacific Anticyclone and the westerly wind belt move northward, allowing the arrival of mid-latitude atmospheric disturbances to central Chile as far north as  $\sim 30^\circ\text{S}$ , which increase the frequency and magnitude of poleward winds [e.g., Fuenzalida, 1971; Saavedra and Foppiano, 1992]. Indeed, south of  $\sim 35^\circ\text{S}$  mean coastal winds are downwelling favorable during winter. During summer (December, January and February; DJF), the Southeast Pacific Anticyclone moves southward and upwelling winds are predominant down to  $\sim 40^\circ\text{S}$ . In this season, a synoptic low-level wind jet blowing northward is frequently observed between  $\sim 38^\circ$  and  $30^\circ\text{S}$  [Garreaud and Muñoz, 2005].

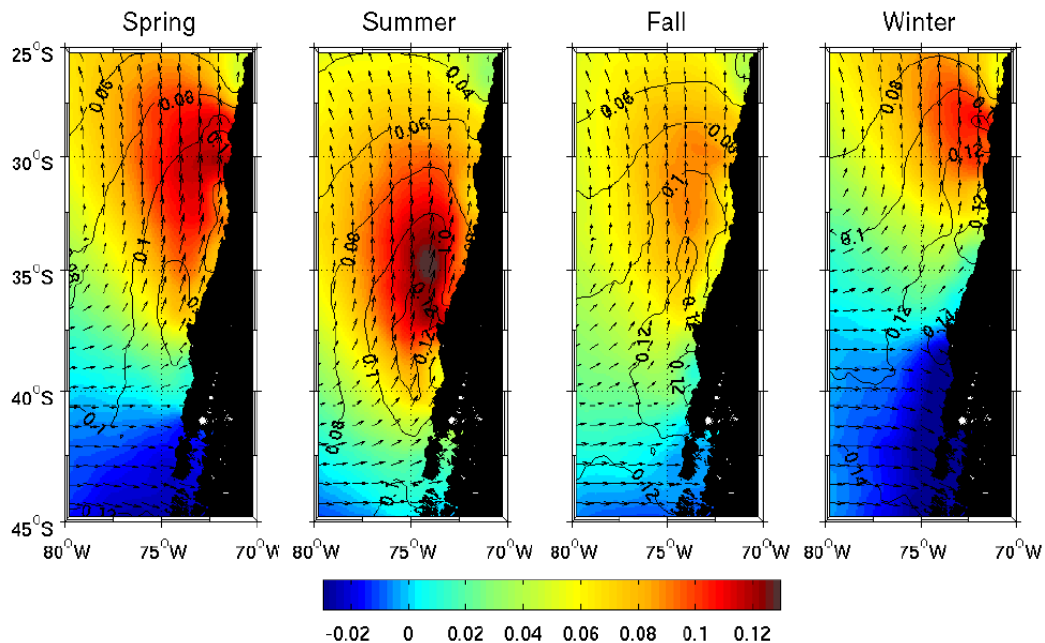


**Figure 1.1.** Climatology of the meridional wind stress (colors, in Pa), standard deviation of the meridional wind stress (contours) and wind stress vector (arrows) from QuikSCAT (2000 to 2007).



South of 35°S synoptic variability of the winds is very pronounced in winter –when stronger northerlies alternate with milder southerlies due to the passage of extratropical atmospheric disturbances. This high-frequency wind variability is still present in summer [e.g., *Sobarzo et al.*, 2010] due to the quasi-weekly occurrences of southerly atmospheric coastal jet events alternated with periods of weak southerlies or even northerly flow in connection with the passage of coastal lows [*Garreaud and Muñoz*, 2005; *Garreaud et al.*, 2002]. These jet events are characterized by a meridionally elongated maximum of surface southerly winds over 15 m s<sup>-1</sup> generally rooted in Punta Lavapie (Figure 1.2) and extending northward several hundred of km [*Muñoz and Garreaud*, 2005].

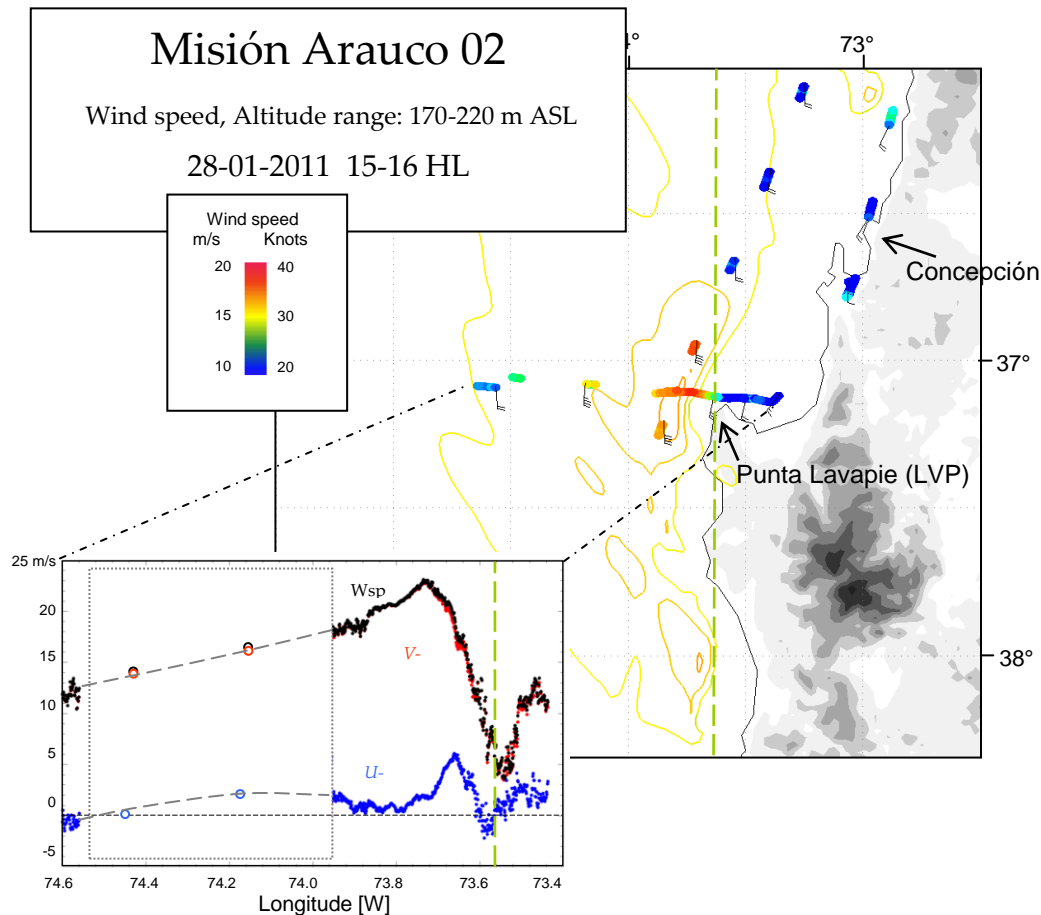


**Figure 1.2.** Wind speed measured by an instrumented aircraft during a wind jet event off Punta Lavapie. The lower inset shows the wind speed (Wsp), zonal ( $u$ ) and meridional ( $v$ ) components illustrating the general southerly flow at the jet core.

In this thesis we focus on the seasonal and synoptic variability of the atmospheric forcing on the surface ocean circulation. Intraseasonal fluctuations and interannual variability are studied elsewhere [e.g. *Hormazabal et al.*, 2002; *Pizarro et al.*, 2002; *Vega et al.*, 2003]. The main objectives of this thesis are to describe the surface ocean response at seasonal and synoptic scales, and to identify the atmosphere-ocean interactions involved. This was motivated by the existence of a southerly coastal wind jet off central Chile, which is more frequent during austral spring and summer, introducing seasonal variability in the wind stress. The lack of information on the surface ocean response to atmospheric jet events, partly because of the scarcity of *in situ* data, encouraged us to use numerical modeling with enhanced time resolution of the atmospheric forcing, comparing with previous simulations, and using more efficient regional ocean models.

## 1.2. Eastern Boundary Current System Dynamics

In this section a basic overview of the eastern boundary current system dynamics is provided, in order to make easier to the reader understand the ocean processes involved in this research.

The coastal ocean response to upwelling wind forcing in a region of uniform topography and straight coast line have been widely study and it is relatively well understood [e.g. *Charney, 1955; Anderson and Gill, 1975; Philander and Yoon, 1982*]. Assuming that the wind starts blowing alongshore, independent of the cross shore direction, above an ocean at rest, the wind stress produces offshore currents associated to the Ekman transport [*Ekman, 1905*],

$$u_{Ek} = \frac{M_x}{D},$$

where  $M_x$  is the offshore transport and  $D$  is the Ekman layer depth, which are given by [e.g. *Cushman-Roisin, 1994*]:

$$M_x = \frac{\tau^y}{\rho_0 f} \quad D = \frac{0.4}{f} \sqrt{\frac{\tau}{\rho_0}}$$

where  $\tau$  is the wind stress magnitude,  $\tau^y$  is its meridional (alongshore) component,  $\rho_0$  is a characteristic density of the sea water ( $\sim 1025 \text{ kg m}^{-3}$ ) and  $f$  is the Coriolis parameter related to the rotating Earth. Typical values of  $D$  off central Chile are  $\sim 40 \text{ m}$ .

Close to the coast exists a thin strip, with a thickness equal to the baroclinic radius of deformation, which is typically 30 km at mid-latitudes [*Chelton et al., 1998*], where the cross-shore Ekman transport changes from its typical offshore value ( $M_x$ ) to zero at the coast. This produces divergence, which generates vertical velocities promoting coastal upwelling of cold subsurface waters (Figure 1.3). This process moves the isopycnals upward near the coast, producing a zonal gradient of the dynamic height, which is geostrophically balanced:

$$v_g = \frac{1}{f} \frac{\partial \phi'}{\partial x}$$

where  $\phi'$  is the dynamic height (geopotential anomaly) respect to a reference level, for example 1000 db (1000 m). Considering that the mean sea level is a surface of equal gravitational potential, the sea level anomalies ( $\eta$ ) are geopotential anomalies. Thus, the surface geostrophic (*sfg*) flow is given by:

$$v_{sfg} = \frac{g}{f} \frac{\partial \eta}{\partial x}$$

and it is related to the meridional wind stress by [*Csanady, 1977*]:

$$\eta = -\frac{\tau^y t}{\rho f R_0} \left[ e^{-y/R_{01}} + \frac{h'}{h} \frac{R_1}{R_0} e^{-y/R_1} \right], \quad (\text{non-oscillatory solution})$$

assuming that the water depth is constant  $H = h + h'$ , a slightly lighter top layer of equilibrium depth  $h$  lying over dense water of depth  $h'$ .  $R_0$  is the barotropic Rossby radius of deformation ( $R_0 = c_0/f$ ),  $c_0$  is the phase speed of a barotropic wave ( $c_0 = \sqrt{gH}$ ),  $R_1$  is the internal deformation radius ( $R_1 = c_1/f$ ),  $c_1$  is the phase speed of a baroclinic wave ( $c_1 = \sqrt{g\Delta\rho h h' / \rho H}$ ) and  $t$  is time. It is important to note that this solution is valid for a sufficiently short period (days) and permit us elucidate important properties of the initial motion. These results show that a southerly wind stress produces a fall down of the sea level anomaly toward the coast (in the southern hemisphere), resulting in a surface geostrophic equatorward flow.

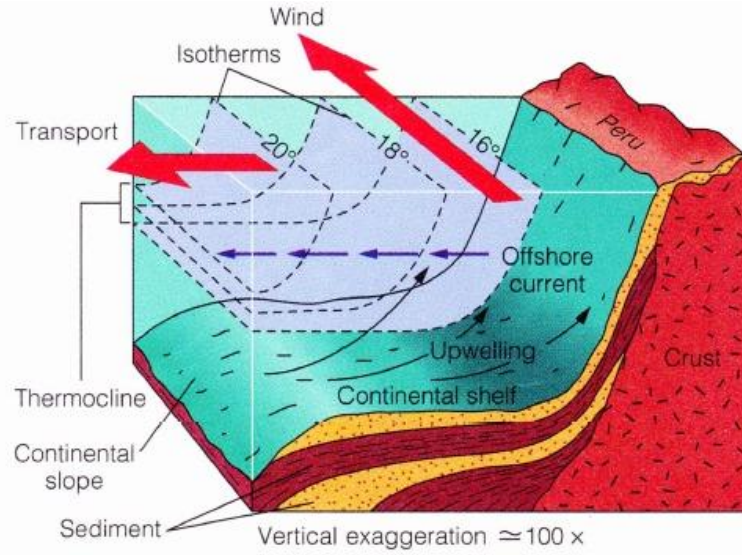


**Figure 1.3.** Simplified scheme of the upwelling process off the South East Pacific (source: www.worldgeographic.org).

To this point it has been considered an  $f$ -plane dynamics, that is, one in which there is not latitudinal variation of the Coriolis parameter  $f$ . In this case the energy remains trapped inside the baroclinic deformation radius. When including the latitudinal variation of  $f$ , that is the  $\beta$ -effect, the energy may propagate offshore. This occurs because the fluid experiments a large advection from high latitudes to lower latitudes changing its planetary vorticity ( $f$ ). Thus, long waves (Rossby waves) are induced, which propagates to the west extending the horizontal scale of the meridional surface current [e.g. *Anderson and Gill, 1975, Philander and Yoon 1982*], in order to preserve the potential vorticity:

$$\frac{D}{Dt} \left( \frac{\zeta + f}{H} \right) = 0$$

where  $\zeta$  is the vertical component of the vorticity and  $H$  is the water column depth.

Another related mechanism with the wind forcing which generates surface currents is related to the wind stress curl. If the wind stress curl is null the equilibrium state in an infinite

wide and deep ocean corresponds to an ocean at rest below the Ekman layer depth ( $D$ ), since wind field may generate surface Ekman transport. In contrast, if the wind stress field varies spatially (i.e. the curl is different from zero), then the equilibrium state correspond to a Sverdrup balance, which is a simple solution obtained from the depth integrated potential vorticity equation in its stationary and linear form. Thus, the Sverdrup balance (Figure 1.4) is a direct relationship between the latitudinal transport ( $V$ ) and the wind stress curl,

$$\beta V = \nabla \times \tau$$

where  $\beta$  is the latitudinal variation of  $f$  ( $\beta = df/dy$ ).

The Sverdrup circulation explains well many of the general characteristics of the large scale circulation and the distribution of sea water properties. Nevertheless, the low frequency variability associated to the regional wind stress may introduce important deviations from this stationary state scheme. In fact, the propagation of coastal trapped waves (Kelvin waves) and planetary waves (Rossby waves) are essential processes in the ocean adjustment to the Sverdrup balance [Anderson and Gill, 1975]. The effects of those waves are particularly relevant to understand the low frequency (periods from weeks to years) dynamics off Perú and Chile [e.g Pizarro, 1999].

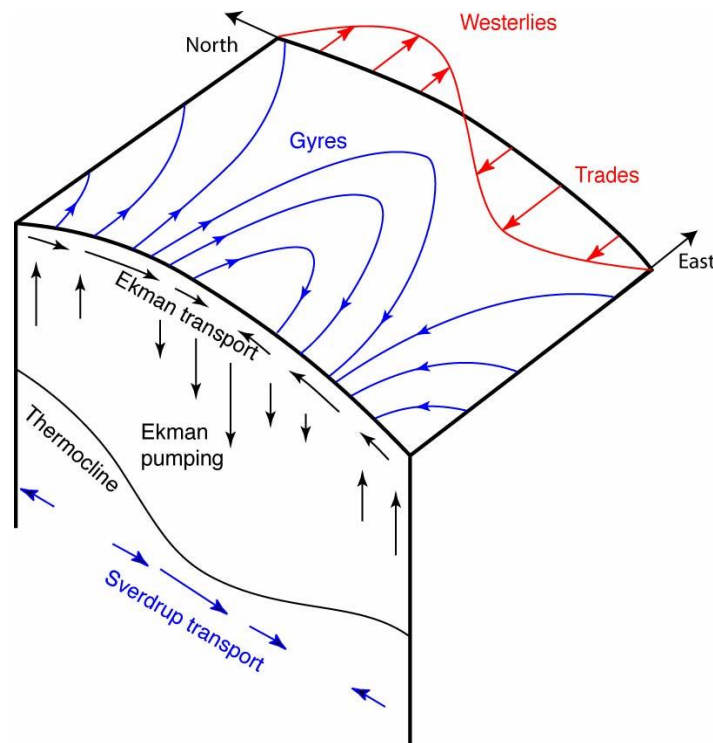


**Figure 1.4.** Schematic plot of the processes involved in the equilibrium state (Sverdrup balance) producing a Sverdrup transport in the northern hemisphere (source: www-pord.ucsd.edu).

### 1.3. Upper-ocean regional circulation in the Eastern South Pacific

The main features of the upper-ocean regional circulation in the eastern South Pacific have been extensively reviewed by *Strub et al.* [1998]. They identified four major currents off central Chile (Figure 1.5): 1) the Chile-Peru Current (also known as the Humboldt Current), which is the surface equatorward flow traditionally identified as the eastern branch of the subtropical South Pacific gyre; 2) a coastal jet called the Chile Coastal Current that flows equatorward and is directly related to the upwelling dynamics; 3) the Peru-Chile Countercurrent, which is a surface poleward flow located about 100-300 km offshore of the Chile Coastal Current [Strub et al., 1995] and 4) the Peru-Chile Undercurrent, which is a coherent subsurface current that flows poleward over the slope along the Peruvian and Chilean coasts [e.g., *Silva and Neshyba*, 1979; *Huyer et al.*, 1991a; *Shaffer et al.*, 1997]. Based on satellite-tracked, near-surface (15-m depth) drifters, *Chaigneau and Pizarro* [2005] observed a mean surface equatorward flow extending to about 82°W off central Chile, with a mean speed of about  $6 \text{ cm s}^{-1}$ . This flow is consistent with the large-scale South Pacific gyre circulation, traditionally recognized by classical geostrophic calculations based on hydrographic data. However, using satellite-derived surface geostrophic currents *Fuenzalida et al.*, [2008] described a jet-like stream as a central component of the Chile-Peru current, with a summer intensification.

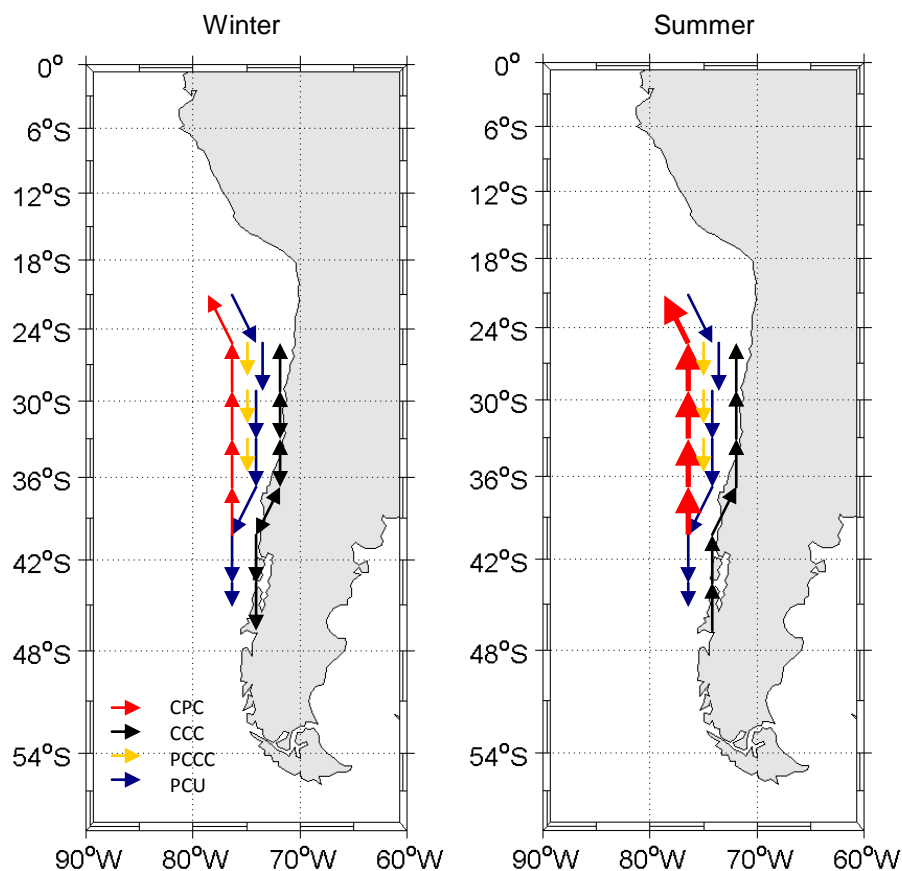


**Figure 1.5.** Simplified scheme of the regional near-surface circulation off central Chile. Adapted from Strub et al., 1998.

## 1.4. Outline

This thesis is organized as follows: the methods used in this research are detailed in Chapter 2, which include data sets and data processing, the ocean model applied and a general validation of a climatological simulation. In Chapter 3, the seasonal dynamics of the near-surface alongshore currents is described, and the role of the seasonal cycle of the wind field is discussed through different experiments using the numerical ocean model. Finally, in Chapter 4, the surface ocean response to synoptic-scale variability in wind stress is described using different surface forcing in the numerical model experiments to account for the role of wind stress and heat fluxes in mean surface currents, sea surface temperature and eddy kinetic energy.

The main results of this thesis were already reported in two scientific articles. The first one (Chapter 3) was published in the *Journal of Geophysical Research – Oceans* (2012), and the second one (Chapter 4) to be submitted to *Dynamics of Atmospheres and Oceans*.

# Chapter 2

## Methods

### 2.1 Datasets and data processing

We focused on a large region covering central Chile between 25° – 45°S and extending from the coast to 90°W (Figure 2.1a). Sea level anomalies (SLA) and geostrophic surface current anomalies derived from altimetry from 1993 to 2007 were used in this study. They are gridded in a Mercator mesh of 1/3° spatial resolution by SSALTO/DUACS and distributed by AVISO (Archivage, Validation, Interprétation des données des Satellites Océanographiques). Time series of SLA and geostrophic currents with weekly temporal resolution were monthly averaged. The absolute surface velocity was obtained by adding a mean geostrophic current based on the dynamic height estimated using temperature and salinity climatologies from CARS (CSIRO Atlas of Regional Seas) 2006 [Ridgway *et al.*, 2002] with 1000 db as the reference level. We use wind stress from QuikScat data from 2000 to 2007. Monthly mean wind stress data with a spatial resolution of 0.5° were obtained from Centre d'Exploitation et de Recherche Satellitaire (CERSAT), at Institut Francais de Recherche pour l'Exploitation de la Mer (IFREMER).

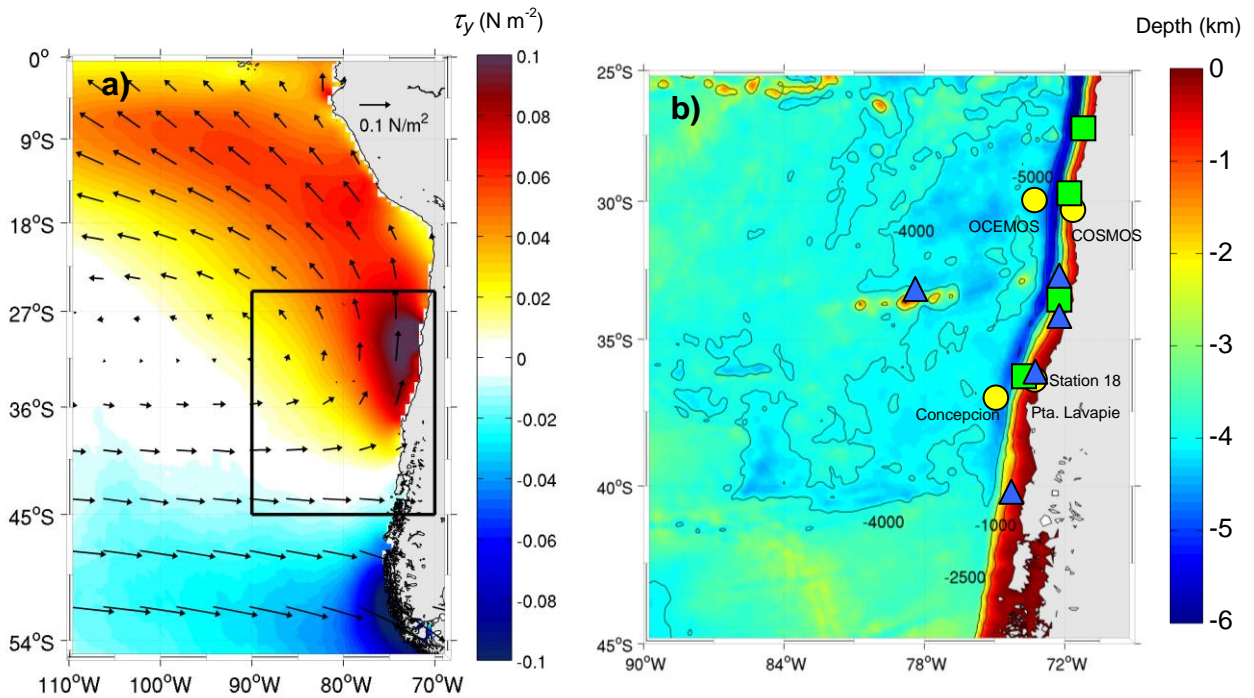


**Figure 2.1.** a) Mean of the meridional wind stress magnitudes (colors, in  $\text{N m}^{-2}$ ) and wind stress vectors (arrows) derived from QuikSCAT satellite data for the period 2000-2007. The black square indicates the model domain used in this study. b) Bottom topography of the study area. Depth contours are shown for 1000 m, 2500 m, 4000 m and 5000 m. In addition, yellow dots indicate the mooring locations, green squares indicate tide gauge locations and blue triangles indicate thermistor locations.

The wind data allowed us to compare the relative contributions of the Ekman transport and Ekman pumping to the vertical velocities and transports near the coast. The Ekman pumping vertical velocities ( $w$ ) were estimated directly from the curl of the wind stress ( $\vec{\tau}$ ) fields [e.g., Stewart, 2008]

$$w = \nabla \times \frac{\vec{\tau}}{\rho f},$$

where  $\rho$  is a representative density for seawater ( $1025 \text{ kg m}^{-3}$ ). These vertical velocities are then integrated from the coast to  $\sim 150 \text{ km}$  and in each  $0.5^\circ$  of latitude to obtain the vertical transports. The cross-shore Ekman transport near the coast is estimated by

$$M_x = \frac{\tau_y}{\rho f},$$

where  $\tau_y$  is the alongshore (assumed meridional in the study region, positive to the north) component of the wind stress. These values are also integrated every  $0.5^\circ$  of latitude. In this case we only integrated meridionally, considering that the offshore Ekman transport  $M$  ( $\text{m}^2 \text{ s}^{-1}$ ) is completely compensated by a vertical transport near the coast.

To evaluate the quality of the variability of the velocities estimated from the gridded altimetry and the model, *in-situ* currents measurements are used (Table 1). Hourly data were obtained from four moorings located off  $\sim 30^\circ\text{S}$  and  $\sim 37^\circ\text{S}$  (Figure 2.1b). Two of them were located close to the coast, about  $13 \text{ km}$  offshore at  $30^\circ\text{S}$  (COSMOS) and about  $20 \text{ km}$  offshore at  $37^\circ\text{S}$  (Station 18). Both moorings were instrumented with a 300-kHz acoustic Doppler current profiler (ADCP) pointing upward. In addition, four recording current meters (RCM 7) are available at  $30^\circ\text{S}$  (Figure 2.2). Because the observed vertical structure of currents is more clearly defined in coastal regions than in offshore areas, these coastal data are used to validate the model velocities profiles. The other two moorings are located farther offshore ( $>100 \text{ km}$ ) and are used to compare upper-ocean current variability with satellite data. At  $37^\circ\text{S}$  the Concepción mooring was instrumented with an ADCP, but we only use the measurements at  $50 \text{ m}$  depth. At  $30^\circ\text{S}$  (OCAMOS mooring) the shallowest measurement is from a RCM 7 located at  $340 \text{ m}$  depth. Table 1 lists the positions, start and end times of the current meter records, and the depth of the water column.

The squared coherence values between the satellite-derived geostrophic velocities and the *in-situ* offshore currents are plotted in Figure 2.3. Despite the fact that the satellite-derived geostrophic currents represent surface velocities and the *in-situ* data are from  $50$  and  $340 \text{ m}$  depth, they show significant coherence at periods longer than  $100$  days. The phase is close to zero at these periods. The use of rotary spectra is preferred because oceanic velocity vectors do not present a dominant direction.

To validate the seasonal cycle of modeled sea level, *in-situ* data near the coast recorded by tide-gauges at four different locations are analyzed (Figure 2.1a). These data were provided by the Servicio Hidrográfico y Oceanográfico de la Armada (SHOA), and they are from Caldera ( $27.1^\circ\text{S} - 70.8^\circ\text{W}$ ), Coquimbo ( $30^\circ\text{S} - 71.4^\circ\text{W}$ ), Valparaíso ( $33^\circ\text{S} - 71.6^\circ\text{W}$ ) and Talcahuano ( $36.7^\circ\text{S} - 73.1^\circ\text{W}$ ).



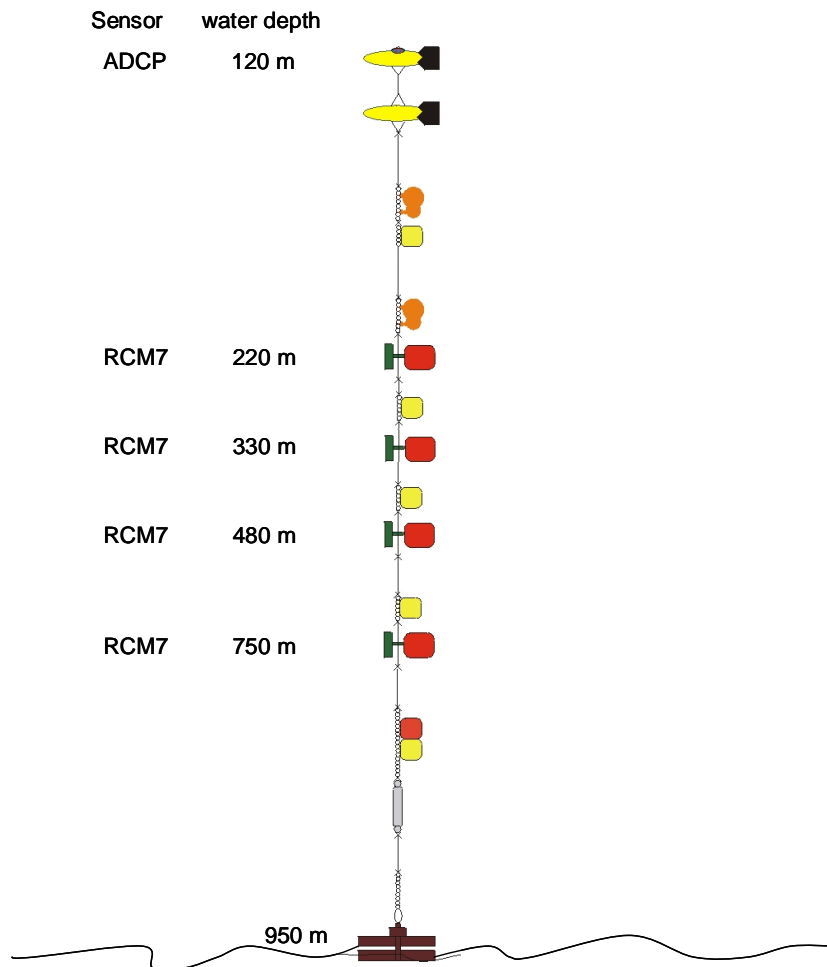
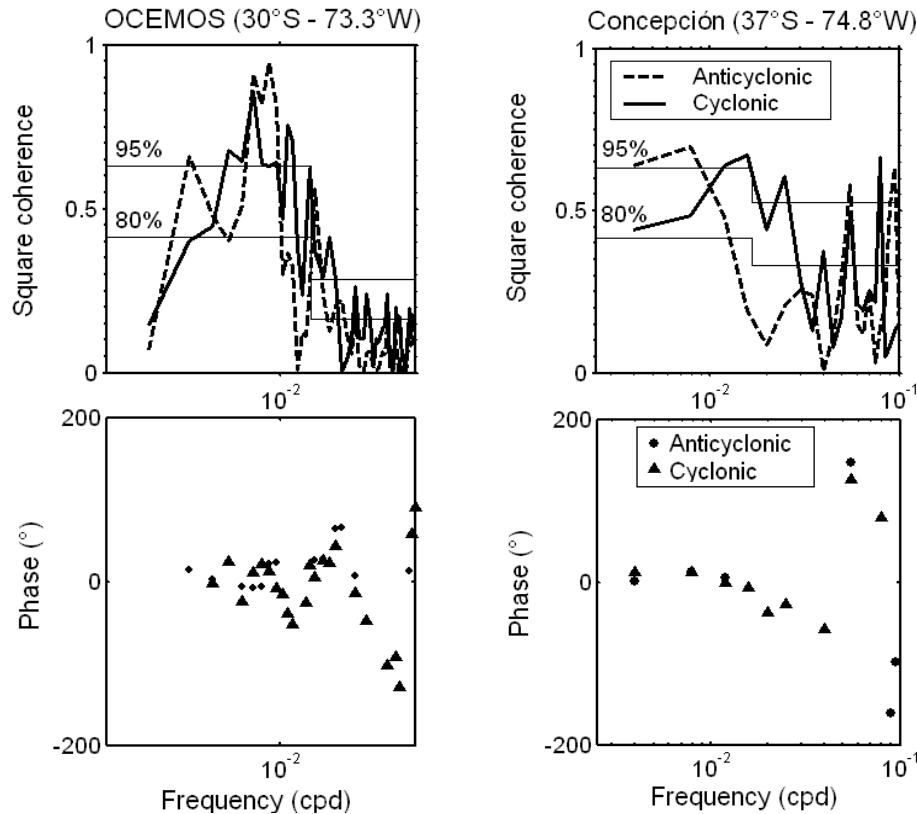


Figure 2.2. Scheme of the COSMOS mooring (source from Oscar Pizarro).

Table 1. Information about the moorings and measurements.

Site	Instrument	Latitude	Longitude	Start time	End time	Instrument depth measurement	Water depth
OCEMOS	RCM7	30° 00' S	73° 15' W	Jan 1996	Sep 2006	340 m	4400 m
COSMOS	ADCP			Apr 2003	Sep 2006	10-110 m (bin 5m)	
	RCM7			Nov 1991	Sep 2008	220 m	
	RCM7	30° 21' S	71° 47' W	Sep 2000	Oct 2003	330 m	950 m
	RCM7			Nov 1991	Apr 2009	480 m	
	RCM7			Nov 1991	Jun 2008	750 m	
Concepción	ADCP	37° 03' S	74° 50' W	Nov 2003	Oct 2006	50 m	4600 m
Station 18	ADCP	36° 28' S	73° 10' W	Jan 2009	Jan 2011	6-86 m (bin 4 m)	100 m



**Figure 2.3.** Rotary coherence (upper panels) and phase (lower panels) between the cyclonic and anticyclonic components of the satellite-derived surface current anomalies (AVISO) and *in-situ* observations at OCEMOS ( $\sim 30^{\circ}\text{S}$ - $73.3^{\circ}\text{W}$ ) and Concepción ( $\sim 37^{\circ}\text{S}$ - $78.4^{\circ}\text{W}$ ). Horizontal lines indicate 80% and 95% coherence significance levels. Phase results for values higher than 80% are plotted for the cyclonic (triangles) and anticyclonic (dots) components. The depths of the *in-situ* currents are 340 m at  $30^{\circ}\text{S}$  and 50 m at  $37^{\circ}\text{S}$ .

We used both satellite and *in-situ* data to validate the simulated SST. To compare the simulated mean SST field to observations we used the long-term mean (years 1985-2001) SST obtained from the Advanced Very High Resolution Radiometer (AVHRR). The data set has a spatial resolution of  $\sim 4 \times 4$  km and corresponds specifically to the product named Pathfinder Version 5.0 SST Project (Pathfinder V5) and is distributed by the Physical Oceanography Distributed Active Archive Center (PO.DAAC).

The offshore SST synoptic variability field was obtained from the TRMM Microwave Imager (TMI) data set produced by Remote Sensing Systems (RSS). These data were used to compare with the simulated synoptic SST variability, since it is largely uninfluenced by cloud cover, aerosols and atmospheric water vapor [Wentz *et al.*, 2000]. Daily satellite SST data between 2000 and 2007 on a regular grid of  $0.25^{\circ}$  for latitudes lower than  $\sim 38^{\circ}\text{S}$  were used. Since the TMI blind zone correspond to the first 50 km from the coast, modeled coastal SST had to be validated against *in-situ* data recorded by near surface thermistors at five different locations (Figure 2.1b). These daily SST data were provided by the Servicio Hidrográfico y Oceanográfico de la Armada (SHOA), at Valparaíso ( $33^{\circ}\text{S}$  –  $71.6^{\circ}\text{W}$ ), San Antonio ( $33.6^{\circ}\text{S}$  –  $71.5^{\circ}\text{W}$ ), Talcahuano ( $36.7^{\circ}\text{S}$  –  $73.1^{\circ}\text{W}$ ), Corral ( $39.9^{\circ}\text{S}$  –  $73.4^{\circ}\text{W}$ ) and Robinson Crusoe Island ( $33.6^{\circ}\text{S}$  –  $78.8^{\circ}\text{W}$ ).

## 2.2 The Regional Ocean Model

The model used in this research is the Regional Oceanic Modeling System (ROMS), which is a split-explicit, free surface, topographically-following-coordinates (Figure 2.4a) oceanic model [Shchepetkin and McWilliams, 2005]. ROMS is an evolutionary descendent from SCRUM (the S-Coordinate Rutgers University Model; Song and Haidvogel, 1994). ROMS solves the primitive-equations in hydrostatic and incompressible conditions. The prognostic variables are surface elevation, barotropic and baroclinic horizontal velocity components, and material properties such as temperature and salinity. Where boundaries are open (Figure 2.4b), oblique radiation conditions are used to estimate the direction of information flux in order to treat the inward and outward fluxes of information separately. When information fluxes are outward the boundary is passive and when they are inward the boundary is active [Marchesiello *et al.*, 2001]. In order to absorb disturbances and reduce noise associated with the radiation condition, the model uses a sponge layer, which is a region of increased horizontal viscosity close to the open boundaries. In our simulations we use a 50-km-wide sponge layer. The vertical mixing is parameterized using the K-Profile Parameterization (KPP), which is a non-local closure scheme based on the boundary layer formulation by Large *et al.*, [1994].

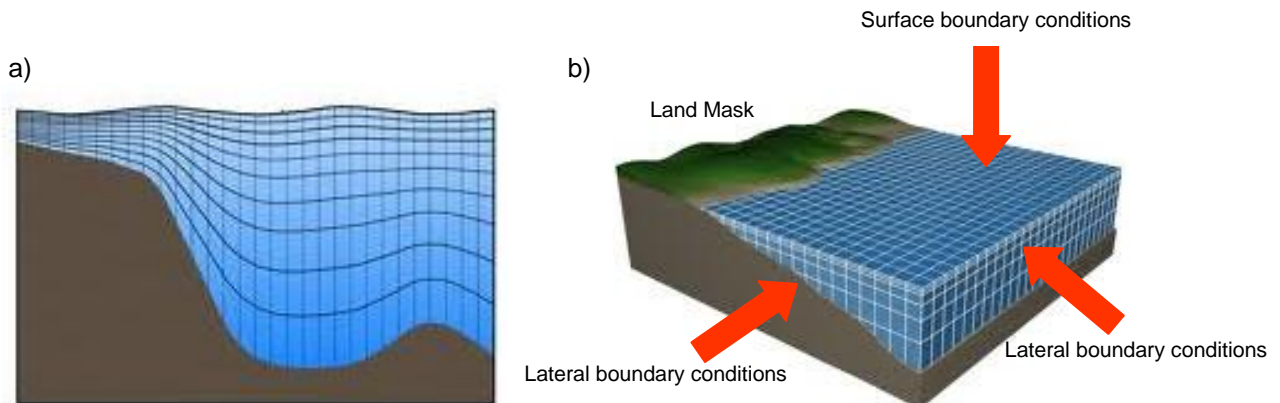


**Figure 2.4.** a) Vertical discretization in topographically-following-coordinates (sigma-coordinates). b) Open boundaries and land mask in a regional ocean model (source: [www.meted.ucar.edu](http://www.meted.ucar.edu)).

A mode-splitting technique allows the separation of the barotropic and baroclinic components with different time steps. The mode splitting is done using a time filter, which ensures that the continuity equation is satisfied on the discrete level, thus removing previous restrictions of small free-surface changes [Marchesiello *et al.*, 2003]. The time stepping is a leap frog/Adams–Moulton, predictor–corrector scheme, which is third-order accurate in time and has good dispersive properties for the advection equation. An expanded regime of stability allows larger time steps.

The model has been designed to use parallel computer architectures, allowing us to solve much larger problems than with a serial code. Parallelization and optimal use of processors are done simultaneously by an explicit two-dimensional partitioning into sub domains. Eight processors were used to perform our runs at 10-km resolution requiring about 36 hours to complete one year simulation.

## 2.3 Equations resolved by the regional ocean model

ROMS is a three-dimensional, free-surface, terrain-following numerical model that solves the Navier-Stokes equations using the hydrostatic and Boussinesq assumptions. The equations in Cartesian coordinates can be written as:

<b>Momentum conservation</b>	$\frac{\partial u}{\partial t} = \vec{u} \cdot \nabla u - fv = -\frac{1}{\rho_o} \frac{\partial p}{\partial x} + \nabla_h (K_{Mh} \cdot \nabla_h u) + \frac{\partial}{\partial z} (K_{Mv} \frac{\partial u}{\partial z})$ $\frac{\partial v}{\partial t} = \vec{u} \cdot \nabla v + fu = -\frac{1}{\rho_o} \frac{\partial p}{\partial y} + \nabla_h (K_{Mh} \cdot \nabla_h v) + \frac{\partial}{\partial z} (K_{Mv} \frac{\partial v}{\partial z})$
<b>Hydrostatic</b>	$0 = -\frac{1}{\rho_o} \frac{\partial p}{\partial x} - \rho g$
<b>Continuity</b>	$0 = \frac{\partial u}{\partial x} + \frac{\partial v}{\partial y} + \frac{\partial w}{\partial z}$
<b>Tracer conservation</b>	$\frac{\partial T}{\partial t} = \vec{u} \cdot \nabla T = \nabla_h (K_{Th} \cdot \nabla_h T) + \frac{\partial}{\partial z} (K_{Tv} \frac{\partial T}{\partial z})$ $\frac{\partial S}{\partial t} = \vec{u} \cdot \nabla S = \nabla_h (K_{Sh} \cdot \nabla_h S) + \frac{\partial}{\partial z} (K_{Sv} \frac{\partial S}{\partial z})$
<b>Equation of state</b>	$\rho = \rho(S, T, p)$

The surface and bottom boundary conditions are prescribed as:

	<b>Surface (z = <math>\eta</math>)</b>	<b>Bottom (z = -H)</b>
<b>Kinematic</b>	$\frac{\partial \eta}{\partial t} = w$	$\vec{u} \cdot \nabla(-H) = w$
<b>Wind stress/ Bottom friction</b>	$K_{Mv} \frac{\partial u}{\partial z} = \frac{\tau_x}{\rho_0}$	$K_{Mv} \frac{\partial u}{\partial z} = \frac{-C_D  \vec{u}  u}{\rho_0}$
	$K_{Mv} \frac{\partial v}{\partial z} = \frac{\tau_y}{\rho_0}$	$K_{Mv} \frac{\partial v}{\partial z} = \frac{-C_D  \vec{u}  v}{\rho_0}$
<b>Heat flux</b>	$K_{Tv} \frac{\partial T}{\partial z} = \frac{Q}{\rho_0 C_p}$	$K_{Tv} \frac{\partial T}{\partial z} = 0$
<b>Salt flux</b>	$K_{Sv} \frac{\partial S}{\partial z} = \frac{S(E - P)}{\rho_0}$	$K_{Sv} \frac{\partial S}{\partial z} = 0$

Where  $K_{Mh}$ ,  $K_{Th}$ ,  $K_{Sh}$  and  $K_{Mv}$ ,  $K_{Tv}$ ,  $K_{Sv}$  are the horizontal and vertical diffusivities of momentum, temperature and salinity respectively.  $T$  is temperature and  $S$  salinity.  $E$  is evaporation and  $P$  precipitation.  $Q$  is the heat flux at surface and  $C_D$  is the bottom drag coefficient.

## 2.4 Model Validation

Satellite and *in-situ* data were used to validate the model performance and we contrasted the simulated climatological near-surface circulation with known features of the Chile-Perú Current System. The seasonal mean of the simulated and satellite SLA are compared, but it is important to note that a climatological simulation lacks the energetics of intraseasonal and interannual forcing. This last may modulate the amplitude of the seasonal scale variability. Although the altimeter data exhibits larger seasonal amplitude, the modeled and observed SLA are similar in their patterns (Figure 2.5). Low (high) anomalies are generated in a narrow strip close to the coast during summer (winter), consistent with the seasonal variability of the wind stress. Offshore, the simulated SLAs show more structure with relatively smaller scales than those observed in the altimetry data, which is smoothed in the process of creating gridded fields from multiple altimeters. To validate the model seasonal variability near the coast, we compared the model coastal sea level with tide-gauge data at four different locations (Figure 2.6). Model sea level agrees well with the *in-situ* observations, including the fact that the annual cycle is larger at Talcahuano ( $\sim 36.6^\circ\text{S}$ ).

The vertical sections of the alongshore (meridional) currents at latitudes of  $30^\circ\text{S}$  and  $36^\circ\text{S}$  (Figure 2.7a,c) are consistent with the major currents of the Southeast Pacific as identified by *Strub et al.*, [1998]. Near the coast, within the first  $\sim 50$  km, the model reproduces an equatorward jet that represents the Chile Coastal Current (CCC). At  $30^\circ\text{S}$  the CCC is stable and is present year-round; it only slightly weakens during fall (not shown). Over the continental slope, below the CCC, the model exhibits a poleward flow that is consistent with the Peru-Chile Undercurrent (PCU). At  $30^\circ\text{S}$ , this current is observed during the whole year, with maximum values of  $\sim 15$   $\text{cm s}^{-1}$  near its core, which is located between 150 and 300 m depth. This mean value agrees well with the annual mean value of  $13$   $\text{cm s}^{-1}$  obtained for a six year period of current measurements near the PCU core over the slope at  $30^\circ\text{S}$  [*Shaffer et al.*, 1999].

Another poleward flow is observed farther offshore, between 150 and 200 km from the coast, extending from the surface to more than 500 m depth north of  $\sim 33^\circ\text{S}$ . This flow can be associated with the Peru-Chile Countercurrent (PCCC). The PCCC may be clearly differentiated from the PCU north of  $\sim 33^\circ\text{S}$ . In contrast, at  $36^\circ\text{S}$  the poleward flow that reaches the surface west of the CCC, may be associated with an outcrop of the PCU more than the PCCC. *Penven et al.*, [2005] found that the PCCC appears indiscernible from the PCU at lower latitudes ( $6^\circ - 10^\circ\text{S}$ ) and that the PCU outcrops at about 100 km from the shore at southern latitudes ( $10^\circ - 20^\circ\text{S}$ ). These results seem to be consistent with those obtained by *McCreary and Chao* [1985] using a linear model, who argued that the undercurrent may reach the surface in the case of cyclonic stress curl. Therefore, *Penven et al.* speculated that the currents observed by *Strub et al.* [1995] in three years of altimeter data and identified as the PCCC might correspond to the outcropping of the PCU. Nevertheless, in our model fields north of  $\sim 33^\circ\text{S}$ , the PCCC is clearly different than the PCU and flows poleward offshore of the CCC and onshore of the Chile-Perú Current (CPC), in agreement with the location described by *Strub et al.*, [1995].

Further verification of the model performance in simulating the mean currents is provided in Figure 2.7b,d by the mean vertical profiles of zonal ( $u$ ) and meridional ( $v$ ) velocity components, along with their observational counterparts from two moorings at COSMOS and Station 18 (Table 1). Mean profiles from model and observations are very similar – their shapes agree well and the model captures the reversal of the currents at different depths. At COSMOS,

the model profiles show an overestimation of the northward surface current, but the intensity of the PCU at 220 m depth is well represented by the model with values around  $15 \text{ cm s}^{-1}$ .

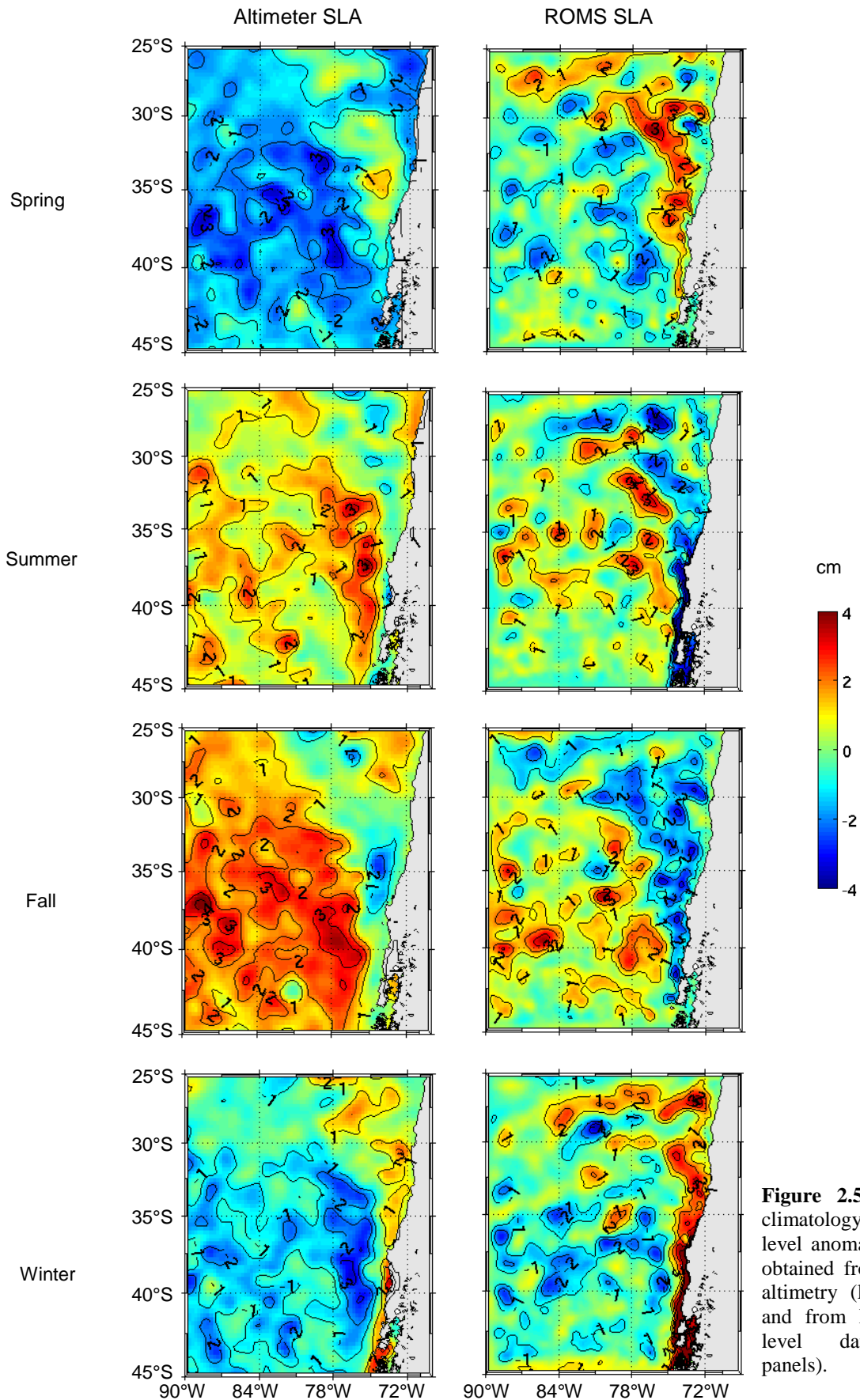


**Figure 2.5.** Seasonal climatology of the sea level anomalies (SLA) obtained from AVISO altimetry (left panels) and from ROMS sea level data (right panels).

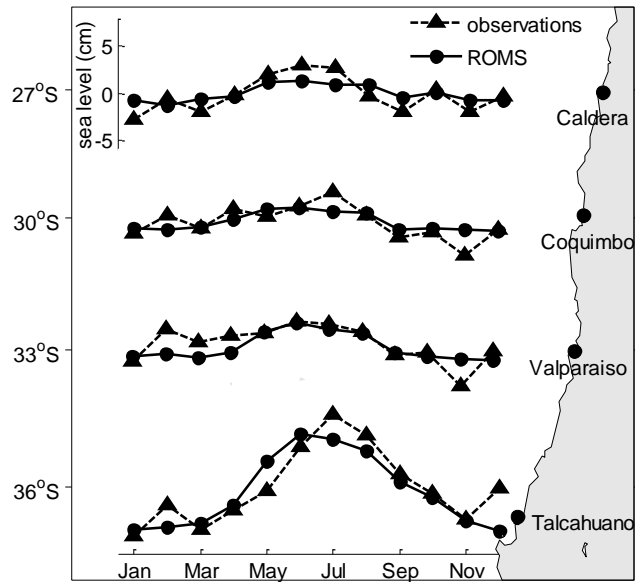


**Figure 2.6.** Seasonal sea level at Caldera (27.1°S - 70.8°W), Coquimbo (30°S - 71.4°W), Valparaíso (33°S - 71.6°W) and Talcahuano (36.7°S - 73.1°W) obtained from tide gauges and the simulated sea level approximately 4 km offshore.

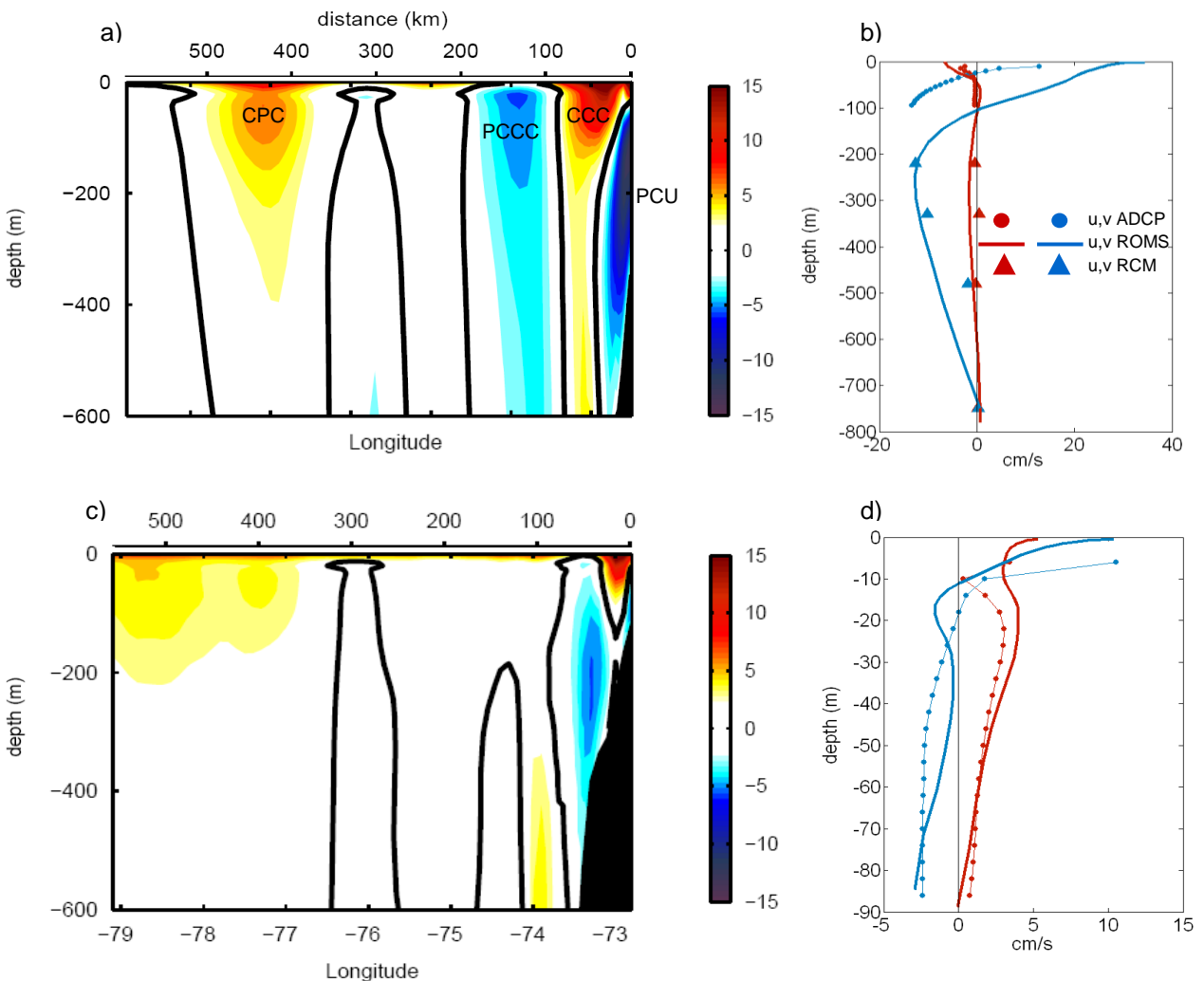


**Figure 2.7.** Mean vertical section of the simulated meridional currents at a) 30°S and c) 36°S. Mean profiles of the meridional (black) and zonal (gray) currents at the moorings b) COSMOS and d) Station 18.

The offshore propagation of the surface alongshore geostrophic current is a feature that has been observed widely in altimeter data [e.g., *Chelton and Schlax, 1996; Ramos et al., 2006*]. In this work both, model and satellite meridional geostrophic currents, showed offshore propagation at different latitudes. To better illustrate this propagation we show a Hovmoller diagram at 37°S (Figure 2.8). The thick black line represents the theoretical phase speed of the first long Rossby wave mode [e.g., *Gill, 1982*].

$$C = -\frac{\beta c_1^2}{f^2}$$

where  $c_1$  is the phase speed of the first baroclinic mode of a long gravity wave. It is important to note that eddies in the ocean propagate nearly due west at approximately the phase speed of nondispersive baroclinic Rossby wave [*Chelton et al., 2007*]. Thus, new observations from higher resolution SLA fields constructed from multiple satellite altimeters have cast doubt on the original interpretation of the observations as linear waves [*Chelton et al., 2011*].

To compare with altimetry data we use  $c_1$  from *Chelton et al., [1998]* in figure 2.8b, while for figure 2.8a  $c_1$  was computed using the annual mean stratification from the model temperature and salinity. The phase speed of the first baroclinic mode for a Rossby wave ( $C$ ) obtained from the model stratification is slightly slower than that obtained from the observed stratification with maximum differences of about  $0.5 \text{ cm s}^{-1}$  in the northern part of our domain (not shown). This slight difference can be also observed in the slopes of the theoretical  $C$  plotted in figures 2.8a and 2.8b. This is attributed to slight differences in model and observed stratification, because  $c_1^2$  is computed from normal modes decomposition, where changes in the  $N^2$  values are absorbed by the  $c_1^2$  [e.g *Pringle and Brink, 1999*].

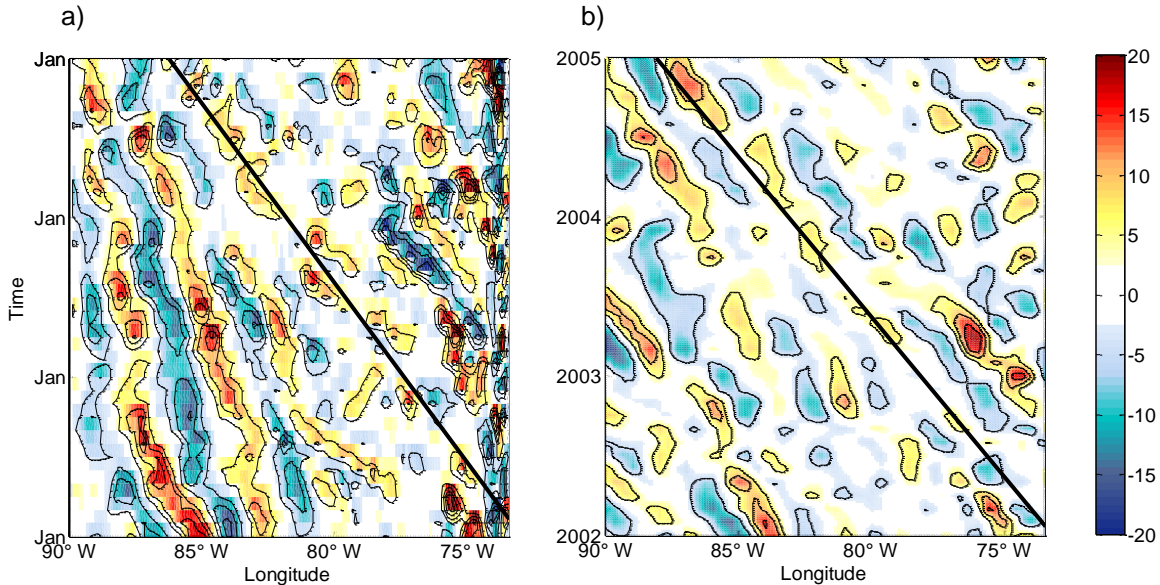


**Figure 2.8.** Hovmoller diagram of the meridional geostrophic surface currents anomalies at 37° S obtained from a) the model and b) altimetry. The thick line indicates the theoretical phase speed of a first mode Rossby wave ( $C = -\beta c_1^2 / f_0^2$ ).



In order to evaluate in detail the offshore propagation of the model currents we performed a Complex Empirical Orthogonal Function (CEOF) analysis [Horel, 1984]. This is a useful method for detecting traveling waves in space-time geophysical data. As the wave length of the propagating disturbances may depend on latitude we calculate the spatial phase of the first CEOF mode at each latitude for model and satellite surface geostrophic meridional velocities. We show the spatial phase obtained at 37° S in Figure 2.9a, corresponding to the Hovmoller diagrams showed in Figure 2.8. The spatial phase of the first CEOF mode for both, model and satellite currents, change monotonically with longitude indicating a propagation with an estimated wave length of ~250 km (i.e. ~3° of longitude) at 37°S. To estimate the wave length at each latitude we fit a straight line to the spatial phase data. Only results with a correlation coefficient  $R > 0.95$  are shown in figure 2.9b. In addition, the theoretical wave lengths of the first baroclinic Rossby wave mode with annual and semiannual periods ( $T$ ) are plotted. They were calculated from the Rossby wave dispersion relation [e.g., Gill, 1982]

$$\omega = -\frac{\beta k}{k^2 + \frac{f^2}{c^2}} \approx -\frac{\beta k c^2}{f^2},$$

where  $\omega$  is the angular frequency of the wave ( $\omega = 2\pi/T$ ),  $k$  is the wave number ( $k = 2\pi/L$ ) and  $L$  is the wave length. The model reproduces well the offshore propagation with similar wave lengths as those obtained from the satellite data. Both the model and satellite derived wave lengths tend to increase at lower latitudes and approach to the theoretical semiannual wave length.

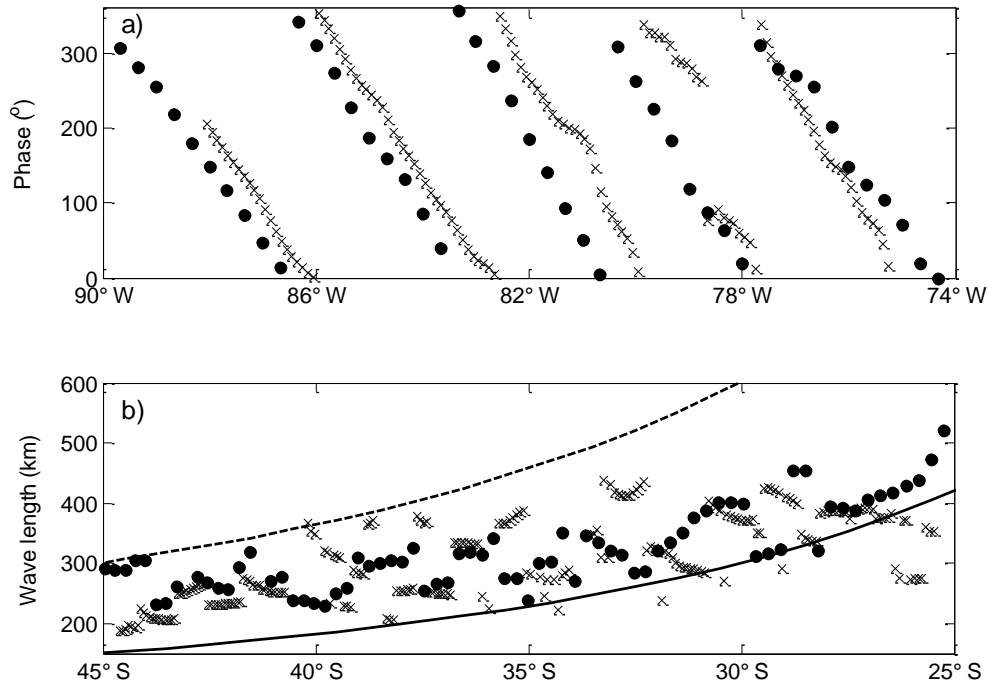


**Figure 2.9.** a) First mode of the spatial phase of the surface geostrophic meridional current using Complex Empirical Orthogonal Functions (CEOF) at 37° S. Results for the altimetry data are marked by dots and for the simulated data are marked by crosses. b) Wave length as function of latitude estimated from altimetry data (dots) and from simulated data (crosses).

The dominant semiannual wave length estimated above is probably related to the large influence of disturbances associated with waves of equatorial origin. These waves play a major role in current variability in this region at semiannual and intraseasonal time scales, i.e. periods between 30 and 90 days [e.g., *Shaffer et al.*, 1999; *Pizarro et al.*, 2002; *Ramos et al.*, 2006]. However, part of the semiannual variability in the model may result directly from the wind forcing, which also shows a significant increase of energy at this frequency. In addition, the northern boundary conditions are based on the monthly WOA temperature and salinity climatology and these data also have a semiannual signal off northern Chile [*Ramos et al.*, 2006], although weaker than that observed near the coast.

# Chapter 3

## Seasonal dynamics of the near-surface alongshore flow off central Chile

### 3.1 Introduction

The seasonal cycle of the wind field off central Chile and particularly the presence of an atmospheric low-level jet during upwelling season lead to a consideration of the role of wind stress curl in near-surface ocean circulation. In the offshore region, the wind stress curl field off central Chile is mostly anticyclonic (downwelling favorable). In contrast, the coastal band is dominated by cyclonic (upwelling favorable) curl, which exhibits a distinct annual cycle [Bakun and Nelson, 1991]. In summer, when the equatorward wind stress is more intense, stronger cyclonic (anticyclonic) wind stress curl develops east (west) of the wind jet axis, commonly located at about 150 km offshore [Garreaud & Muñoz, 2005]. This low-level wind jet and the associated wind stress curl may play a major role in coastal upwelling dynamics and surface circulation off central Chile. The seasonal cycle of the wind stress and wind stress curl based on QuikScat data are presented in Figure 3.1.

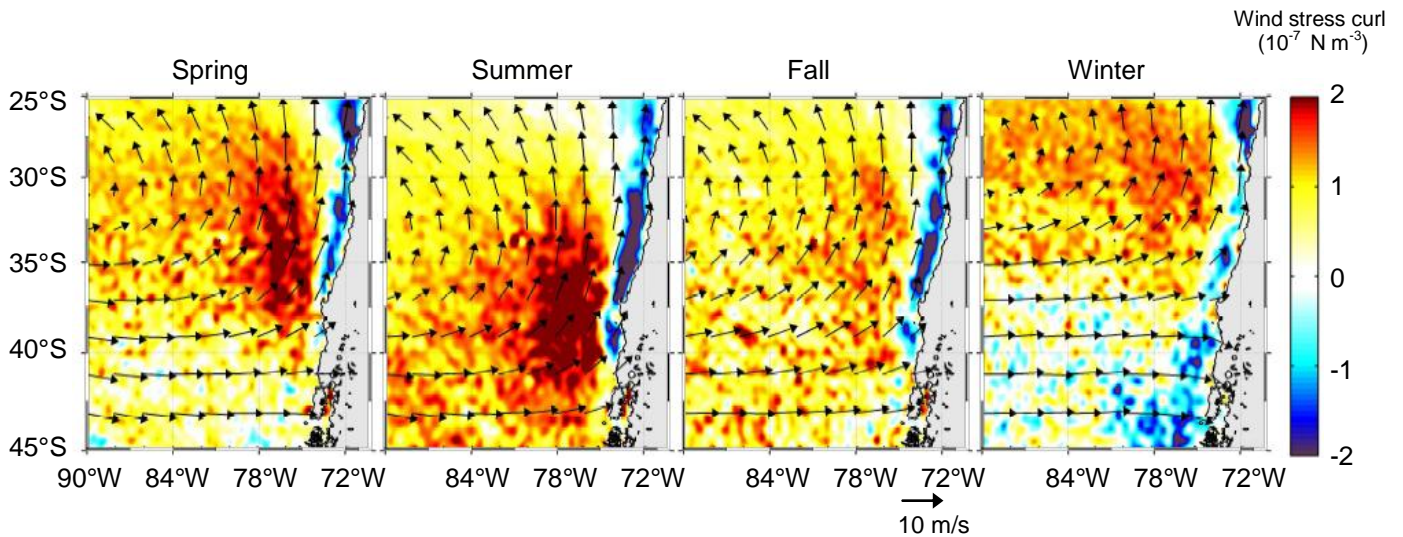


**Figure 3.1.** Mean wind velocity (vectors) and wind stress curl (colors,  $10^{-7} \text{ N m}^{-3}$ ) off central Chile derived from QuikSCAT satellite data for the period 2000-2007.

Only a few studies have addressed the dynamics of the regional ocean circulation and its seasonal variability off Chile. The few numerical modeling studies have focused on the intense upwelling region near 37°S [Batteen *et al.*, 1995; Leth and Shaffer, 2001; Leth and Middleton, 2004; Mesias *et al.*, 2001, 2003], where an oceanic jet observed farther north seems to begin. These simulations have shown a surface coastal jet, which separates from the coast around Punta Lavapie (~37°S), creating a meander that gives rise to a large upwelling plume north of 36°S. This jet and its separation have been recently confirmed by satellite and hydrographic data [Letelier *et al.*, 2009]. These results suggest that the jet observed in the coastal transition zone

(CTZ), about 100-200 km offshore off central Chile during the upwelling season (usually from November to March), is related to a current that detaches from the coast at Punta Lavapie. This jet may play a major role in the surface circulation off Central Chile, but its dynamics and seasonal variability remain almost unknown.

Here, we use the Regional Ocean Modeling System (ROMS) along with surface geostrophic currents, derived from satellite altimetry, and QuikScat winds to analyze the circulation off central Chile ( $\sim 25^{\circ}$ – $45^{\circ}$ S). The main focus of this chapter is on the jet observed in the CTZ off central Chile during spring and summer. We particularly address the effects of the seasonal variability of the wind stress and the wind stress curl on the surface alongshore currents.

### 3.2 Model setup

We carried out a climatological simulation (control run) off central Chile (between  $25^{\circ}$ – $45^{\circ}$ S, and  $70^{\circ}$ – $90^{\circ}$ W) with a horizontal resolution of  $1/10^{\circ}$  (between 7.9 and 10.1 km) and 32 sigma levels in the vertical. We used long-term monthly means from eight years of QuikScat data (2000-2007) as surface boundary conditions of wind stress and Comprehensive Ocean-Atmosphere Data Set (COADS) climatology to calculate the surface heat and freshwater fluxes [Da Silva *et al.*, 1994]. The initial and lateral boundary conditions were obtained from the World Ocean Atlas 2005 monthly climatology [Locarnini *et al.*, 2006; Antonov *et al.*, 2006]. The model topography (Figure 2.1b) is based on the global ETOPO2 at  $2'$  resolution [Smith and Sandwell, 1997]. The model runs for ten years of 360 days with a spin up period of 2 years, so model climatology was based on the last eight years. All the output variables were daily averaged. Geostrophic surface currents were calculated using the model sea level ( $\eta$ ) to better compare with satellite-derived surface currents.

To understand the role of the wind stress curl in the formation of the CTZ jet we performed a second simulation, identical to the control run except that the wind stress forcing did not have curl (no-curl simulation). The wind stress field only has the meridional component ( $\tau_x = 0$  everywhere), which retains the observed latitudinal variation but it is constant in longitude. At each latitude, the modified wind stress is estimated by averaging the meridional component of the wind stress between the coast and  $80^{\circ}$ W.

### 3.3 Seasonal variability of the upwelling and surface currents

Near the Chilean coast north of  $36^{\circ}$ S, both the offshore Ekman transport and the Ekman pumping due to the wind stress curl are predominantly upwelling favorable (Figure 3.2a,b). South of  $36^{\circ}$ S, poleward wind stress induces downwelling during winter. Slight downwelling is also induced by the anticyclonic wind stress curl near  $38^{\circ}$ S during much of the winter and spring. Vertical transport associated with Ekman transport is about one order of magnitude larger than the transport related to Ekman pumping in most of the region. But during summer, between  $32^{\circ}$ S and  $37^{\circ}$ S, the low level atmospheric jet centered around 150 km offshore reaches maximum intensities and the Ekman pumping is also intensified, reaching about one half of the Ekman transport. Figure 3.2d shows the vertical transport near the coast integrated between  $27^{\circ}$ S and

40°S, and the vertical transport obtained from the ROMS model. Model vertical transport agrees well with the vertical transport estimated from the Ekman transport plus Ekman pumping, with a maximum value of  $\sim 1.7$  Sverdrup (Sv) during summer and a minimum of  $\sim 0.6$  Sv in winter. If we consider the total wind-driven upwelling, model values are slightly lower (higher) than those estimated from the satellite wind stress during the first (second) half of the year. Note that model vertical velocities may also be affected by other mechanisms, particularly by mesoscale eddies, which become important south of 30°S [e.g., *Hormazabal et al.*, 2004]. Nevertheless, those values should tend to vanish when we integrate in a large area that may include cyclonic and anticyclonic eddies.

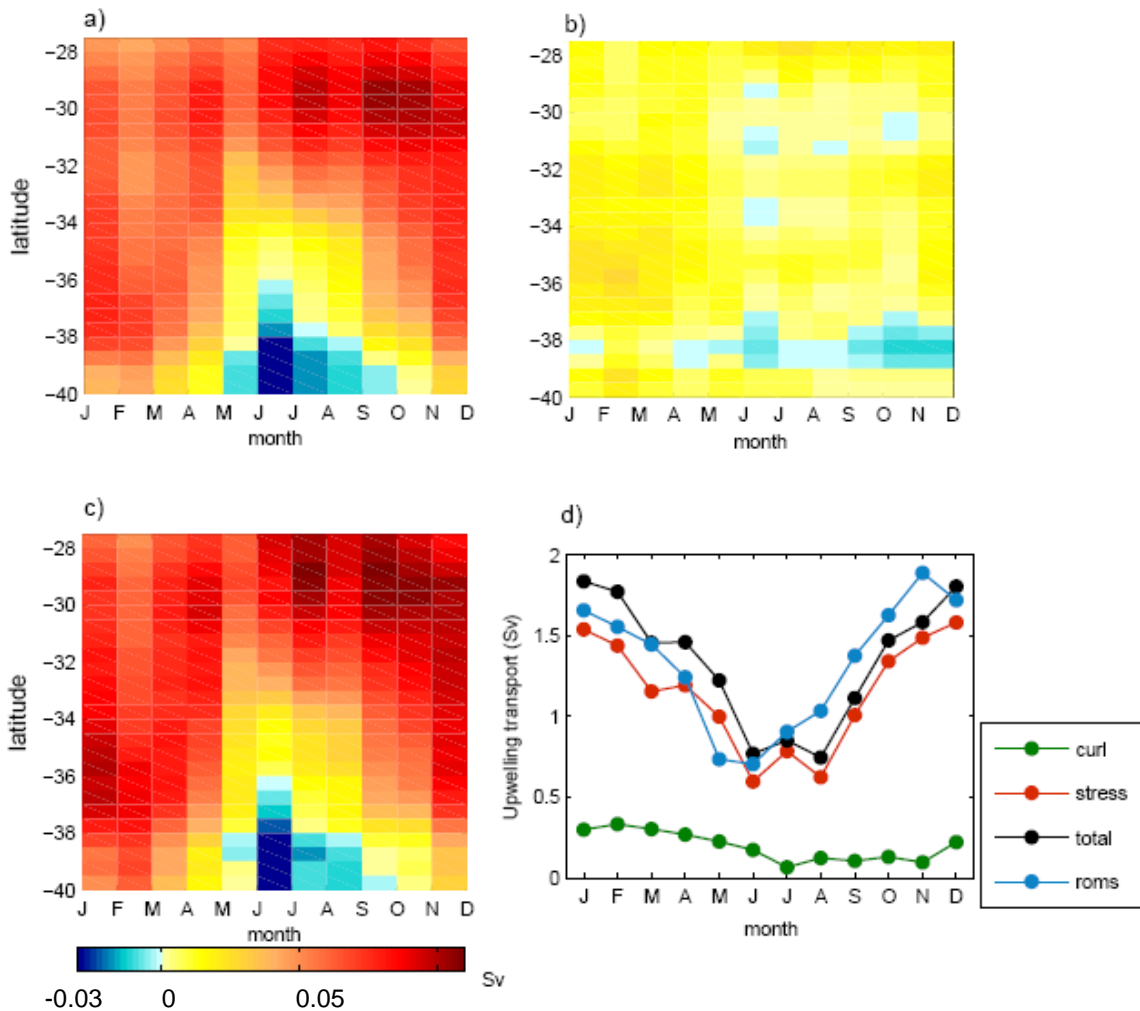


**Figure 3.2.** Contributions of the Ekman transport and Ekman pumping to the vertical transport near the coast (within the first 150 km offshore). a) Seasonal vertical transport associated with Ekman transport, b) seasonal vertical transport associated with Ekman pumping, c) seasonal total wind induced vertical transport (Ekman transport + Ekman pumping). d) Vertical transport (Sv) associated with Ekman transport (red), Ekman pumping (green), total wind induced vertical transport (Ekman transport + Ekman pumping, black) and simulated vertical velocities at 30 m depth (blue). Vertical velocities were integrated between 27° and 40°S, and the first 150 km offshore.

These results show that Ekman transport is the main mechanism forcing coastal upwelling since Ekman pumping –related to the wind stress curl– is always much smaller off central Chile. Nevertheless we are probably underestimating the wind stress curl due to the resolution of QuikScat data, in particular near the coast, where the curl is negative (upwelling favorable). In

fact, *Capet et al.*, [2004] infer that present wind analyses do not adequately represent the speed drop-off near the coast. Specifically, off central Chile the cross-shore wind gradient may be large due to the low-level atmospheric jet observed during upwelling seasons [cf., *Muñoz and Garreaud*, 2005]. Differences in the wind stress curl near the coast may also influence the coastal circulation [*Capet et al.*, 2004].

The surface geostrophic flow estimated from both satellite altimetry and model sea level shows a well defined equatorward current with a jet like-structure during spring and summer (Figure 3.3a,b). The jet remains close to the coast south of Punta Lavapie ( $\sim 37^\circ\text{S}$ ) with velocities larger than  $10 \text{ cm s}^{-1}$ . North of Punta Lavapie, the coast changes its orientation and the jet separates from the coast. Farther north, during summer, the jet bends to the northwest at around  $30^\circ\text{S}$ , remaining over the deep ocean. During fall the jet is still observed, but it is located farther offshore –with a core west of  $75^\circ\text{W}$ – between  $35^\circ\text{S}$  and  $39^\circ\text{S}$ . In contrast, during winter the equatorward flow is much weaker and disorganized, and a poleward flow develops close to the coast in the southern region, consistent with the predominant poleward wind stress found there (Figure 3.1).

The model reproduces reasonably well the coastal jet in the southern part of the domain and very importantly, the jet separation observed at Punta Lavapie ( $\sim 37^\circ\text{S}$ ), which subsequently forms the CTZ equatorward flow centered at  $75^\circ\text{W}$  (Figure 3.3b). Nevertheless, model velocities show more spatial structure than observations and larger values than that estimated from satellite altimetry. In addition, the model exhibits an intense coastal equatorward jet year-round within a narrow coastal strip ( $\sim 40 \text{ km}$ ), which can not be compared using satellite-derived geostrophic currents. During summer the model exhibits a surface poleward flow east of the CTZ jet (between  $27^\circ\text{S}$  and  $33^\circ\text{S}$ ) consistent with the PCCC, which was also suggested by three years of satellite-derived currents anomalies [*Strub et al.*, 1995], although it is not clearly distinguished in our longer record of surface geostrophic current (Figure 3.3a).

The jet-like stream observed during summer was originally described by *Fuenzalida et al.*, [2008] using maps of absolute dynamical topography combining satellite sea level height anomalies and mean ocean dynamic topography. They indicate that maximum values of the geostrophic velocities do not exceed  $10 \text{ cm s}^{-1}$ . In our case, we used a different ocean dynamic topography, but maximum equatorward speeds are similar to those found by *Fuenzalida et al.* [2008]. Equatorward speeds rarely exceed  $13.0 \text{ cm s}^{-1}$  (in fact, using weekly data only 5% of the summer equatorward velocities are larger than  $13.0 \text{ cm s}^{-1}$ ).

The seasonal cycle –estimated by least-square fitting of an annual harmonic– of the meridional geostrophic currents has maximum amplitude near the coast south of  $35^\circ\text{S}$ , with maximum equatorward values occurring during February and March for both satellite altimetry and in the model (Fig. 3.4b,c). In this region the maximum amplitude ( $\sim 5 \text{ m s}^{-1}$ ) of the wind is also observed (Figure 3.4a). In the northern part of the study region the annual cycle of the meridional geostrophic current is not significant (white regions); i.e. the correlation coefficients between the adjusted annual harmonic and the observed (or model) time series are not significantly different from zero (at the 95% level of confidence according to the *t-test*). On the other hand, the phase observed in the satellite and model geostrophic current (arrows in Figure 3.4b,c) are similar. In both cases the phases suggest an offshore propagation of the meridional current. The large amplitude observed offshore north of Punta Lavapie ( $\sim 37^\circ\text{S}$ ) is directly related to the presence of the CTZ jet during spring and summer.

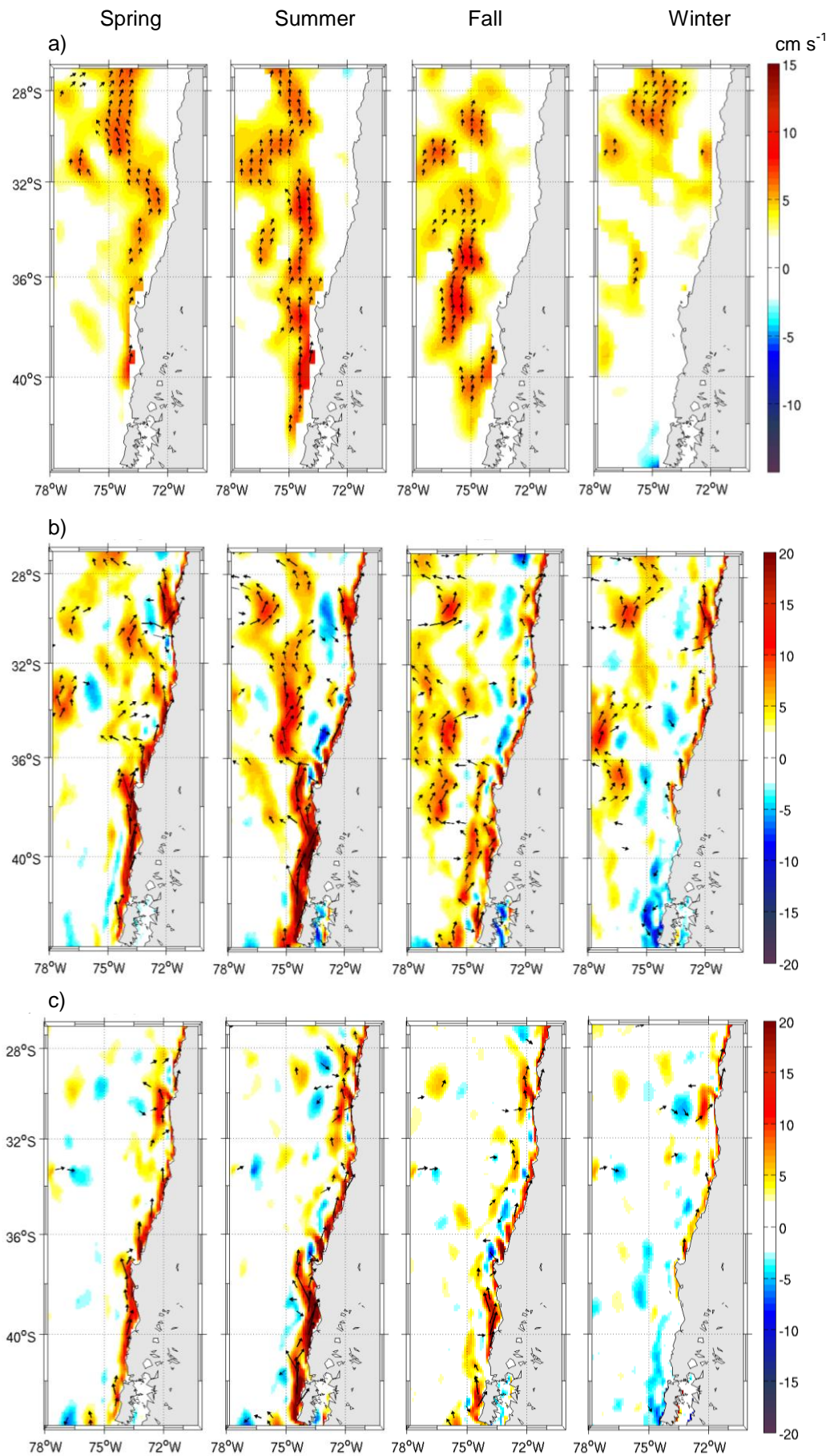


**Figure 3.3.** Seasonal climatology of the surface geostrophic meridional currents obtained from: a) a combination of mean surface geostrophic currents based on CARS temperature and salinity climatology (assuming a level of no motion at 1000 db) and geostrophic current anomalies derived from AVISO altimetry. b) ROMS (control simulation) surface geostrophic meridional current and c) ROMS (no-curl simulation) surface geostrophic meridional current. Vectors are shown only if the current speeds are higher than  $5 \text{ cm s}^{-1}$ .

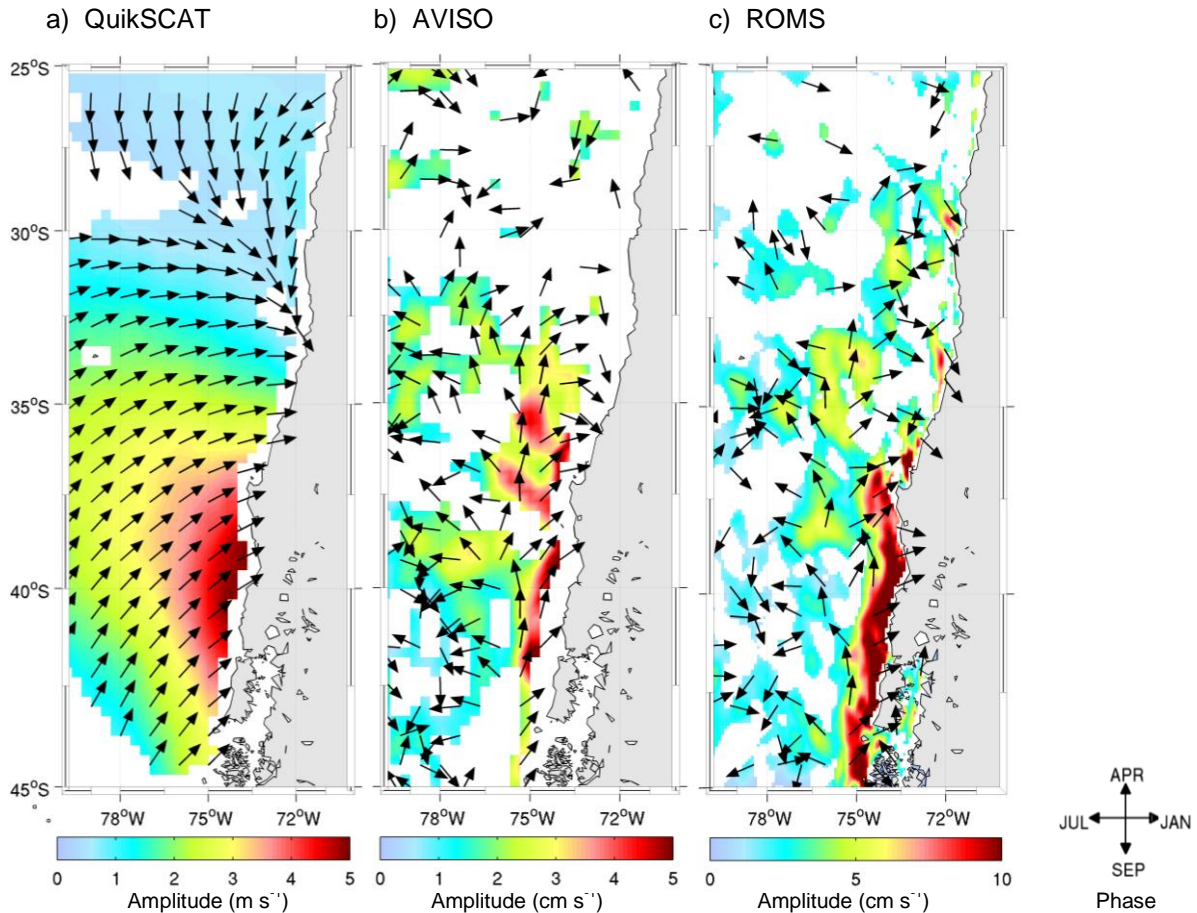


**Figure 3.4.** Amplitude (colors) and phase (vectors) of the annual cycle of the a) Meridional wind speed (QuikSCAT), b) observed surface geostrophic meridional current (AVISO) and c) model surface geostrophic meridional current. Results are plotted only when the adjusted annual harmonic of the wind and the observed (or model) time series of currents are significantly correlated using a *t-test* at the 95% level of confidence. White regions show not significant correlations.

Spectra for the wind stress and surface geostrophic currents were calculated based on the corresponding time series and then averaged inside a box of  $1^\circ$  of latitude and  $5^\circ$  of longitude starting with the valid data near the coast. The relative importance of the annual cycle of the wind stress and the meridional surface current from the model and altimetry increases with latitude (Figure 3.5). In fact, in the northern part of the domain (i.e. north of  $35^\circ S$ ), the spectral maxima for the surface geostrophic flow are near the semiannual frequency, with no significant peaks at the annual frequency. The spectral maxima for this variable are near the semiannual frequency. In contrast, south of  $36^\circ S$  all the spectra are dominated by an annual peak.



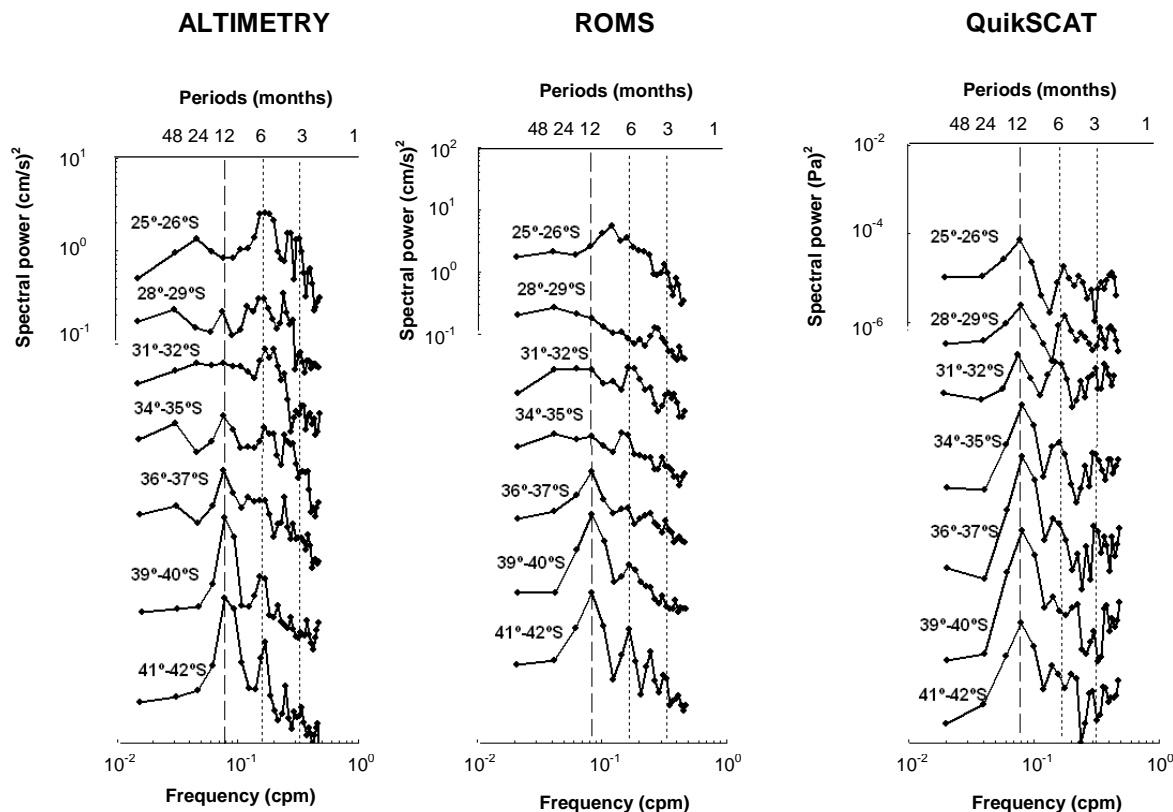


**Figure 3.5.** Spectra of the meridional geostrophic surface currents from altimetry data (AVISO) and model data (ROMS), and the spectra of the meridional wind stress from QuikSCAT data at different latitudes. The spectra inside a “box” of  $1^\circ$  latitude and the first  $5^\circ$  longitude offshore were averaged. The dashed line indicates the annual period and the dotted lines indicate the 6 and 3 months periods.

### 3.4 Vertical structure of the coastal transition zone (CTZ) jet

In this section we present the vertical structure of the CTZ jet through vertical sections of the simulated meridional currents. Because the CTZ jet is fully developed during summer (DJF), only summer means at different latitudes are presented (Figure 3.6). The axis of the CTZ jet observed during summer clearly exhibits its westward displacement as the flow travels northward (see red arrows in Figure 3.6). The vertical extension of the CTZ jet increases at lower latitudes reaching values close to  $10 \text{ cm s}^{-1}$  at about 200 m depth at  $30^\circ\text{S}$  and  $33^\circ\text{S}$ , transporting approximately 3.2 Sv. This deepening may represent the process referred as “barotropization”, in which the jet separates from the coast at Punta Lavapie and undergoes baroclinic instability, deepening through the transformation of kinetic energy from vertically sheared flow into the vertical mean flow [Haney *et al.*, 2001].

In Table 2 we quantify the meridional transports (Sv) for the four main alongshore flows off central Chile at four latitudes. We also estimate the *Humboldt* transport as the large scale equatorward flow between 200 and 600 km offshore and 600 m depth. Transport due to the simulated CTZ jet was calculated only for the summer season, when it is well developed. At  $30^\circ$  and  $33^\circ\text{S}$  the transport of the CTZ jet during summer is a significant proportion (60-80%) of this *Humboldt* transport.

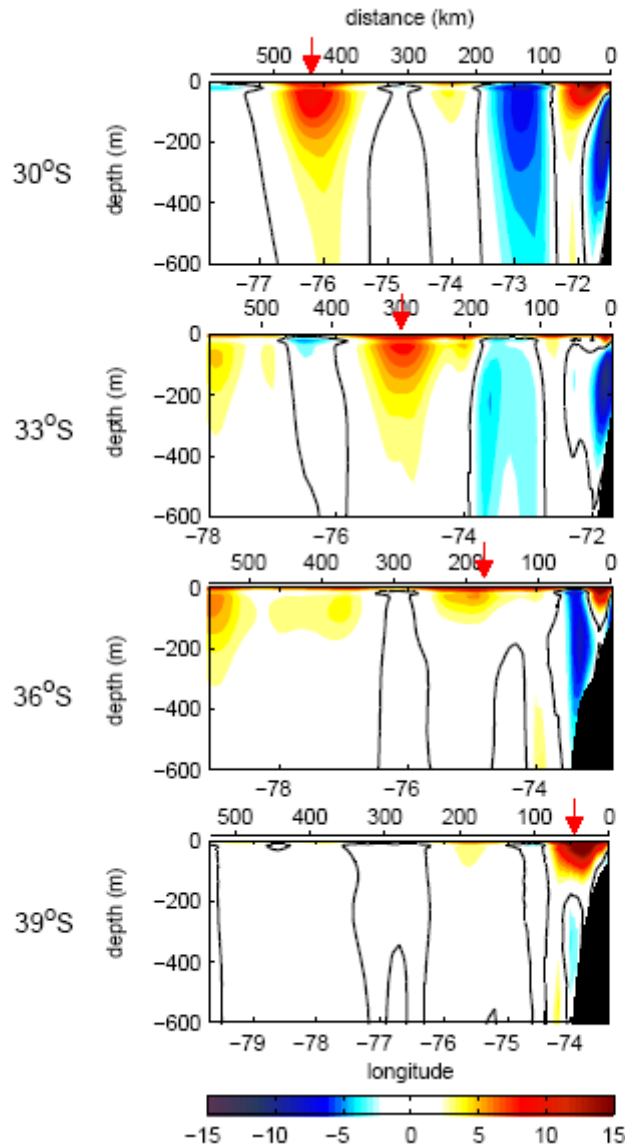


**Figure 3.6.** Vertical sections of the model meridional currents ( $\text{cm s}^{-1}$ ) at different latitudes during summer (DJF). The red arrows indicate the axis of the CTZ jet. Note that south of  $37^\circ\text{S}$  the CTZ jet can not be separated from the CCC.

Transport calculations for the other major flows off central Chile (Table 2) show that the CCC exhibits a distinct seasonal cycle in the southern part of the domain, being more intense during spring-summer and weaker in fall-winter. This seasonality is directly related to the upwelling dynamics [e.g., *Aiken et al.*, 2008]. The PCU shows more seasonality at  $33^\circ\text{S}$  and  $36^\circ\text{S}$  with higher values during spring-summer and summer-fall, respectively. At  $39^\circ\text{S}$  the PCU is considerably weaker and it is not present during spring. According to model results the PCCC does not show strong seasonality, but is very weak (velocities  $< 3 \text{ cm s}^{-1}$ ) during spring at  $33^\circ\text{S}$ .

**Table 2.** Seasonal transport (Sv) of the major currents of the Chile-Perú Current System, obtained integrating to 600 m deep.

		CCC	PCU	PCCC	Humboldt	CTZ jet <sup>1</sup>
<b>30°S</b>	Fall	0.77	-1.06	-1.78	3.15	-
	Winter	1.73	-0.86	-1.99	3.60	-
	Spring	1.96	-0.87	-0.90	3.01	-
	Summer	1.13	-0.81	-2.27	3.96	3.16
<b>33°S</b>	Fall	0.51	-0.81	-1.49	4.70	-
	Winter	0.78	-0.61	-1.29	3.57	-
	Spring	1.09	-0.70	-0.26	4.97	-
	Summer	0.54	-0.73	-1.39	5.18	3.17
<b>36°S</b>	Fall	0.47	-0.68	-	3.75	-
	Winter	0.39	-0.55	-	3.85	-
	Spring	1.05	-0.43	-	3.44	-
	Summer	0.47	-0.85	-	4.44	1.37
<b>39°S</b>	Fall	0.62	-0.34	-	1.86	-
	Winter	0.36	-0.20	-	2.14	-
	Spring	1.20	-	-	2.01	-
	Summer	1.07 <sup>2</sup>	-0.17	-	1.54	1.07 <sup>2</sup>

<sup>1</sup> The transport of the CTZ jet is only estimated during summer when it is fully developed.

<sup>2</sup> South of 37°S, the CTZ jet cannot be separated from the CCC.

### 3.5 The role of wind stress curl in the CTZ jet variability

In the large scale context, the wind stress curl field (Figure 3.1) suggests, through Sverdrup dynamics, a southward transport during spring and summer close to the coast (within the first 150 km) and northward transport offshore. Sverdrup transport estimated directly from the wind stress curl agrees well with the model meridional transport (Figure 3.7). Estimates of geostrophic transport based on hydrographic data from WOCE P06 line at 32°S have values of ~8 Sv to 90°W [Shaffer *et al.*, 2004], which also agree well with our model meridional transports. However, even though the large scale Sverdrup transports are consistent with the model transports, the CTZ jet itself could be controlled by other dynamics that also involve the wind stress curl [Castelao and Barth, 2007].

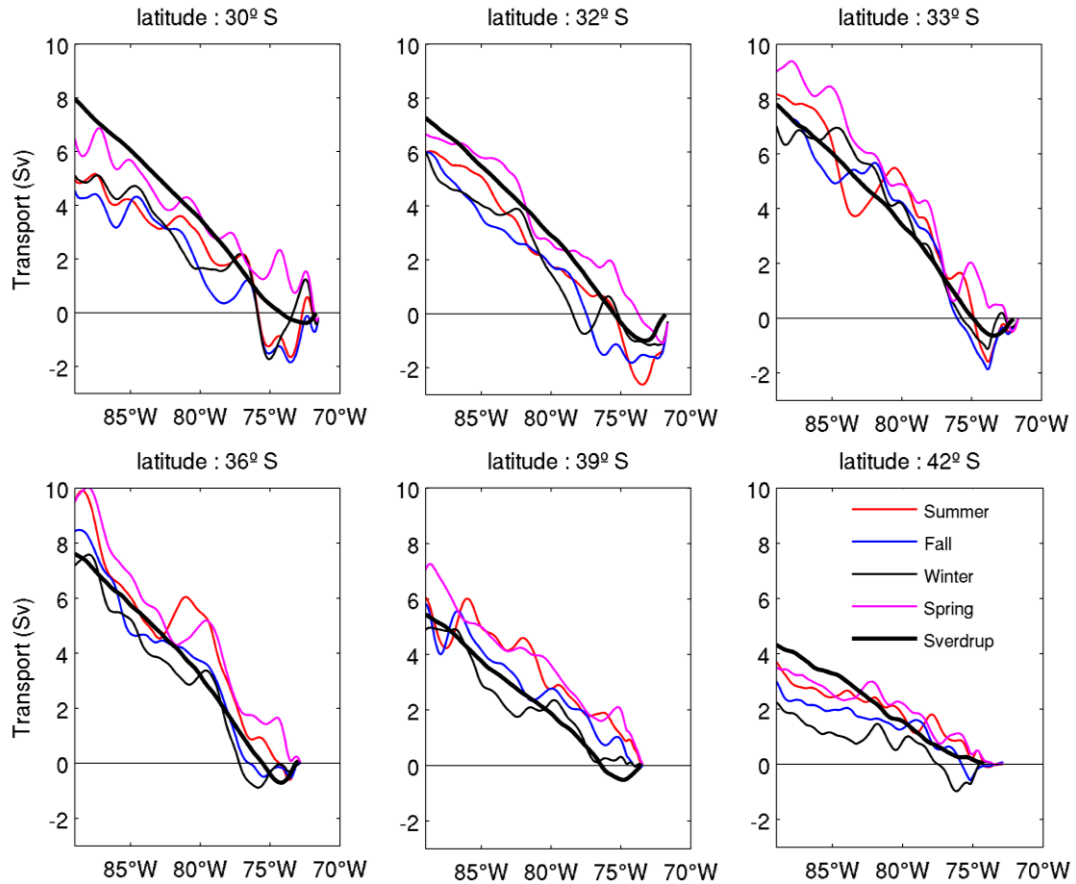


**Figure 3.7.** Seasonal surface transport (0-600 m depth) integrated westward along different latitudes from the Chilean coast based on model results. The thick black line shows the Sverdrup transport estimated directly from the annual mean wind stress curl (QuikScat data).

In order to evaluate the impact of the wind stress curl on the CTZ jet dynamics, we used a no-curl simulation (see methodology section). Comparing results between both simulations (i.e. the control and the no-curl runs) we found major differences only far from the coast (Figures 3.3b and 3.3c). The CCC remains close to the coast and a poleward flow is developed during winter in the southern region, consistent with the wind stress there. The vertical structure of currents during summer at 30°S shows that both the CCC and the PCU are similar in both simulations (Figure 3.8). The poleward and the equatorward flows, associated with the PCCC and the CTZ jet respectively, in the control run, are still present in the no-curl simulation; but their transports are reduced in magnitude. Notably, the equatorward jet-like flow observed offshore in the satellite data and in the control run, is not observed in the no-curl simulation. It is worth noting that boundary conditions may indirectly be imposing a flow by the use of climatological temperature and salinity fields. At 36°S, only the CCC is similar in both simulations. The PCU is weaker in the no curl simulation, but it still outcrops the surface as in the control run. The equatorward flow observed offshore of 100 km from the coast at 36°S is considerably weaker in the no curl simulation.

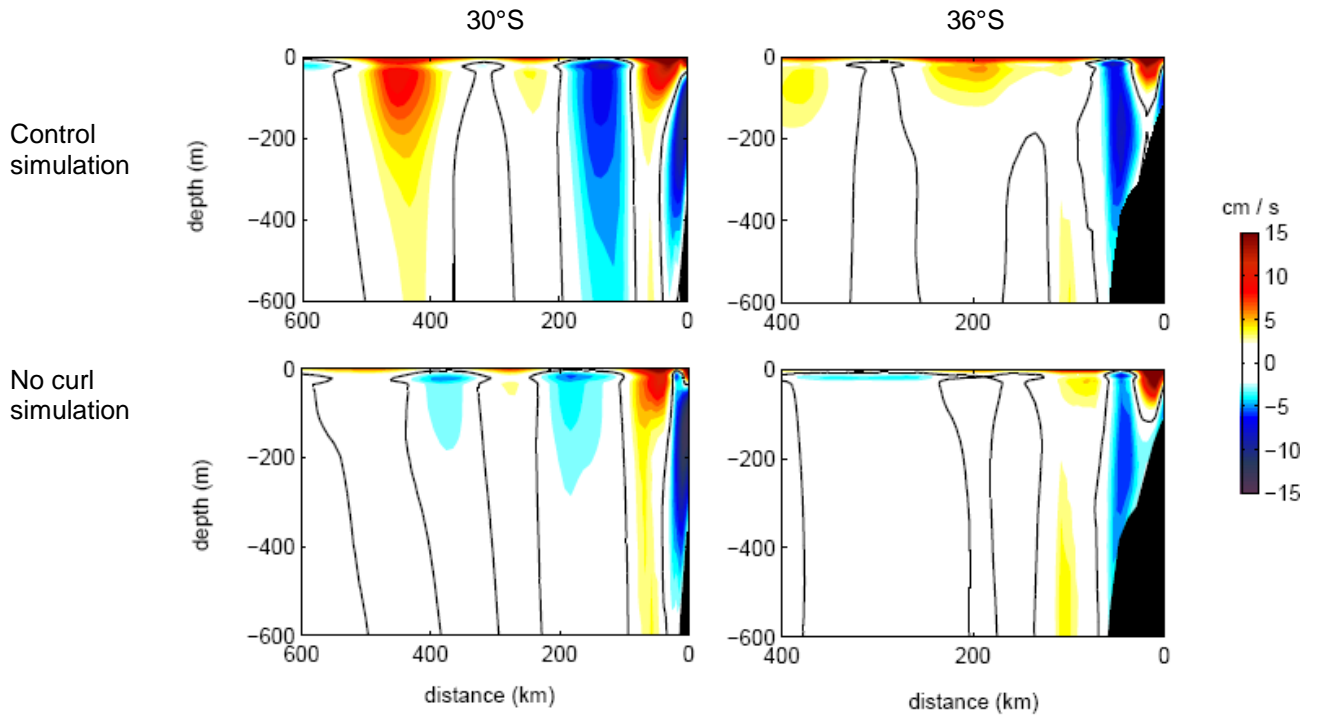


**Figure 3.8.** Vertical sections of the summer mean meridional flow at 30°S (left) and 36°S (right) obtained from the control (upper) and the no curl (bottom) simulations.

These results show that the oceanic CTZ jet north of Punta Lavapie observed during spring and summer is not present in the no-curl simulation. In the satellite observations and in the control run the coastal jet observed south of 37°S separates from the coast at Punta Lavapie to form the CTZ jet. The separation of the coastal jet seems to be directly related to the wind stress curl. Indeed, the axis of the CTZ jet tends to follow the contour of zero wind stress curl from 37°S to 32°S (Figure 3.9). But farther north the CTZ is observed west of the zero wind stress curl during spring. According to the Sverdrup balance it is expected that the long-term mean position of the maximum surface current would be located near the contour of maximum anticyclonic curl. However, this contour is located far westward (more than 200 km) from the CTZ jet axis.

On the other hand, the zero wind stress curl moves slightly offshore and extends southward from spring to summer, following the displacement of the axis of the atmospheric low-level jet present in the region from around 38°S to 27°S [Garreaud and Muñoz, 2005]. Note that the axis of the CTZ jet is observed just west of the zero wind stress curl in summer. The possible mechanism relating the wind stress curl and the CTZ jet are discussed below.

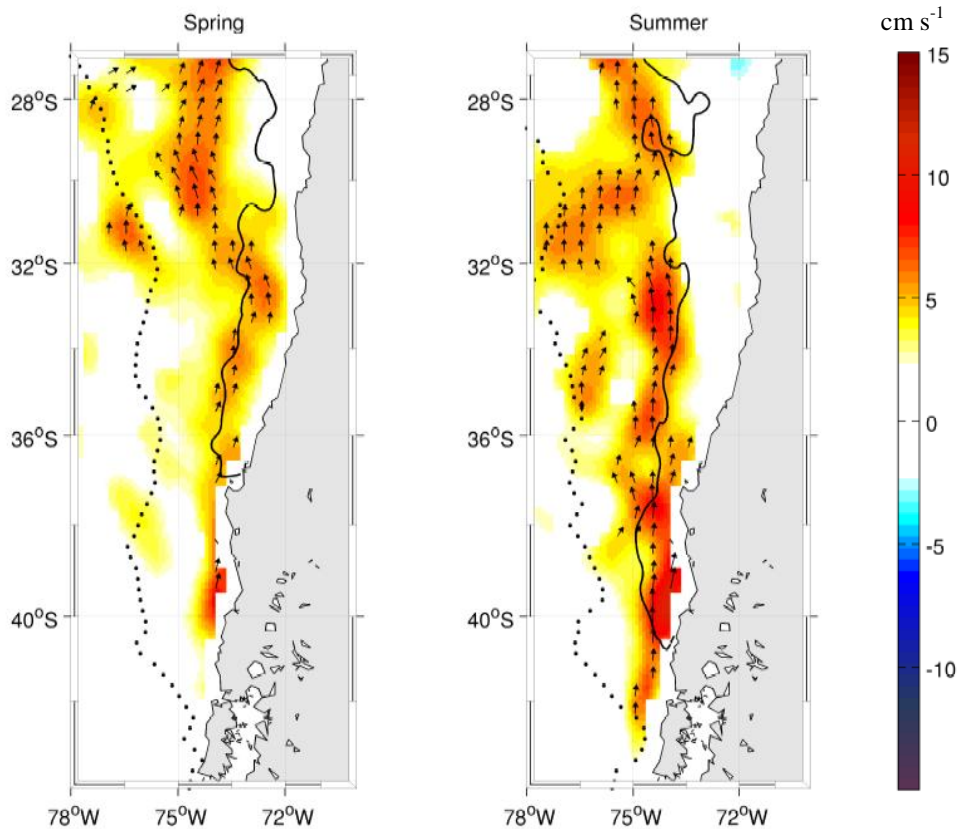


**Figure 3.9.** Spring and summer climatology of the observed surface geostrophic meridional currents from CARS 2006 plus AVISO (colors) as in Figure 8a. The continuous line indicates the zero wind stress curl and the dotted line indicates the position of the maximum values of the anticyclonic wind stress curl.

### 3.6 Discussion

Studies in the Pacific eastern boundary current systems provide examples of upwelling jets that separate from the coast near capes to become oceanic jets [e.g. *Barth and Smith, 1998; Barth et al., 2000*]. Insights into this process were obtained by numerical experiments [*Castelao and Barth, 2006, 2007; Mesias et al., 2003*]. These model analyses showed that capes play a crucial role for separation of the coastal jet, and that the nonlinear terms in the equations that govern the flow are increased in the vicinity of a coastline perturbation or where the bottom topography orientation changes. In contrast, our two simulations (control and no-curl runs) used the same topography, but the CTZ jet was only observed when the wind stress curl was present in the surface forcing. This result shows that the wind stress curl plays a major role in the dynamics of the CTZ jet. Although the cape may be important for the separation of the coastal jet at Punta Lavapie, by itself it could not generate the CTZ jet observed off central Chile. Using an  $f$ -plane model, *Castelao and Barth [2007]*, showed that the intensity of the wind stress is much less important than the position of the zero wind stress curl, which controls the location of the offshore jet. The mechanism proposed by those authors is that the spatial pattern of the wind stress curl generates a couplet of upwelling and downwelling regions (on each side of the zero wind stress curl line) that modify the density field and, thus, the position and intensity of the geostrophically balanced jet. This process is consistent with our model observations, which find a

region of cyclonic curl onshore (upwelling) and anticyclonic curl offshore (downwelling) of the CTZ jet. The jet follows (approximately) the zero wind stress curl. Hence, the seasonal variability of the CTZ jet is related to the seasonal variability of the Ekman pumping process superimposed on a large scale context dominated by the Sverdrup dynamics.

Tracing these processes into the atmosphere, the positions of the zero wind stress curl and the CTZ jet correspond approximately to the climatological position of the core of the low-level atmospheric jet that is rooted at Punta Lavapie. This wind jet, in turn, is determined by the temperature gradient in the lower troposphere, which is maximum downstream of the major capes along the coast [Rahn *et al.*, 2011]. Thus, Punta Lavapie may indirectly affect the location of the CTZ jet separation, by generating a recurrent atmospheric coastal wind jet during summer. The wind jet then impacts the upper-ocean circulation via the wind stress curl field.

Major eastern boundary current systems are driven by predominant equatorward winds, which force coastal upwelling, equatorward surface flows and a poleward undercurrent [e.g., Hill *et al.*, 1998]. In this context, it is worth mentioning a brief comparison between the California and Humboldt Current System, particularly on the CTZ jet. The Coastal Transition Zone experiment conducted off northern California ( $\sim 39^\circ\text{N}$ ) provided evidences of a strong surface alongshore jet flowing equatorward [Brink and Cowles, 1991]. During spring and summer the model fields strongly support the concept of a meandering jet, which carries most of the surface transport in this period [Strub *et al.*, 1991]. The equatorward CTZ jet is narrow (50–75 km) and exhibits its maximum values at the surface ( $> 50 \text{ cm s}^{-1}$ ), decreasing to velocities of  $10 \text{ cm s}^{-1}$  about 200 m deep. Its equatorward transport is  $\sim 4 \text{ Sv}$  and it may be identified as the core of the California Current [Huyer *et al.*, 1991b]. The spatial pattern and the equatorward transport associated with the CTZ jet during spring and summer in the California Current agrees well with the CTZ jet described here off central Chile as a major component of the Humboldt Current. This jet transports about  $3 \text{ Sv}$ , which is  $\sim 1 \text{ Sv}$  smaller than its counterpart in the California Current System. Using satellite height fields Strub and James [2000] define a conceptual model of the seasonal evolution of the surface circulation in the California Current System. During spring and summer, an equatorward flow develops close to the coast ( $\sim 123^\circ\text{W}$ ), with an initial latitudinal structure that responds to the latitudinal distribution of the equatorward winds. This jet moves offshore from spring to fall to around  $130^\circ\text{W}$ , where the jet weakens and dissipates. The westward velocity propagation of the jet is consistent with the Rossby wave dynamics. A similar seasonal cycle is found in the Humboldt Current System. The jet develops during spring and summer, responding to the wind forcing, and continuously moves offshore, becoming a more disorganized structure in winter. However, the CTZ jet of the Humboldt Current seems to be formed by the coastal jet separation observed at Punta Lavapie.

### 3.7 Conclusions

In this work we have characterized the alongshore flows off central Chile, particularly the coastal transition zone jet and its seasonal variability, using geostrophic velocities derived from satellite altimetry and from simulations using the regional ocean model (ROMS). We perform two simulations that only differ in their surface wind forcing. The standard case uses long-term monthly mean wind stress from QuikSCAT and the second uses a wind stress field without curl (the “no curl” simulation). Both the observed and model geostrophic surface currents show a well defined equatorward flow with a jet like-structure which develops during spring and summer and

moves westward as the year progresses. In fall the jet is located offshore and becomes weaker. In contrast, during winter the flow is in general much weaker and a poleward flow is observed close to the coast in the southern region. There, the amplitude of the annual cycle of the geostrophic current is larger, consistent with the maximum amplitude of the annual cycle of the wind stress.

The model is able to reproduce the major features observed off central Chile, such as a coastal surface equatorward jet, a poleward undercurrent with a core over the upper slope, and a countercurrent located westward of the coastal jet. In addition, the model reproduces the coastal jet separation at Punta Lavapie ( $\sim 37^\circ\text{S}$ ) during summer to become the offshore CTZ jet, which is also observed by altimetry data. This striking feature is not replicated by the surface geostrophic currents in the no-curl simulation, so the CTZ is not present during the spring and summer off central Chile. Although Sverdrup transport was similar to the model transport in a large scale context, the CTZ jet is not located where the positive wind stress curl is maximum (Sverdrup transport is maximum), which is found farther offshore. In contrast, the position of the CTZ jet seems to be related to the zero wind stress curl contour, which corresponds to the climatological location of the axis of the low-level atmospheric jet. Thus, both the oceanic and the atmospheric jets are aligned about the same axis. These results illustrate the importance of the offshore upwelling/downwelling associated with the Ekman pumping, which tilts the isopycnals upward, creating a northward flow through thermal wind balance. Our results show that the cape could be important for separation of the coastal jet at Punta Lavapie, but is not enough to generate (by itself) the CTZ jet observed off central Chile. Indeed, the presence of Punta Lavapie and the abrupt change in coastline orientation downstream of it seem fundamental in producing a recurrent and intense atmospheric low-level coastal wind jet in this area, which in turn produces the marked change in wind stress curl near the coast and offshore.



## Chapter 4

### Surface ocean response to synoptic-scale variability in wind stress and heat fluxes off south-central Chile.

#### 4.1 Introduction

Upwelling of cold, nutrient rich waters along much of the Chilean coast induces high primary productivity and maintains one of the major fisheries of the world [e.g., *Rutllant and Montecino*, 2002; *Food and Agriculture Organization*, 2004]. Coastal upwelling is in turn forced by alongshore, southerly (equatorward) winds, being particularly strong around major capes at 30°S (Punta Lengua de Vaca), 33°S (Punta Curaumilla) and 37°S (Punta Lavapié) because of topographic / bathymetric effects [*Figueroa and Moffat*, 2000]. Although the basic features of coastal upwelling, including their regional distribution and seasonal variability have been described elsewhere [e.g., *Figueroa and Moffat*, 2000; *Leth and Shaffer*, 2001; *Blanco et al.*, 2001; *Sobarzo et al.*, 2007], there is less information on the surface ocean response to atmospheric jet events, partly because of the scarcity of *in situ* data. Using satellite observations *Renault et al.*, [2009] studied the effect of the atmospheric low-level jet on sea surface temperature (SST) off central Chile (30°S), but the blind zone close to the coast was an important limitation to capture the upwelling response to the wind forcing which is particularly important within the first 20 km off the coast [e.g., *Perlin et al.*, 2007; *Aiken et al.*, 2008]. Modeling efforts have also been conducted to understand upwelling and ocean circulation off central Chile [*Batteen et al.*, 1995; *Leth and Shaffer*, 2001; *Mesias et al.*, 2001; *Mesias et al.*, 2003; *Leth and Middleton*, 2004, *Aiken et al.*, 2008]. However, most of these studies have used climatological (long-term-mean) wind data to force an ocean model, perhaps losing an important source of variability, particularly south of 35°S in austral summer. Only *Mesias et al.*, [2001] and *Aiken et al.*, [2008] used daily wind data, but the former utilized a coarse horizontal resolution ( $2.5^\circ \times 2.5^\circ$  lat-lon grid) and the latter applied a spatially homogeneous wind stress field recorded at a coastal station. The lack of spatial structure of the near-shore winds in both studies may strongly influence the patterns of the circulation and SST [*Capet et al.*, 2004]. Recently, *Renault et al.*, [2012] modeled the upwelling response to an atmospheric low-level jet event occurred in spring off central Chile (30°S), focusing on the spatial variability of the forcing winds field.

Here, we used the Regional Ocean Modeling System (ROMS) [*Shchepetkin and McWilliams*, 2005] off Chile to investigate the impact of the atmospheric quasi-weekly low-level jet events on the surface ocean through wind-stresses and heat fluxes forcing. Three runs of the model were forced by different surface conditions. A climatological run was performed using long-term-mean monthly wind-stresses, similar to previous studies. The other two simulations were forced by daily wind-stresses (momentum fluxes), but only one of them was allowed for day-to-day changes in heat fluxes. This experimental set up allows us to gauge the nature and magnitude of the surface ocean variability induced by varying surface heat fluxes and wind stresses separately. Although the model domain extends along most of the Chilean coast (25°-45°S) and the runs span 8 full years, we focus our study off south-central Chile (35°-40°S) during austral summer, when there is significant synoptic variability in the wind superimposed on a mean, upwelling-favorable flow (Figure 1.1).

## 4.2. Model configuration and experimental setup

To analyze the effect of the synoptic-scale variability in wind stresses and surface heat fluxes relative to a smooth mean seasonal variation, we performed three simulations (termed as *climatological*, *partial-synoptic* and *full-synoptic*) that only differ in their surface boundary conditions. The model domain spans from 25° to 45° S and from 70° to 80° W, where the northern, western and southern boundaries are open. The data used to nudge the circulation at the three open boundaries were the climatological monthly means of temperature and salinity obtained from the World Ocean Atlas 2005 [Locarnini *et al.*, 2006; Antonov *et al.*, 2006]. These data were used to estimate climatological values of geostrophic currents considering a level of no motion at 1000 m depth. The model horizontal resolution is 1/10°, which corresponds to ~7.9-10.1 km, with a 248 × 101 grid points. The bathymetry was extracted from the 2' resolution ETOPO database [Smith and Sandwell, 1997]. In spite of the fact that a pressure gradient scheme prevents large errors in the computation of horizontal pressure gradients in the ocean [Shchepetkin and McWilliams, 2003], the bathymetry was smoothed in order to maintain a “slope parameter”  $r = \nabla h / 2h < 0.25$  [Beckmann and Haidvogel, 1993]. The vertical grid has 32 vertical levels and stretching parameters of  $\theta_s=7$ ,  $\theta_b=0$  and  $hc=10$  m [Song and Haidvogel, 1994] allowing for a good representation of the surface coastal ocean. The time step was 13.3 min and outputs were averaged over each day.

The *climatological* run (CL) used long-term monthly mean wind stresses as a surface boundary condition, calculated from QuikSCAT data between 2000 and 2007, along with climatological monthly means of short and long wave radiation fluxes, air temperature, humidity, precipitation and wind speeds from the Comprehensive Ocean-Atmosphere Data Set (COADS) [Da Silva *et al.*, 1994] to calculate the surface heat and freshwater fluxes. This simulation was integrated for 10 years of 360 days each, repeating the mean annual cycle of the surface stresses. Statistics are analyzed for the last 8 years (the first 2 years are considered model spin-up). The *partial-synoptic* run (PS) was forced with daily wind-stresses from QuikSCAT, but used climatological COADS data to calculate surface fluxes, as in the CL run. Finally, the *full-synoptic* simulation (FS) is the experiment with more realistic surface boundary conditions (in terms of variability), because it is forced with daily QuikSCAT wind-stresses and daily surface variables to calculate heat and freshwater fluxes through bulk formulas while running the model. Time series with 6-hrs resolution from 2000 to 2007 of short and long wave radiation fluxes, air temperature, humidity and precipitation were obtained from the NCEP Climate Forecast System Reanalysis (CFSR) with a spatial resolution of 0.3° [Saha *et al.*, 2010]. This is a new coupled global NCEP Reanalysis at much higher temporal and spatial resolution than the previous Reanalysis [Kalnay *et al.*, 1996]. The major advantages of using this new data set is the coupling to the ocean during the generation of the 6-h fields and higher spatial resolution permitting analyses closer to the coast. These time series were daily averaged to calculate (through bulk formulas) surface heat and fresh water fluxes using the daily wind speeds from QuikSCAT in the same period. Both PS and FS had an initial two year integration using surface boundary forcing for the year 2000 (spin up period). Thus, we computed model statistics using 8 years, as in CL. Table 3 summarizes the three experiments performed in this study.

**Table 3.** Surface forcing and spatial/time resolution of the different simulations performed in this work.

Variable	Climatological (CL)	Partial-Synoptic (PS)	Full-Synoptic (FS)
Wind stress	Climatological QSCAT	Daily QSCAT	Daily QSCAT
Wind velocities	Climatological COADS	Climatological COADS	Daily QSCAT
Air temperature, relative humidity, precipitation, radiation	Climatological COADS	Climatological COADS	Daily NCEP
Boundary and initial conditions	Climatological WOA	Climatological WOA	Climatological WOA
Spatial resolution	1/10 °	1/10 °	1/10 °
Outputs time resolution	Daily	Daily	Daily

### 4.3. Inter-simulations comparison

#### 4.3.1 Mean circulation

The summer mean surface geostrophic flow obtained from both satellite altimetry and model sea level output, show a well defined equatorward direction with a jet-like structure (Figure 4.1). This flow has previously been described in Chapter 3 showing higher equatorward velocities during summer. The dynamics of the seasonal cycle of this jet is probably related to the spring/summer intensification of the wind-stress curl which produces surface equatorward current via thermal wind balance (Chapter 3). Since our three simulations contain the same seasonal variations in the wind-stress field (from QuikSCAT), we obtain a similar geostrophic equatorward flow with a mean value of  $\sim 12 \text{ cm s}^{-1}$  during summer. The simulated ocean jet exhibits a coastal separation near Punta Lavapié, an important feature that has been observed by hydrographic data [Letelier *et al.*, 2009] confirming previous simulations using the Princeton Ocean Model [Mesias *et al.*, 2001; Mesias *et al.*, 2003; Leth and Middleton, 2004]. The model velocities are somewhat higher than those characterizing satellite-derived surface currents ( $>10 \text{ cm s}^{-1}$ ) and show more spatial structure than observations, but it is important to note that altimetry data is smoothed in the process of creating gridded fields from multiple altimeters.

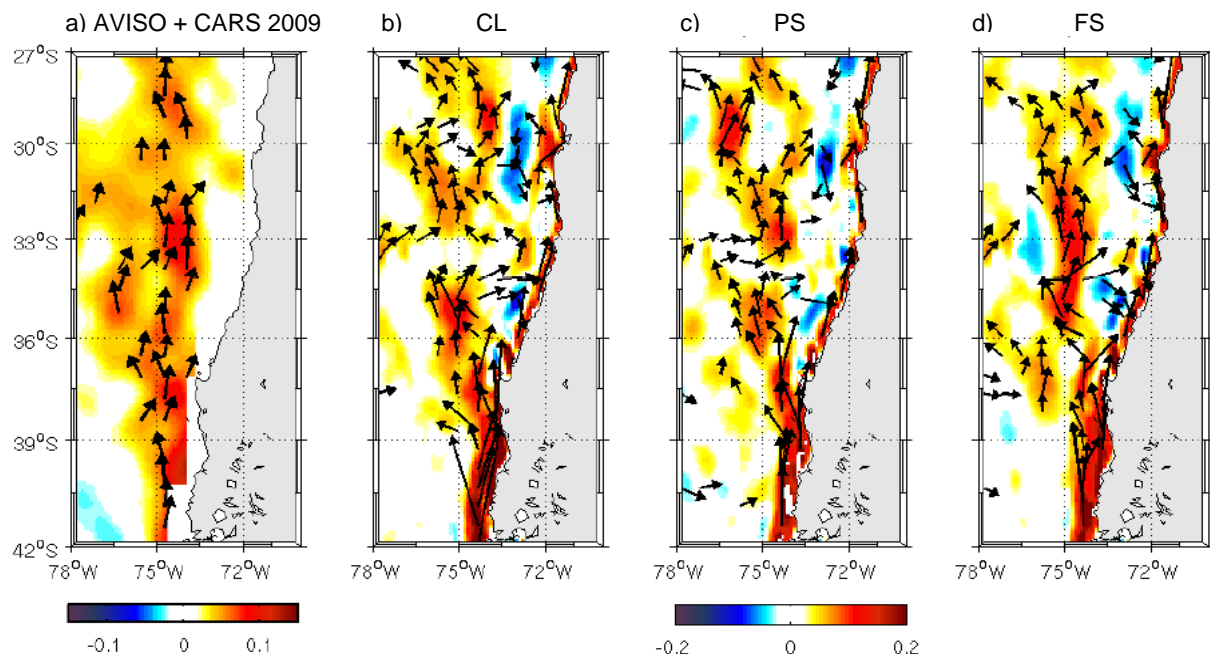


**Figure 4.1.** Climatology of the austral summer (DJF) surface geostrophic meridional currents (colors) obtained from a) a combination of mean surface geostrophic currents based on CARS temperature and salinity climatology (assuming a level of no motion at 1000 db) and geostrophic current anomalies derived from AVISO altimetry; and b), c), d) surface geostrophic meridional currents obtained from the three different simulations. Vectors are shown only if the current speeds are higher than  $5 \text{ cm s}^{-1}$ .

Further verification of the model performance in simulating the summer mean currents is provided in Figure 4.2 by the summer mean vertical profiles of zonal ( $u$ ) and meridional ( $v$ ) components along with their observational counterparts obtained from two ADCP (see section 2.1). As found before, mean profiles from our three simulations are very similar, their shapes agree well with the observations and they capture, in general, the reversal of the currents at different depths. The agreement is better in S18, within our target area, while farther north (COSMOS) the model profiles show an overestimation of the northward and eastward surface currents.

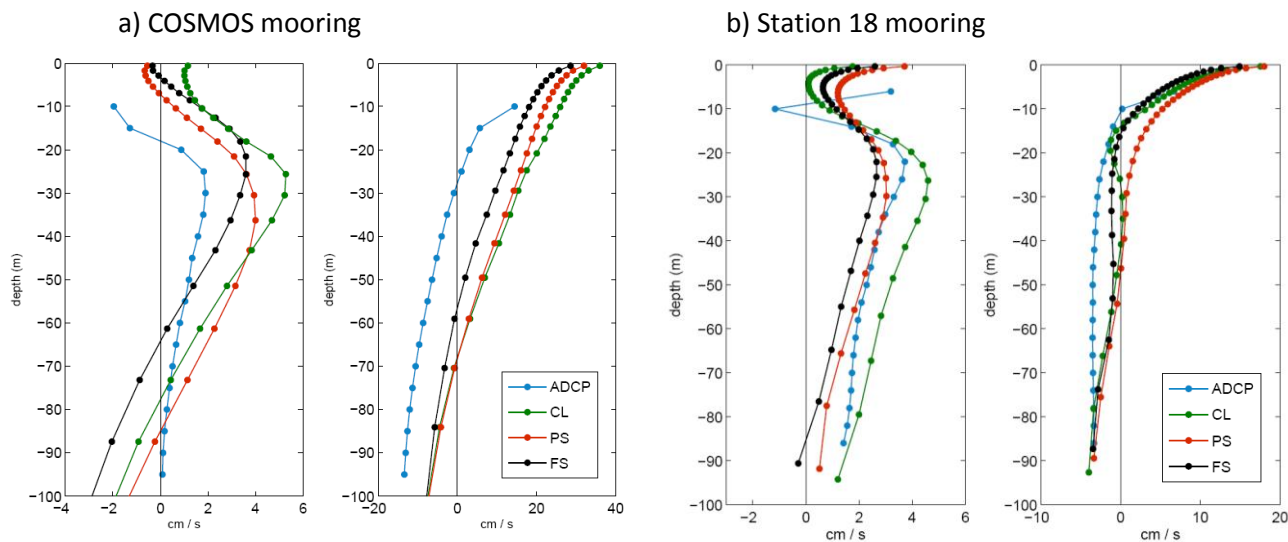


**Figure 4.2.** Summer mean profiles of the meridional ( $v$ ) and zonal ( $u$ ) currents at the moorings a) COSMOS and b) Station 18.

The model ageostrophic component of the surface flow was estimated subtracting the geostrophic currents (obtained from the model sea level) from the total currents. The summer mean of the ageostrophic currents is very similar in our three simulations (not shown) and, in general, agrees well with the surface Ekman currents obtained directly from the wind data (Figure 4.3a). Nevertheless friction, along with non linear interactions increase the ageostrophic currents close to the coast, departing from the Ekman theory [Ekman, 1905].

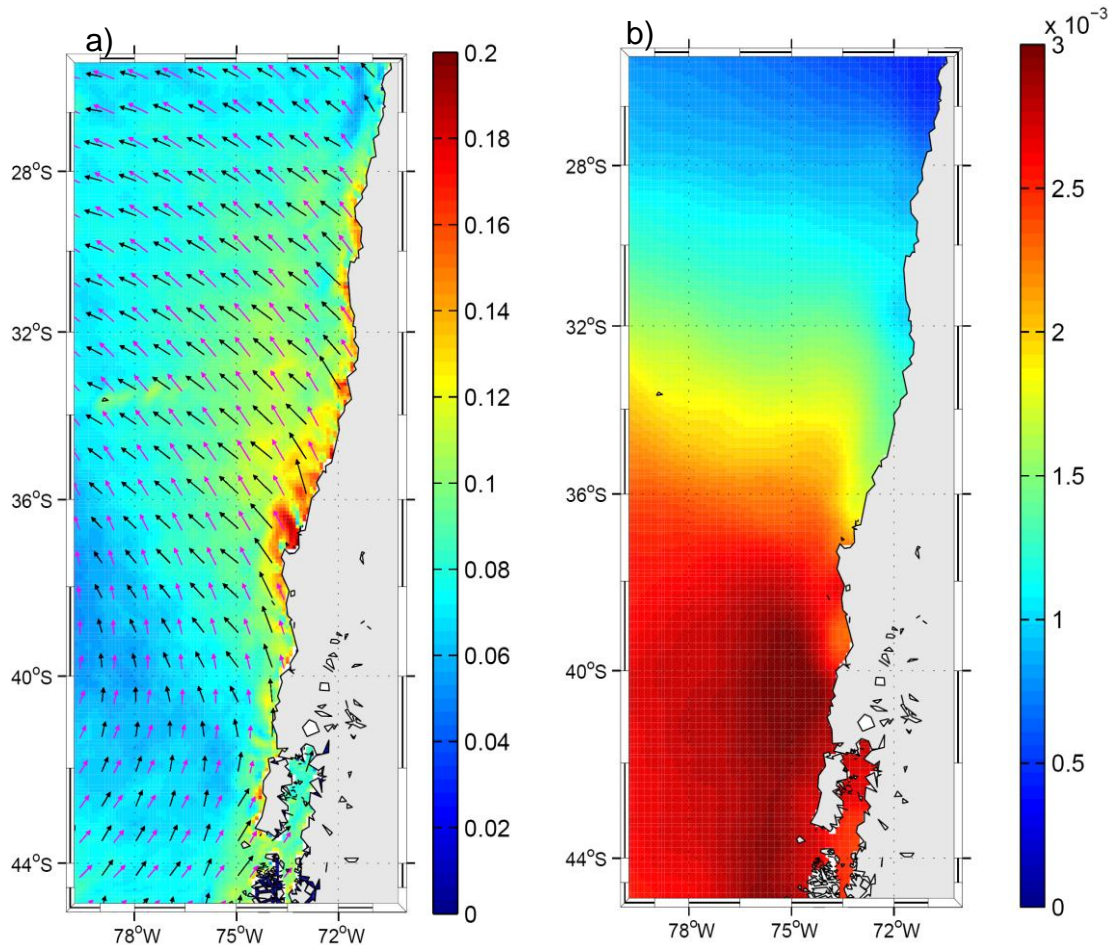


**Figure 4.3.** a) Summer mean of the surface ageostrophic currents speed (colors) and ageostrophic currents vector (black vectors) from the model (FS). Magenta vectors correspond to the summer mean of the Ekman surface currents obtained directly from the QuikSCAT wind stress field. b) Summer mean of the ageostrophic EKE obtained from the Ekman surface currents calculated from daily QuikSCAT wind stresses.

#### 4.3.2. Eddy Kinetic Energy (EKE)

Given the complexity in the EKE generation, surface EKE comparison between a model and data is a stringent test of the upper-ocean circulation [Capet *et al.*, 2008]. To test our simulations, we used the altimetry-derived geostrophic EKE (see section 2.1). The model outputs allow calculation of both total EKE (time average of the square of sea surface velocity departures from the mean) and geostrophic EKE (obtained from the sea-surface height anomalies).

In the offshore region, the spatial pattern of geostrophic EKE is similar in the three simulations and in agreement with satellite data (Figure 4.4). Higher values are found in a band rooted along the coast between 38-30°S. This region corresponds to the energetic coastal

transition zone off Chile described by *Hormazabal et al.*, [2004] using 7.5 years of AVISO data. The model and observed geostrophic EKEs show higher values in a band extending offshore in a SE-NW direction from Punta Lavapie, consistent with the coastal jet separation. The offshore values of the simulated geostrophic EKE are, however, 40-60% larger than the observations, an overestimation also found in other upwelling systems [*Veitch et al.*, 2010; *Capet et al.*, 2008]. This could be attributed, in part, to a smoothing of the gridded AVISO data. In particular, the observed geostrophic EKE minima close to the coast, could be attributed to the nearshore eddy scale ( $<50$  km) not resolved in the satellite data [*Ducet et al.*, 2000]. Furthermore, to the south of  $37^{\circ}\text{S}$  the simulations exhibit high geostrophic EKE ( $\sim 150 \text{ cm}^2 \text{ s}^{-2}$ ) in a coastal strip of about 70 km wide that is not present in the observations, probably because AVISO data are not reliable within the first  $\sim 50$  km offshore.

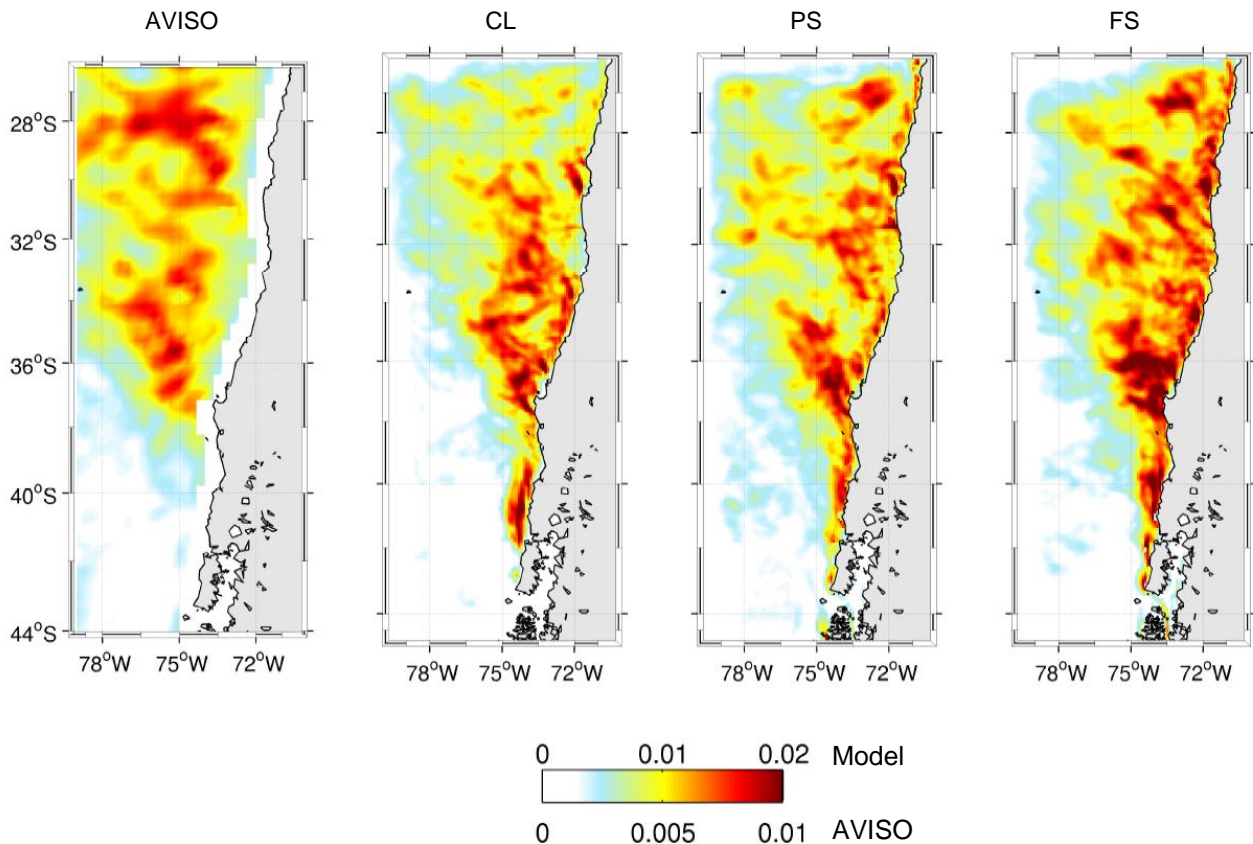


**Figure 4.4.** Summer mean of the geostrophic surface eddy kinetic energy (EKE,  $\text{m}^2 \text{ s}^{-2}$ ) derived from AVISO data and from the three different simulations.

In contrast to the geostrophic EKE, the ageostrophic kinetic energy (obtained from the ageostrophic currents) is significantly different between CL and PS (Figure 4.5). The simulations forced with daily wind stress data exhibit a coastal band of high ageostrophic EKE ( $> 50 \text{ cm}^2 \text{ s}^{-2}$ ) from  $35$  to  $45^{\circ}\text{S}$  accounting for about 25% of the total surface EKE. A coastal band of high ageostrophic EKE is also found in the CL, but spatially smaller and with weaker values ( $\sim 15 \text{ cm}^2 \text{ s}^{-2}$ ) than in PS and FS. In general, ageostrophic EKE in the CL represent less than 5% of the total EKE. A similar spatial pattern and values were found in a climatological simulation for the California Current System, where a coastal strip of intensified ageostrophic EKE would be consequence of nonlinear advection of momentum in the upwelling dynamics [*Marchesiello et al.*, 2003].

South of the jet separation (i.e. south of Punta Lavapie), the offshore region exhibits the weakest geostrophic EKE due the lack of a major current inducing baroclinic instability. In fact, the values of geostrophic EKE in this region are less than  $50 \text{ cm}^2 \text{ s}^{-2}$  [Hormazabal et al., 2004]. Thus, as consequence of the synoptic variability in the wind in this region, the ageostrophic EKE becomes particularly important by contributing to the total EKE, as much as 30-50% in the PS and 40-60% in the FS simulations. In fact, the ageostrophic EKE produced by the Ekman currents is maximum south of Punta Lavapie (Figure 4.3b). Therefore, variable winds enhance the level of eddy kinetic energy in the coastal zone and principally in the offshore region off south-central Chile (south of  $\sim 37^\circ\text{S}$ ) over a background EKE which is independent of the wind stress temporal resolution.

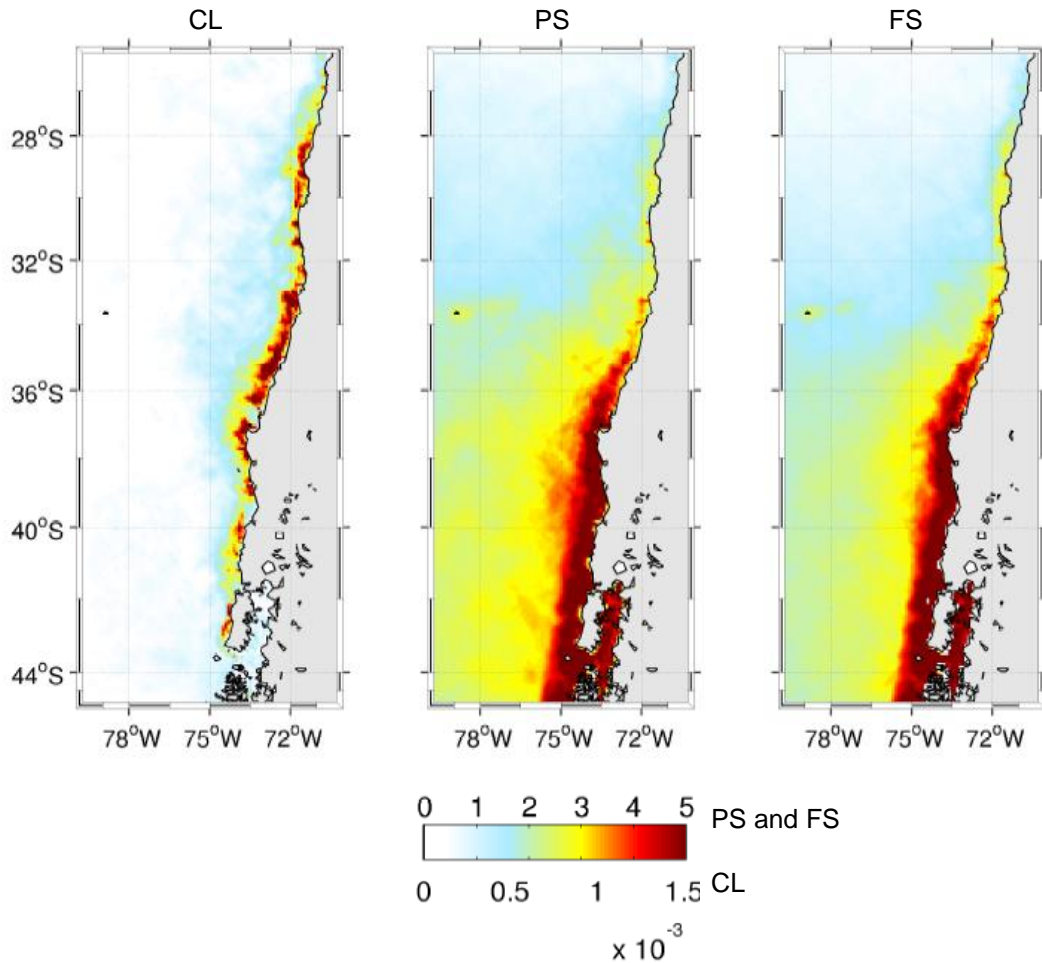


**Figure 4.5.** Summer mean of the ageostrophic surface eddy kinetic energy (EKE,  $\text{m}^2 \text{ s}^{-2}$ ) obtained from the three different simulations.

#### 4.3.3. Lagrangian properties of the surface flow

We have shown that forcing ROMS with synoptic-scale variable winds and heat fluxes makes little difference in the resulting mean currents and geostrophic EKE compared with a smooth (climatological) forcing, but it does increase the ageostrophic EKE along the coast and, particularly, in the offshore region south of Punta Lavapie (Figure 4.3b). To further quantify this effect, here we study the properties of the surface flow by tracking particles released at the

surface ocean using a Lagrangian drifter-tracking code, developed by X. Capet<sup>1</sup>. The offline version of the code advects numerical floats from stored ROMS outputs of the velocity field. For more details of the algorithm the reader is referred to *Carr et al.*, [2008]. For this analysis we used the ROMS outputs from December of each simulated year (8 months per simulation). Drifters were released simultaneously at the surface within a strip of ~25 km located about 200 km from the shore, separated by 5 km in the cross-shore direction and 10 km in the along-shore direction (Figure 4.6). This analysis was performed in a region with high EKE north of Punta Lavapie (centered at 35°S) and in a region with low EKE south of Punta Lavapie (centered at 43°S).

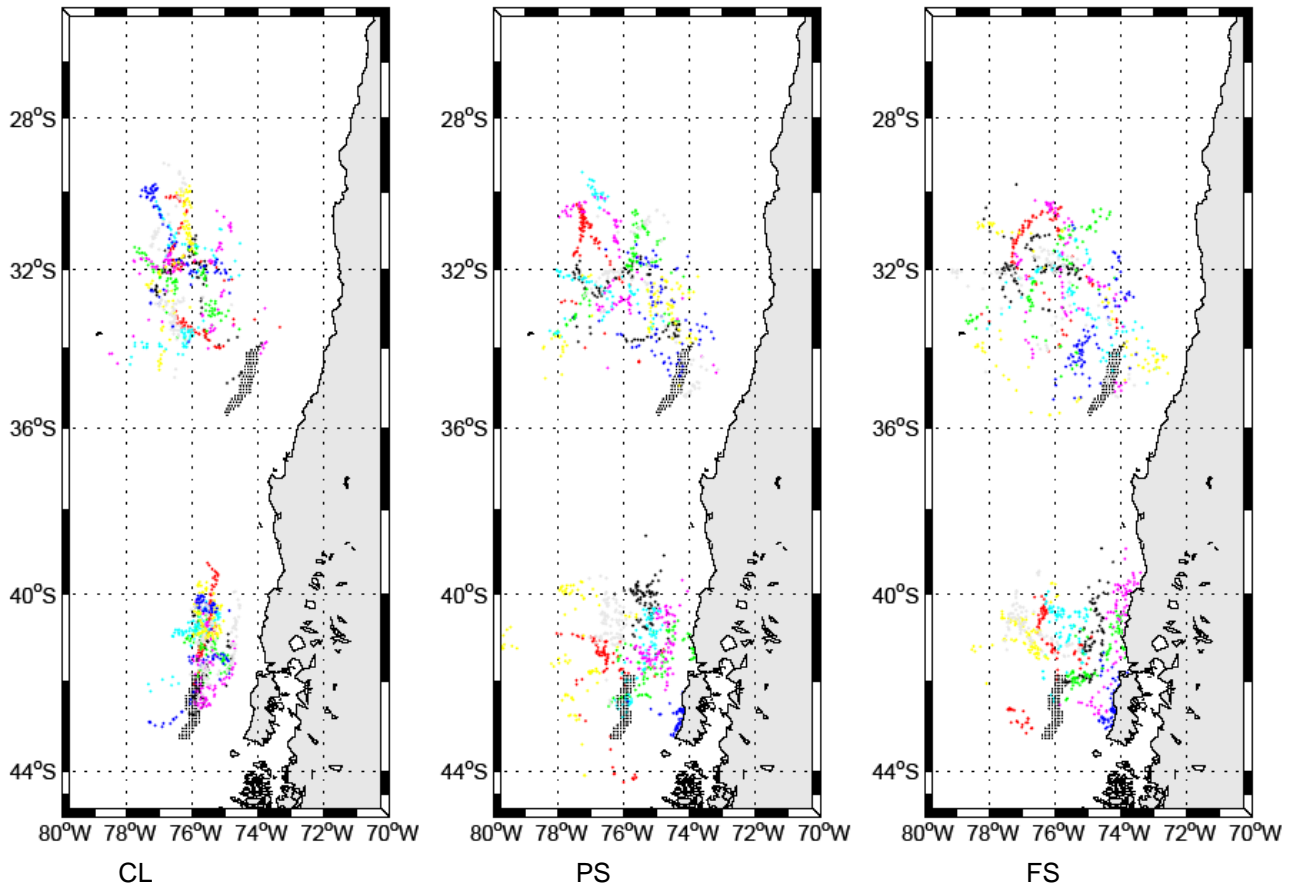


**Figure 4.6.** Dispersion of surface drifters in two different locations off south-central Chile. The black dots indicate the initial position of the drifters and dots with different colors represent the position reached by each drifter one month later (December) in different years of simulation.

In a Lagrangian frame, the velocity vector of each drifter ( $\mathbf{U}(t)$ ) can be written as  $\mathbf{U} + \mathbf{u}'(t)$ , where  $\mathbf{U}$  is the mean flow, representative of the large spatial scale and calculated by averaging the velocity component over each drifter trajectory, and  $\mathbf{u}'$  is the time varying perturbation [e.g., *Kundu and Cohen*, 2000]. For the zonal ( $u'$ ) and meridional ( $v'$ ) components of the eddy velocity we calculated the integral time scale  $\mathbf{T}=(T_u, T_v)$ , the integral length scale  $\mathbf{L}=(L_u, L_v)$  and the horizontal diffusivity  $\mathbf{K}=(K_u, K_v)$  as in *Chaigneau and Pizarro* [2005]. These statistics were computed for each drifter (80 drifters in each simulation) and are presented in Table 4.

<sup>1</sup> Roms Offline Floats (Roff) available at [http://www.atmos.ucla.edu/~capet/Myresearch/my\\_research\\_floats.html](http://www.atmos.ucla.edu/~capet/Myresearch/my_research_floats.html)



On the basis of a  $t$ -test with a significance level of 5%, all mean values become significantly different between the north and south parts of the domain (i.e. north and south of Punta Lavapie). Most importantly, while south of Punta Lavapie all mean values are significantly different between CL and PS simulations, it is not always the case north of Punta Lavapie. In addition, in the south part, diffusivities are significantly different between PS and FS (at 95% confidence level). In terms of the diffusivity magnitude ( $|\bar{K}|$ ) we found similar differences between absolute values of  $\bar{K}$  between CL and PS in both regions ( $\sim 0.5 \cdot 10^7 \text{ cm}^2 \text{ s}^{-1}$ ), but their relative importance to the total diffusivity differ considerably. In fact, variable winds increase diffusivity by only 14% in the north part, contrasting with 71% in the south part of the domain. On the other hand, the inclusion of synoptic variability in the heat fluxes only accounts for an increase of 3% in the magnitude of the diffusivity in both regions.

**Table 4.** Lagrangian time ( $T_u, T_v$ ) and length ( $L_u, L_v$ ) scales, velocity variances ( $\overline{u'^2}, \overline{v'^2}$ ) and diffusivities ( $K_u, K_v$ ) for the zonal and meridional components of the surface flow in three different simulations and for two different location for the numerical drifter release (see more details in the text).

Float release	$T_u$ , days	$T_v$ , days	$L_u$ , km	$L_v$ , km	$\overline{u'^2}$ , $\text{cm}^2 \text{ s}^{-2}$	$\overline{v'^2}$ , $\text{cm}^2 \text{ s}^{-2}$	$K_u, 10^7$ $\text{cm}^2 \text{ s}^{-1}$	$K_v, 10^7$ $\text{cm}^2 \text{ s}^{-1}$	
CL	35°S	3.01±0.07	3.86±0.06	24.8±1.2	20.6±0.7	95	77	2.75±0.22	1.88±0.98
	43°S	3.39±0.06	3.68±0.08	10.9±0.4	12.5±0.6	15	17	0.46±0.02	0.59±0.05
PS	35°S	3.04±0.06	2.99±0.06	27.3±1.1	21.9±0.9	112	75	2.71±0.17	2.22±0.14
	43°S	2.20±0.05	2.26±0.05	14.0±0.4	11.3±0.4	54	37	1.07±0.05	0.73±0.04
FS	35°S	2.71±0.06	3.06±0.08	25.0±1.0	24.7±1.1	120	89	2.95±0.18	2.52±0.19
	43°S	2.16±0.04	2.25±0.06	13.0±0.4	12.3±0.6	50	44	0.95±0.04	0.94±0.08

Tracking actual drifters in the region comprised between 24°-34°S and 70°-82°W, *Chaigneau and Pizarro* [2005] obtained annual mean diffusivities of  $K_u=2.2\pm 0.5 (\cdot 10^7) \text{ cm}^2 \text{ s}^{-1}$  and  $K_v=1.8\pm 0.4 (\cdot 10^7) \text{ cm}^2 \text{ s}^{-1}$ . These values are lower than  $K$ -values obtained in our simulations which include synoptic variability of wind stress and heat fluxes (i.e. FS run), but it is important to note that we calculate diffusivities only for summer farther south, where synoptic-scale variability in the winds is higher.

#### 4.3.4. Sea surface temperature

The long-term mean of the summer SST observed from the Advanced Very High Resolution Radiometer (AVHRR, Pathfinder V5, years 1985-2001) and those simulated (8-years) in the three different runs are presented in Figure 4.7. Our three simulations are able to reproduce a realistic pattern of the summer mean SST field, with warmer waters offshore and colder waters at the coastal region, superimposed on a general NW-SE decrease in SST. The simulated summer upwelling front (i.e., the offshore limit of the coastal highest SST gradient) is about 75 km from the coast north of Punta Lavapie and  $\sim 100$  km from the coast south of Punta Lavapie. These values are in agreement with the location of the front estimated using satellite observations [Letelier *et al.*, 2009].

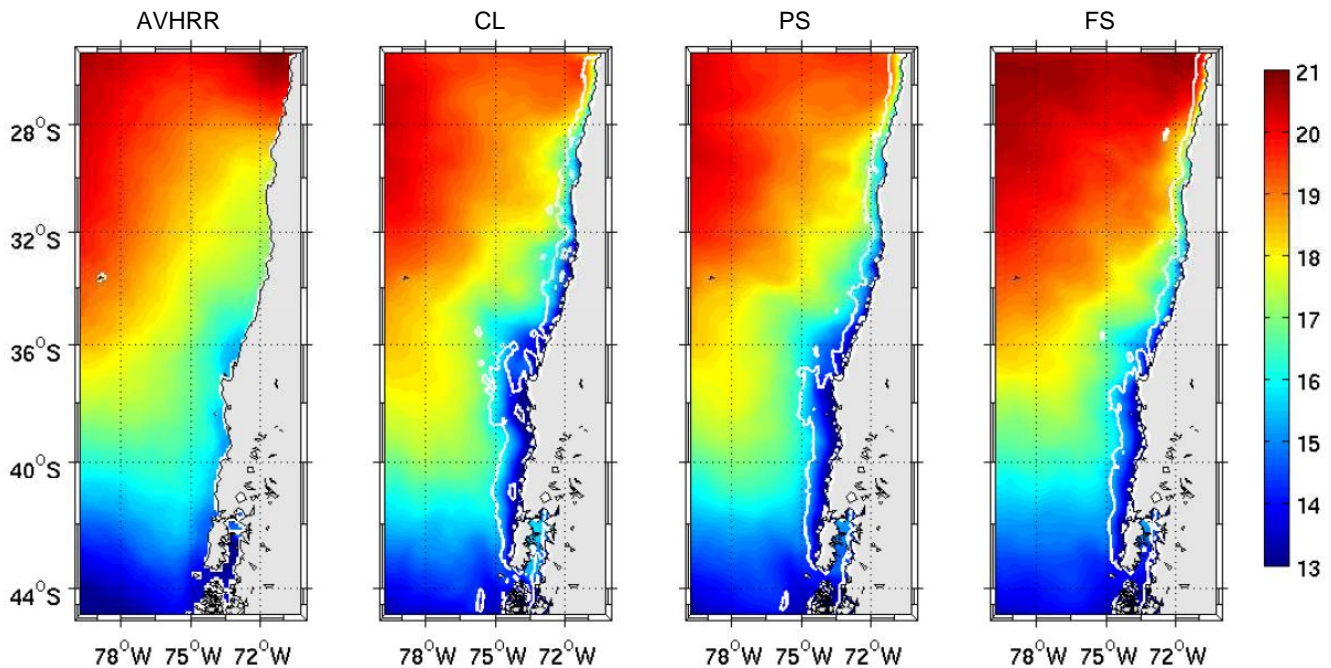


**Figure 4.7.** Summer mean of the sea surface temperature ( $^{\circ}\text{C}$ ) from satellite observations (AVHRR, Pathfinder Version 5.0 from 1985-2001) and the three different simulations. White lines in model SST field indicate the location of the mean coastal upwelling front.

Close to the coast of south-central Chile the CL and PS SST summer means are  $2\text{-}3^{\circ}\text{C}$  colder than satellite observations. However, these differences reduce to  $\sim 1^{\circ}\text{C}$  in the FS, a situation that can not be directly attributed to heat fluxes variability, since the input atmospheric variables are not the same for COADS (used in CL and PS) and NCEP (used in FS). A colder bias along the coast has also been reported in climatological simulations of the Benguela upwelling system [Penven *et al.*, 2001; Veitch *et al.*, 2010] and the Perú upwelling system [Penven *et al.*, 2005]. This bias has been attributed by these authors to the low spatial resolution of the wind forcing. In our case, the wind stress over the first  $\sim 50$  km off the coast was simply extrapolated from the nearest QuikSCAT ocean grid point ( $0.5^{\circ}$  grid spacing), typically resulting in an overestimation of the wind speed, and hence Ekman transport, in the near shore coastal strip [Capet *et al.*, 2004]. Assumption of an alternative drop-off of the near coastal winds is difficult to justify in our case because of the lack of observations in the coastal strip [Garreaud *et al.*, 2010].

Accordingly, simulated coastal SSTs are also 1-2°C colder than *in-situ* measurements during summer, while simulated offshore SSTs are very similar to those measured *in-situ* at Robinson Crusoe Island, as summarized in Table 5. In spite of the cold bias at the coast, the model SST (PS and FS runs) follows quite well the observed SST anomalies, illustrated in Figure 4.8 by daily time series at selected stations. Multi-year correlation coefficients are around 0.4-0.5 (Table 5) but we found values as high as 0.75 in individual years. The relatively high correlations between PS and *in-situ* observations at the coast, in spite of the lack of realistic (daily) air-sea fluxes in this simulation, emphasize the prominent role of wind-driven upwelling cycles in coastal SST variability. In fact, the PS simulation exhibits significantly higher summer standard deviation of the coastal SST ( $\sigma$ SST) compared with the CL one (Figure 4.9). The major differences in SST variability are found in a coastal strip off south-central Chile, coincident with the region of maximum wind variability [Renault *et al.*, 2009], where  $\sigma$ SST in PS is about two times larger than its climatological counterpart. The cross-shore scale of the  $\sigma$ SST maximum is about 20-30 km, corresponding to the region of strong coupling between the wind stress and SST via upwelling dynamics [e.g., Perlin *et al.*, 2007].

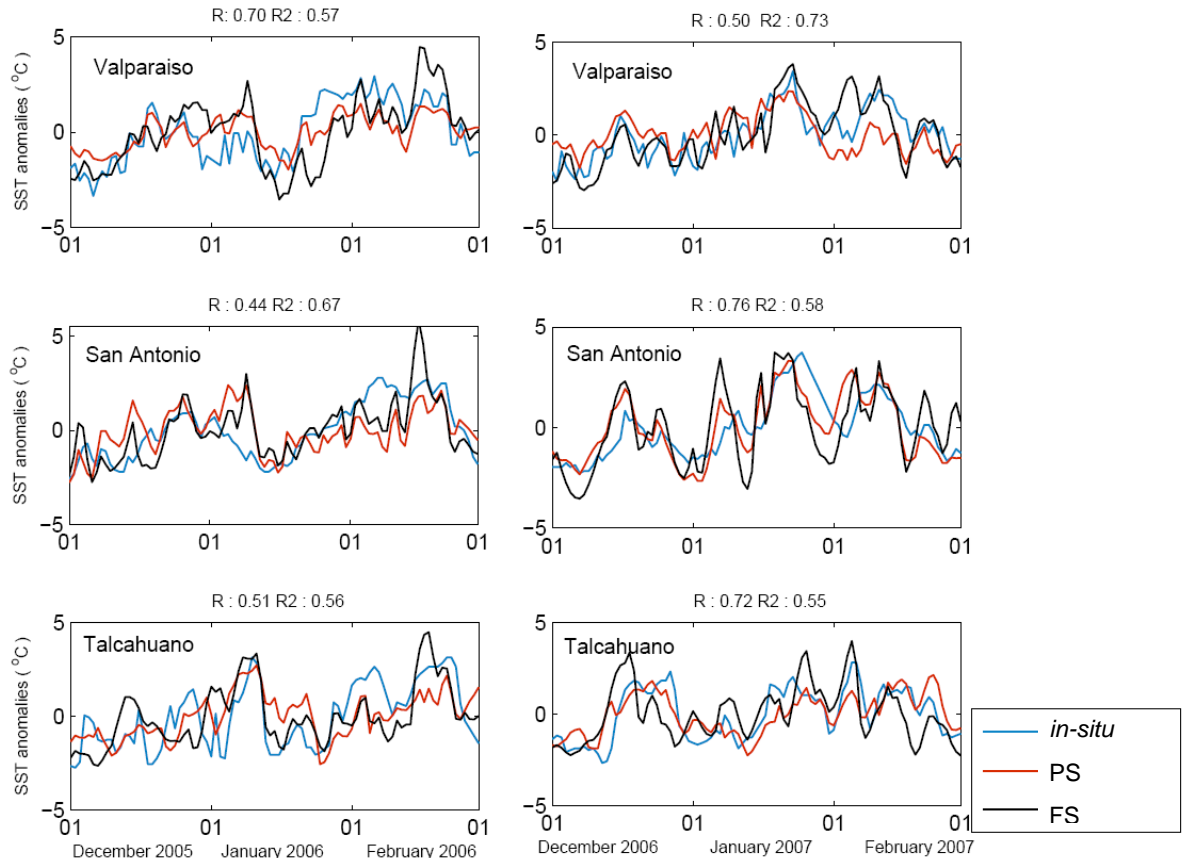


**Figure 4.8.** Daily time series of the simulated SST in the PS (red), FS (black) and *in-situ* observations (blue) at different locations during summer of 2006 and 2007. The correlation coefficient R is obtained from the time series of PS and observations, and the correlation coefficient R2 is obtained from the time series of FS and observations.

On the other hand, the FS simulation is similar to the PS one along the coast but exhibits higher variability of the SST in the offshore region, suggesting that SST day-to-day variability over the open ocean is more controlled by the corresponding changes in air-sea heat fluxes. The FS values of  $\sigma$ SST are close to those from the satellite TMI observations (Figure 4.9) and agree

well with the *in-situ* measurements at Robinson Crusoe Island, while it is overestimated in coastal regions (Table 5).

**Table 5.** Annual and summer (DJF) mean and standard deviation of *in-situ* and simulated SST at different locations along the coast and offshore. The correlation coefficient between simulated (PS and FS runs) and observed daily SST is shown for each station considering the period 2000-2007.

Location	Data	Annual mean (°C)	Annual std (°C)	Summer mean (°C)	Summer std (°C)	Annual R	Summer R
Valparaíso 33.03°S 71.63°W	CL	13.3	1.2	14.5	0.9		
	PS	13.4	1.4	15.0	1.1	0.77	0.50±0.2
	FS	13.9	1.9	16.0	1.6	0.80	0.48±0.2
	<i>in-situ</i>	13.8	1.4	15.2	1.3		
San Antonio 33.58°S 71.53°W	CL	12.6	0.8	12.8	0.7		
	PS	12.7	1.2	13.2	1.4	0.55	0.45±0.3
	FS	13.0	1.5	14.0	1.9	0.67	0.54±0.2
	<i>in-situ</i>	13.6	1.5	15.2	1.3		
Talcahuano 36.70°S 73.10°W	CL	12.4	0.7	13.0	0.7		
	PS	12.3	1.1	12.9	1.3	0.48	0.43±0.2
	FS	12.5	1.4	13.4	1.7	0.61	0.43±0.2
	<i>in-situ</i>	12.9	1.2	13.4	1.6		
Corral 39.87°S 73.42°W	CL	12.0	0.8	12.7	0.5		
	PS	12.0	1.3	12.9	1.6	0.58	0.42±0.2
	FS	12.0	1.5	13.3	1.6	0.72	0.49±0.2
	<i>in-situ</i>	12.7	2.0	14.6	1.3		
Robinson Crusoe 33.6°S 78.8°W	CL	16.7	2.0	18.8	0.9		
	PS	16.5	2.1	18.7	0.9	0.95	0.56±0.2
	FS	16.9	2.3	19.3	1.2	0.95	0.67±0.2
	<i>in-situ</i>	16.6	2.1	18.6	1.2		
	TMI	17.4	2.1	19.2	1.3		

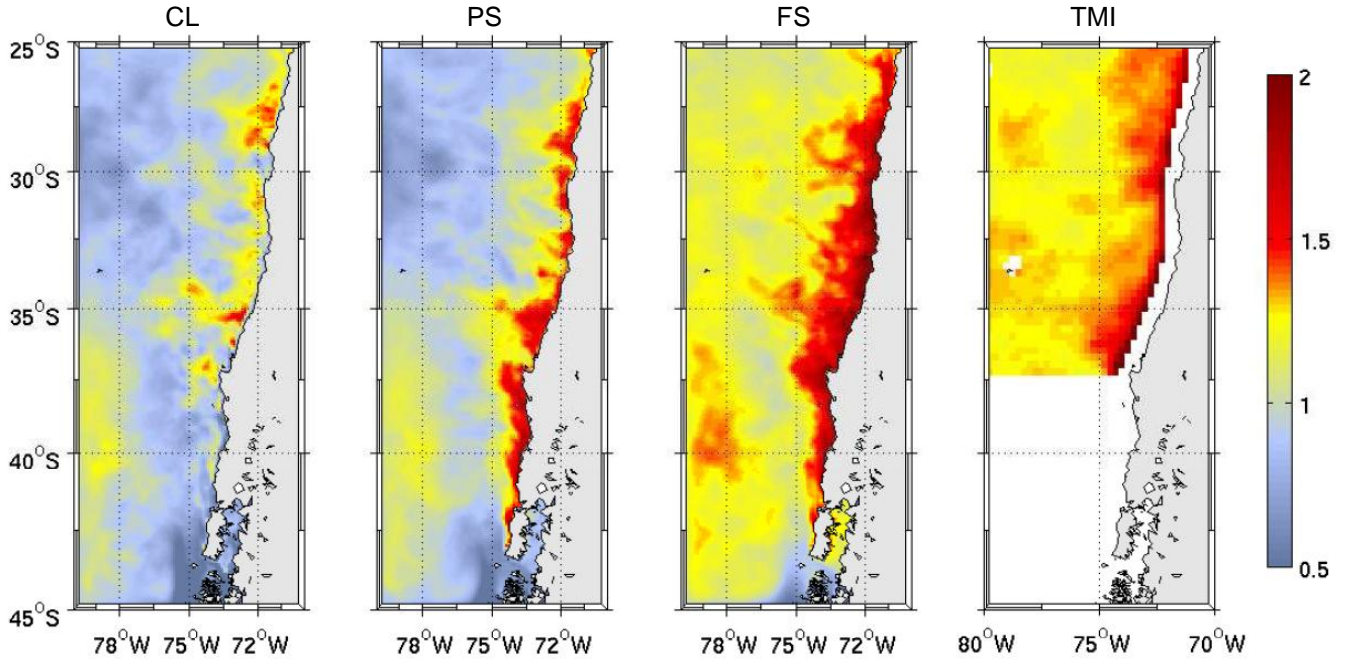


**Figure 4.9.** Summer standard deviation of the daily sea surface temperature ( $^{\circ}\text{C}$ ) from the three different simulations and from the satellite TMI data.

#### 4.4. Discussion

It is interesting to note the little rectification of the high-frequency variable wind stress and heat fluxes on the mean near-surface circulation and mean SSTs showed in our results, in contrast with the much higher level of coastal SST variability and ageostrophic EKE in the simulations which consider high-frequency variable wind stress. This suggests a rather linear response of the coastal surface ocean to cycles of southerly wind strengthening (upwelling favorable) and weakening (downwelling favorable in the case of northerly winds). Assuming approximately linear relationships, the spatial response of the surface ocean to the wind variability can be described by regressing the SST and surface current fields ( $u_{sfc}$ ,  $v_{sfc}$ ) upon the meridional wind ( $vwnd$ ). The local correlation (point to point) between SST and meridional wind is larger than  $-0.5$  (at one day lag) in a coastal strip about 20-30 km wide under the area of maximum wind anomalies, and rapidly decays offshore (Figure 4.10). This coastally confined response of SST to variable winds is consistent with the region of strong coupling between the synoptic wind and SST via upwelling dynamics in an air-sea coupled model [Perlin *et al.*, 2007] and with the cross-shore scale of maximum variability observed by Castelao and Barth [2005] in a field study performed off the Oregon coast during the upwelling season. On the other hand, the surface currents respond rapidly to the changing winds. The response to atmospheric jet events is a surface flow with offshore and equatorward components (vectors in Figure 4.10). The correlation between  $vwnd$  and  $v_{sfc}$  exhibits values as high as 0.6 (at zero lag) in a very coastally confined band (10-20 km from the shore) and implies acceleration (deceleration) of the Chilean coastal current (CCC) during atmospheric jet events (relaxation), consistent with Aiken *et al.*, [2008]. The correlation between  $vwnd$  and  $u_{sfc}$  shows maximum negative correlations values of about  $-0.6$  (at zero lag). In contrast with the coastally confined meridional flow and SST response, the highest ( $vwnd$ ,  $u_{sfc}$ ) correlations under the strong southerlies extend well offshore.

These patterns and values of correlation agree well with an observational study performed off the Oregon coast [Kosro, 2005]. In this research the lag of the maximum correlations between wind and surface currents was calculated in 2-12 hours, which can not be resolved by our model because of its daily time resolution.

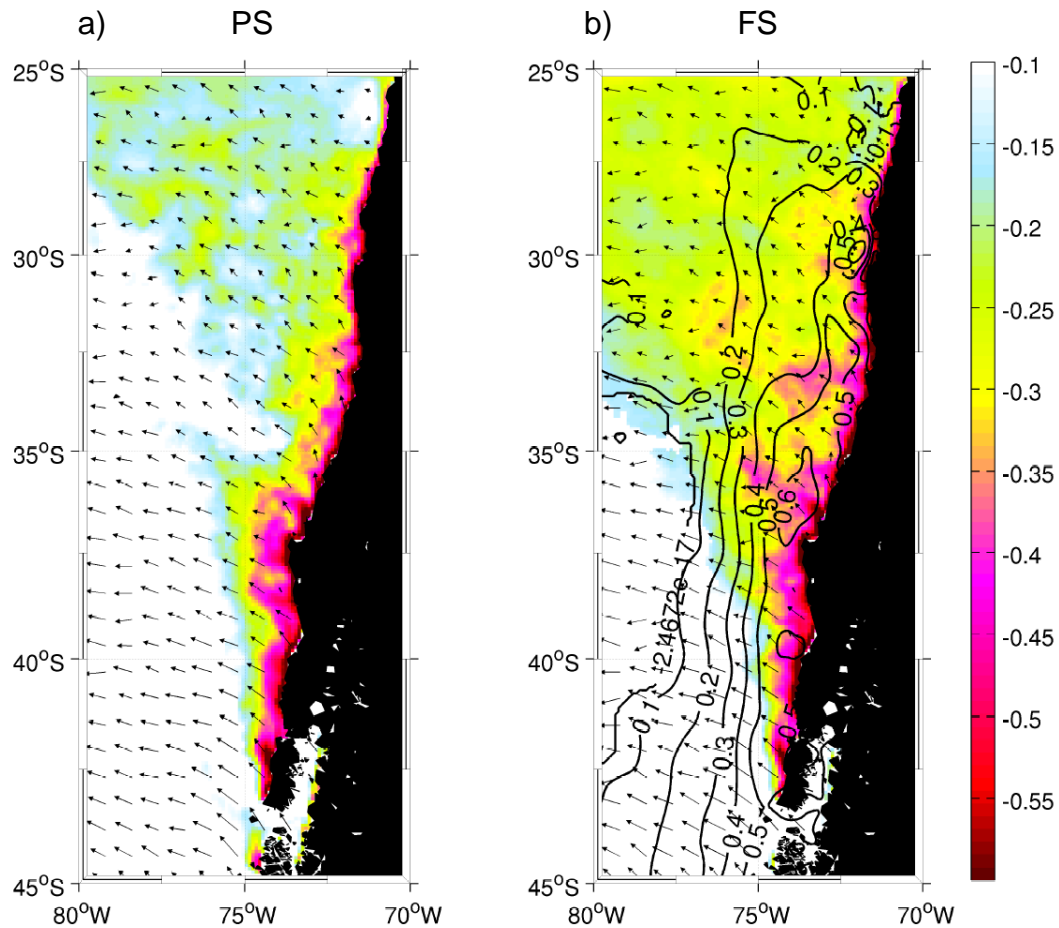


**Figure 4.10.** Local correlation map (point to point) between meridional wind and SST (colors), meridional wind and the zonal and meridional component of surface currents (vectors). a) PS and b) FS includes the correlation between meridional wind and short wave radiation (contours).

In a relatively recent modeling study, *Veneziani et al.*, [2009] compare climatological versus realistic forcings in the coastal ocean off central California. They established that the surface forcing plays a more important role than lateral forcing in the California Current System simulations. In particular, the spatial resolution of the surface forcing is largely responsible for the differences in the structure and seasonal cycle of the mean upper ocean circulation between the climatological run (forced by COADS data with spatial resolution of 1°) and the realistic run (forced by COAMPS data with spatial resolution of 3-9 km). These results, which show very similar mean surface current fields, are consistent with ours in which we only change the time resolution of the wind stresses but keep their spatial resolution. In addition, the results of *Veneziani et al.*, [2009] encourage us to use the same climatological data (WOA 2009) as lateral boundary conditions in our three runs without missing significant variability over the surface ocean.

Modeling studies in different eastern boundary current systems: California Current System [Marchesiello *et al.*, 2003], Benguela Current System [Penven *et al.*, 2001] and Perú Current System [Penven *et al.*, 2005] have provided evidence that most of the surface ocean variability is explained by intrinsic variability of the ocean arising from instabilities in the currents regardless of the presence (or absence) of high-frequency variability in the wind forcing. Both currents and fronts experience baroclinic instability [e.g. Barth, 1994; Haidvogel *et al.*, 1991]. Analysis of the energy conversion in a numerical study made by Leth and Shaffer [2001] showed that baroclinic instability is indeed a major mechanism for the generation of meanders and eddies (quasi-geostrophically balanced) off central Chile. Thus, the agreement in geostrophic EKE between our three simulations would be the result of intrinsic variability from the surface currents, especially CPC and CCC. The eddy generation at the CPC via baroclinic instability [Leth and Middleton, 2004] and the nearshore eddy generation at the CCC propagating westward [Hormazabal *et al.*, 2004], may constitute major sources for the geostrophic EKE offshore.

In spite of the geostrophic EKE being a major component of the total EKE north of Punta Lavapié ( $\sim 37^\circ\text{S}$ ), the ageostrophic EKE plays an important role farther south, where the geostrophic EKE is considerably weaker due the lack of major currents. In fact, we showed that south of  $\sim 37^\circ\text{S}$  diffusivities are significantly higher when synoptic wind stress variability in surface forcing is included. These results highlight the relevance of using variable (synoptic) winds to force the ocean models if one aims at describing the turbulent component of the upper-ocean circulation, as it is in biological modeling when dispersal of chemicals and larvae are key issues. This indicates that the temporal variability of the atmospheric forcing contributes to the overall energy structure, particularly in absence of major currents which produce geostrophic EKE through baroclinic instability.

The role of heat fluxes on SST variability seems to be more prominent in the offshore region than in the coastal zone. The correlation map between  $v_{wnd}$  and SST for the FS run shows larger coefficients offshore but do not alter significantly these values close to the coast in comparison with PS (Figure 4.10). Consequently the variability of SST in the first 30 km from the shore, in the region of maximum wind stress variability, is not significantly different between the PS and the FS (Figure 4.11). In contrast,  $\sigma\text{SST}$  offshore is significantly different between these simulations suggesting that is necessary to include synoptic variable heat fluxes to account for a realistic  $\sigma\text{SST}$ .

The weak increase of  $\sigma\text{SST}$  along the coast when the surface heat fluxes variability is considered relative to the case of climatological fluxes is rather puzzling. In fact, the agreement between the observed and PS-simulated coastal SST is as good as the comparison between observation and the FS results. Because the horizontal resolution of our simulations is not high enough to fully describe coastal upwelling events, we have refrained from performing a coastal energy budget, as recently performed by Renault *et al.* [2012]. Nonetheless, we offer a qualitative explanation of this apparent paradox. While the sensible and latent heat fluxes ( $Q_{sen}$  and  $Q_{lat}$ ) increase during a jet event, their overall effect is small compared with other terms [Renault *et al.*, 2012]. Thus, adding the high-frequency variability of  $Q_{sen}+Q_{lat}$  adds little -if correctly simulated- to the coastal SST variability in our simulation. On the other hand, in the real ocean, the day-to-day variability of shortwave radiation (SW) acts as a damping term in SST variability. Garreaud and Muñoz [2005] showed that meridional wind is significant and negatively correlated with coastal cloud amount, so that coastal jet events often features clear skies which

tend to heat the ocean (by the contrary, downwelling favorable winds are associated with overcast conditions). Such observational relationship between coastal  $w_{wnd}$  and SW is replicated in present in the boundary conditions used to force our model, as shown by the local correlation between these two variables (contours in Fig. 4.10b), thus acting to decrease  $\sigma_{SST}$  in FS.

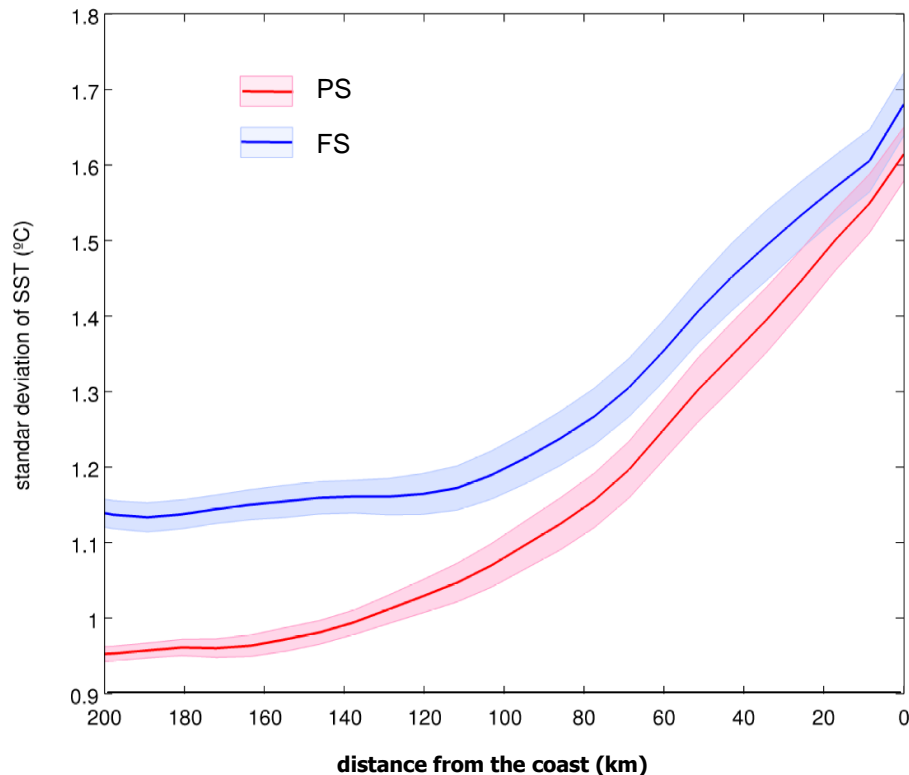


**Figure 4.11.** Meridionally averaged ( $36^{\circ}\text{S} - 41^{\circ}\text{S}$ ) standard deviation of the SST in the PS (red line) and FS (blue line). The shaded areas indicate the confidence interval using a  $t$ -test at the 95% level of confidence.

## 4.5. Conclusions

In this Chapter we have investigated the effects of the synoptic variability of the surface wind stresses and heat fluxes on the ocean off south-central Chile ( $35^{\circ}\text{S} - 45^{\circ}\text{S}$ ) using the regional ocean model (ROMS). We performed three continuous 8-year long simulations (plus two years of spin up) forced by the long-term monthly mean winds (climatological run, CL), QuikSCAT (2000-2007) daily winds (synoptic wind stress run, PS) and daily winds (QuikSCAT) plus other daily atmospheric variables (2000-2007), in order to calculate surface heat fluxes through bulk formulas (synoptic wind stress and heat fluxes run, FS). The simulations are identical otherwise, including lateral boundary conditions from the World Ocean Atlas. This study focuses in the austral summer (December to February) when south-central Chile experience southerly, upwelling favorable mean wind but with substantial day-to-day variability including strong southerly jet events.

The simulated summer mean fields of upper-ocean currents and SST are very similar between the three runs and they reproduce the major observed features of the circulation in the southeast Pacific, such as the Chile-Perú Current, the Perú-Chile Countercurrent and



Undercurrent, the Coastal Chilean Current, and the coastal band of upwelled cold waters. Furthermore, the surface geostrophic EKE is similar between simulations, consistent with the idea that it is intrinsically generated by instability of the major currents. The model geostrophic EKE also agrees well with the spatial pattern observed in satellite-data, but with higher values. In contrast, the ageostrophic EKE is significantly higher in simulations which include wind stress synoptic variability (PS and FS) compared with the CL run, particularly south of Punta Lavapie (~37°S) and inside a coastal band about 50 km wide under the region of strong winds and collocated with the CCC. This has a direct impact in the simulated diffusivities, which are 75% (25%) larger in the simulation including variable wind stresses than in the *climatological* run south (north) of Punta Lavapie, highlighting the relevance of using variable winds to force the ocean models if one aims at describing the turbulent component of the upper-ocean circulation, in particular in regions where the lack of major currents prevents the production of geostrophic EKE through baroclinic instability.

Differences between simulations using climatological and daily variable winds are also found in SST variability within the first 20-30 km offshore. The standard deviation of the daily SST in PS is about twice larger than its climatological counterpart.  $\sigma$ SST is similar between in PS and FS, and agree well with *in-situ* observations indicative of the prominent role of wind-driven upwelling cycles in coastal SST synoptic variability. In contrast, in the offshore region it is necessary to include daily heat fluxes variability to account for the SST variability observed by satellite measurements. Table 6 summarizes these major impacts of the wind stress and heat fluxes variability on the surface ocean north and south of Punta Lavapie (~37°S). The similarities in the spatial pattern of the mean SST, currents and geostrophic EKE between the three simulations in contrast with the much higher level of coastal SST variability and ageostrophic EKE in the runs that include synoptic variability of wind stresses and heat fluxes is indicative of a rather linear response of the surface ocean to cycles of southerly wind strengthening and relaxation.

**Table 6.** Summary of the impacts of the of wind-stress and heat fluxes variability on surface ocean.

		Impact of wind stress variability			Impact of heat fluxes variability		
		$\frac{ageosEKE}{totalEKE}$	$\vec{K}$	$\sigma$ SST	$\frac{ageosEKE}{totalEKE}$	$\vec{K}$	$\sigma$ SST
<b>North Punta Lavapié</b>	Coast	low	-	high	none	-	low*
	Offshore	low	low	none	none	low	high*
<b>South Punta Lavapié</b>	Coast	low	-	high	none	-	none
	Offshore	high	high	none	none	low	high

Mean SST, currents and geostrophic EKE are not included in this table because they are very similar between the three simulations

\*relative with respect to absolute  $\sigma$ SST.

# Chapter 5

## General conclusions and future work

In this thesis, the response of the surface ocean circulation to seasonal and synoptic scales of the atmospheric forcing was described and explanations of the mechanism involved were developed. Satellite derived wind stress, sea level height and surface temperature, along with *in-situ* measurements of currents were used to describe the surface circulation. In addition, a regional ocean model was utilized to examine how the surface ocean responds to different winds forcing.

The satellite derived and simulated surface ocean currents showed a seasonal cycle and a well defined equatorward flow with a jet-like structure. This jet develops during spring and summer consistent with the seasonal cycle of the wind stress. Thus, at the seasonal scale one of the main conclusions is that not only changes in the strength of the wind stress forcing must be considered to account for changes in the near-surface circulation. The spatial pattern of the wind stress field plays a fundamental role in the dynamics of ocean currents and formations of ocean jets, which is neither related with the Sverdrup balance nor with the offshore movement of a coastal jet associated with the upwelling dynamics. This suggests that the wind stress curl is much more important than previously thought, as emphasized in Chapter 3. In addition, a headland (Punta Lavapie) seems to be the key for the wind stress pattern present off central Chile during summer, showing that the CTZ jet is the result of an atmosphere-ocean-land interaction process.

On the other hand, at the synoptic scale the main conclusion is that there is little rectification of the high frequency wind stress and heat fluxes on the near-surface mean circulation and that there is a quasi-linear response of the sea surface temperature to wind changes near the coast. In contrast, higher variability of sea surface temperature (particularly close to the coast) and higher eddy kinetic energy (particularly south of Punta Lavapie) is caused by the synoptic variability of wind stress. Higher eddy kinetic energy impacts on the diffusivity values, stressing the importance in using daily wind stress for describing the turbulent component of the upper-ocean circulation in regional models.

As future work the interannual variability of the CTZ jet as well as its long-term change is under consideration in order to document more completely the dynamics of this flow. The large interannual variability related to the El Niño-Southern Oscillation (ENSO) cycle may directly modulate the CTZ jet due to changes in the wind stress related, in turn, to disturbances in the South Pacific subtropical anticyclone, or indirectly due to the extra-tropical interannual oceanic Rossby wave that is forced by the ENSO in the eastern South Pacific [Vega *et al*, 2003]. On the other hand, regional climate simulations for futures scenarios of increased warming have resulted in a southerly wind increase during spring and summer off western subtropical South America, expanding the upwelling-favorable regime [Garreaud and Falvey, 2008]. If the wind stress curl pattern is changed, the equatorward CTZ jet would presumably be influenced.

Since we have showed in this thesis that the synoptic wind variability introduces higher variability in a thin strip at the coastal ocean, an increase in horizontal resolution of simulations is an important task to fully describe coastal upwelling events and to perform a coastal energy

budget. It has been shown that wind drop-off near the coast may play a fundamental role in upwelling dynamics [Capet *et al.*, 2004], and, in particular, on the heat balance off central Chile [Renault *et al.*, 2012]. Nevertheless, an improved analysis of the coastal wind satellite data evidences that near-shore wind jets, which exhibits higher diurnal variability, precludes the drop-off during the afternoon, particularly off points and capes. This has been previously simulated by high resolution atmospheric model performed off central Chile [Rahn *et al.*, 2011], but its impact on the surface ocean circulation is still being investigated.

Finally, the regional climate simulations for futures scenarios of increased warming have indicated that the atmospheric coastal jets at subtropical latitudes will become more frequent. Following the results obtained in this thesis this should not change neither the general circulation nor the surface temperature, but it should increase the level of eddy kinetic energy available at the surface ocean. This would be interesting to test, because it could increase the horizontal diffusivity, which would affect the heat and nutrients transport between the coastal and offshore regions.

## References

- Aiken C., M. Castillo, and S. Navarrete (2008), A simulation of the Chilean Coastal Current and associated topographic upwelling near Valparaíso, Chile, *Cont. Shelf Res.*, 28, 2371-2381.
- Anderson, D. L. T., and A. E. Gill (1975), Spin-up of a stratified ocean, with application to upwelling. *Deep-Sea Res.* 22, 583-596.
- Antonov, J., R. Locarnini, T. Boyer, A. Mishonov, and H. Garcia (2006), World Ocean Atlas 2005, vol. 2, Salinity, NOAA Atlas NESDIS, vol. 62, edited by S. Levitus, 182 pp., U.S. Gov. Print. Off., Washington, D. C.
- Bakun, A., and C.S. Nelson (1991), The seasonal cycle of wind stress curl in sub-tropical eastern boundary current region, *J. Phys. Oceanogr.*, 21, 1815-1834.
- Barth, J. (1994), Short-wavelength instabilities on coastal jets and fronts. *J. Geophys. Res.*, 99, 16095 – 16115.
- Barth J. and R. Smith (1998), Separation of a coastal upwelling jet at Cape Blanco, Oregon, USA. *S. Afr. J. Mar. Sci.*, 19, 5-14.
- Barth J., S. Pierce and R. Smith (2000), A separating coastal upwelling jet at Cape Blanco, Oregon and its connection to the California Current System. *Deep-Sea Res. II*, 47, 783-810.
- Batteen M., C. Hu, J. Bacon and C. Nelson (1995), A numerical study of the effects on wind forcing on the Chile Current System. *J. Oceanogr.*, 51, 585-614.
- Beckmann A. and D. Haidvogel (1993), Numerical simulation of flow around a tall isolated seamount. Part I: Problem formulation and model accuracy. *J. Phys. Oceanogr.* 23, 1736-1753.
- Blanco, J. L., A. Thomas, M. Carr and P. T. Strub (2001), Seasonal climatology of hydrographic conditions in the upwelling region off northern Chile. *J. Geophys. Res.*, 106, 11451 - 11467. doi :10.1029/2000JC000540.
- Brink, K. H., and T. J. Cowles (1991), The Coastal Transition Zone Program. *J. Geophys. Res.*, 96(C8), 14637-14647.
- Capet X., P. Marchesiello, and J. McWilliams (2004), Upwelling response to coastal wind profiles, *Geophys. Res. Lett.*, 31, L13311, doi: 10.1029/2004GL020123.
- Capet X., F. Colas, P. Penven, P. Marchesiello and J. McWilliams (2008), Eddies in eastern-boundary subtropical upwelling systems. In: *Eddy-Resolving Ocean Modeling*, M. Hecht & H. Hasumi, eds., AGU Monograph.
- Carr S., X. Capet, J. McWilliams, T. Pennington and F. Chavez (2008), The influence of diel vertical migration on zooplankton transport and recruitment in an upwelling region. *Fisheries Oceanogr.* 16, 1-15, doi:10.1111/j.1365-2419.2007.00447.x
- Castelao R. and J. Barth (2005), Coastal ocean response to summer upwelling favorable winds in a region of alongshore bottom topography variations. *J. Geophys. Res.*, 110, C10S04, doi:10.1029/2004JC002429.
- Castelao R. and J. Barth (2006), The relative importance of wind strength and along-shelf bathymetric variations on the separation of a coastal upwelling jet. *J. Phys. Oceanogr.*, 36, 412-425.

- Castelao R. and J. Barth (2007), The role of wind stress curl in jet separation at a cape. *J. Phys. Oceanogr.*, 37, 2652 – 2670, doi: 10.1175/2007JPO3679.1
- Chaigneau A. and O. Pizarro (2005), Mean surface circulation and mesoscale turbulent flow characteristics in the eastern South Pacific from satellite tracked drifters. *J. Geophys. Res.*, 110, C05014, doi:10.1029/2004JC002628.
- Charney J. J. (1955), The generation of ocean currents by wind. *J. Mar. Res.*, 14, 477-498.
- Chelton D. B. and M. G. Schlax (1996), Global observations of oceanic Rossby waves, *Science*, 272, 234-238.
- Chelton D. B., R. de Szoeke, M. Schlax, K. El Nagger and N. Siwertz (1998), Geophysical variability of the first baroclinic Rossby radius of deformation. *J. Phys. Oceanogr.*, 28, 433-460.
- Chelton D. B., M. Schlax, R. Samelson and R. de Szoeke (2007), Global observations of large oceanic eddies. *Geophys. Res. Lett.*, 34, doi: 10.1029/2007GL030812.
- Chelton, D. B., M. Schlax, and R. Samelson (2011), Global observations of nonlinear mesoscale eddies. *Prog. Oceanogr.*, 91, 167-216
- Csanady, G. T. (1977), The coastal jet conceptual model in the dynamics of shallow seas, in *The Sea*, Vol. 6, *Marine modelling*, Goldberg, E. D., McCave, I. N., O'Brien, J. V., and Steele, J. H., Eds., Wiley, New York, 117.
- Cushman-Roisin B. (1994), *Introduction to Geophysical Dynamics*, 320 pp., Prentice-Hall, Upper Saddle River, N. J.
- Da Silva A., C. Young, and S. Levitus (1994), Atlas of surface marine data 1994, vol. 1, Algorithms and procedures, technical report, Natl. Oceanogr. and Atmos. Admin., Silver, Spring, Md.
- Ducet N., P. Le Traon and G. Reverdin (2000), Global high-resolution mapping of ocean circulation from TOPEX/Poseidon and ERS-1 and -2, *J. Geophys. Res.*, 105, C8, doi:10.1029/2000JC900063.
- Dunn J.R., and K.R. Ridgway (2002), Mapping ocean properties in regions of complex topography, *Deep Sea Res*, 49(3), 591-604.
- Figueroa D. and C. Moffat (2000), On the influence of topography in the induction of coastal upwelling along Chilean coast. *Geophys. Res. Lett.*, 27, 23, doi:10.1029/1999GL011302
- Ekman V.W. (1905), On the influence of the earth's rotation in ocean currents, *Arch. Math. Astron. Phys.*, 2, 1-52.
- Food and Agriculture Organization (2004), El estado mundial de la pesca y la acuicultura 2004, *Rep.* 92-5-205177-5, Roma.
- Fuenzalida, H. (1971), *Climatología de Chile*. Departamento de Geofísica, Universidad de Chile, Santiago.
- Fuenzalida R., W. Schneider, J. Garcés-Vargas, and L. Barvo (2008), Satellite altimetry data reveal jet-like dynamics of the Humboldt Current. *J. Geophys. Res.*, 113, C07043, doi:10.1029/2007JC004684.
- Garreaud, R. and M. Falvey (2008), The coastal winds off western subtropical South America in future climates scenarios. *Int. J. Climatol.* 29, 543-554.

- Garreaud, R. and R. Muñoz (2005), The low level jet off the west coast of subtropical South America: structure and variability. *Mon. Wea. Rev.*, *133*, 2246-2261.
- Garreaud, R., J. A. Rutllant and H. Fuenzalida (2002), Coastal lows along the subtropical west coast of South America: Mean structure and evolution. *Mon. Wea. Rev.*, *130*, 75-88.
- Garreaud, R., J. A. Rutllant, R. Muñoz, D. Rahn, M. Ramos and D. Figueroa (2010), VOCALS-CUpEx: the Chilean Upwelling Experiment. *Atmos. Chem. and Phys. Open Discussion*. VOCALS-REx Special Issue 10, 26437-26472.
- Gill, A. (1982), Atmosphere-ocean dynamics. Academic Press. New York, 662 pp.
- Haidvogel, D.B., A. Beckman and K.S. Hedstrom (1991), Dynamical simulation of filament formation and evolution in the coastal transition zone. *J. Geophys. Res.*, *96*, 15017-15040.
- Haney, R., R. Hale, and D. Dietrich (2001), Offshore propagation of eddy kinetic energy in the California Current, *J. Geophys. Res.*, *106*(C6), 11709-11717.
- Hill, A.E., B. Hickey, F. Shillington, P.T. Strub, K.H. Brink, E. Barton, and A. Thomas (1998), Eastern boundary currents: A pan-regional review, in *The Sea*, vol. 11, *The Global Coastal Ocean: Regional Studies and Syntheses*, edited by A.R. Robinson and K.H. Brink, pp. 29-68, John Wiley, New York.
- Horel, J. D. (1984), Complex principal component analysis: theory and examples, *J. Clim. Appl. Meteorol.*, *23*, 1660– 1673.
- Hormazabal S, G. Shaffer, and O. Pizarro (2002). Tropical Pacific control of intraseasonal oscillations off Chile by way of oceanic and atmospheric pathways. *Geophys. Res. Lett.*, *29*, 6, doi:10.1029/2001GL013481.
- Hormazabal S., G. Shaffer, and O. Leth (2004), Coastal transition Zone off Chile, *J. Geophys. Res.*, *109*, C01021, doi:10.1029/2003JC001956.
- Huyer A., M. Knoll, T. Paluszkiwicz and R. Smith (1991a), The Perú Undercurrent: A study in variability, *Deep-Sea Res.*, *38*, 247-279.
- Huyer A., M. Kosro, J. Feischbein, S. Ramp, T. Stanton, L. Washburn, F. Chavez, T. Cowles, S. Pierce and R. Smith (1991b). Currents and water masses of the coastal transition zone off northern California, June to August 1988. *J. Geophys. Res.*, *96*, 14809–14831.
- Kalnay, E., M. Kanamitsu, R. Kistler, W. Collins, D. Deaven, L. Gandin, M. Iredell, S. Saha, G. White, J. Woollen, Y. Zhu, M. Chelliah, W. Ebisuzaki, W. Higgins, J. Janowiak, K.C. Mo, C. Ropelewski, J. Wang, A. Leetmaa, R. Reynolds, R. Jenne, and D. Joseph (1996), The NCEP/NCAR 40-Year Reanalysis Project, *Bull. Amer. Meteor. Soc.*, *77*, No. 3, 437-470.
- Kosro, P.M (2005), On the spatial structure of coastal circulation off Newport, Oregon, during spring and summer 2001 in a region of varying shelf width. *J. Geophys. Res.*, *110*, C10S06, doi: 10.1029/2004JC002769.
- Kundu, P. and I. Cohen (2000), *Fluid Mechanics*, 2<sup>nd</sup> ed., 730 pp., Elsevier, New York.
- Large W., J. McWilliams and S. Doney (1994), Oceanic vertical mixing: a review and a model with a nonlocal boundary layer parameterizations. *Rev. Geophys.*, *32*, 363-403.
- Letelier J., O. Pizarro and, S. Nuñez (2009), Seasonal variability of coastal upwelling and the upwelling front off central Chile, *J. Geophys. Res.*, *114*, C12009, doi: 10.1029/2008JC005171.

- Leth O. and J. Middleton (2004), A mechanism for enhanced upwelling off Central Chile: Eddy advection, *J. Geophys. Res.*, *109*, C12020, doi:10.1029/2003JC002129.
- Leth O. and G. Shaffer (2001), A numerical study of the seasonal variability in the circulation off central Chile. *J. Geophys. Res.*, *106*, 22229-22248, doi:10.1029/2000JC000627.
- Locarnini R., A. Mishonov, J. Antonov, T. Boyer and H. Garcia (2006), World Ocean Atlas 2005, vol. 1, Temperature, NOAA Atlas NESDIS, vol. 61, edited by S. Levitus, 182 pp., U.S. Gov. Print. Off., Washington, D. C.
- Marchesiello P., J. McWilliams, and A. Shchepetkin (2001), Open boundary conditions for long-term integration of regional oceanic models, *Ocean Modell.*, *3*, 1-21.
- Marchesiello P., J. McWilliams, and A. Shchepetkin (2003), Equilibrium structure and dynamics of the California Current system, *J. Phys. Oceanogr.*, *33*, 753-783.
- McCreary, J. P. and S. Y. Chao (1985), Three-dimensional shelf circulation along an eastern ocean boundary. *J. Mar. Res.*, *43*, 13-36.
- Mesias J., R. Matano and P. T. Strub. 2001. A numerical study of the upwelling circulation off central Chile. *J. Geophys. Res.*, *106*, 19611-19623, doi:10.1029/2000JC000649.
- Mesias J., R. Matano and P.T. Strub (2003), Dynamical analysis of the upwelling circulation off central Chile. *J. Geophys. Res.*, *108*, 3085, doi:10.1029/2001JC001135.
- Montecino V., T. Strub, F. Chavez, A. Thomas, J. Tarazona and T. Baumgartner (2006), Bio-Physical interactions off Western South-America, in *The Sea*, vol. 14, *The Global Coastal Ocean: Regional Studies and Syntheses*, edited by A. R. Robinson and K.H. Brink, pp 329-390, Harvard Univ. Press, Cambridge, Mass.
- Muñoz R. and R. Garreaud (2005), Dynamics of the low level jet off the west coast of subtropical South America. *Mon. Wea. Rev.*, *133*, 3661-3677.
- Penven P., C. Roy, J. Lutjeharms, A. Colin de Verdière, A. Johnson, F. Shillington, P. Fréon, and G. Brundrit (2001), A regional hydrodynamic model of the Southern Benguela, *S. Afr. J. Sci.*, *97*, 472-476.
- Penven P., V. Echevin, J. Pasapera, F. Colas, and J. Tam (2005), Average circulation, seasonal cycle and mesoscale dynamics of the Perú Current System: A modeling approach, *J. Geophys. Res.*, *110*, C10021, doi: 10.1029/2005JC002945.
- Perlin N., E. Skillingstad, R. Samelson, and P. Barbour (2007), Numerical simulation of air-sea coupling during coastal upwelling, *J. Phys. Oceanogr.*, *37*, 2081-2093, doi: 10.1175/JPO3104.1.
- Philander S. and J. Yoon (1982), Eastern boundary currents and coastal upwelling. *J. Phys. Oceanogr.*, *12*, 862 – 878.
- Pizarro O., S. Hormazábal, A. González and E. Yañez (1994), Variabilidad del viento, nivel del mar y temperatura en la costa norte de Chile, *Invest. Mar.* *22*, 85-101.
- Pizarro O. (1999), Low frequency fluctuations in the eastern boundary current off South America: Remote and local forcing. Department of Oceanography, Earth Sciences Centre, Goteborg University.
- Pizarro, O., G. Shaffer, B. Dewitte, and M. Ramos (2002), Dynamics of seasonal and interannual variability of the Peru-Chile Undercurrent. *Geophys. Res. Lett.*, *29*, 12, doi:10.1029/ 2002GL 014790.

- Pringle, J. and K. Brink (1999), High frequency internal waves on a sloping shelf. *J. Geophys. Res.*, 104: 5283-5299.
- Ramos M., O. Pizarro, L. Bravo and B. Dewitte (2006), Seasonal variability of the permanent thermocline off northern Chile. *Geophys. Res. Lett.*, 33, doi: 10.1029/2006GL025882.
- Rahn, D., R. Garreaud and J. Rutllant (2011), The low-level atmospheric circulation near Tongoy Bay / point Lengua de Vaca (Chilean coast, 30°S). *Mon. Wea. Rev.* 139, 3628-3647.
- Renault L., B. Dewitte, M. Falvey, R. Garreaud, V. Echevin, and F. Bonjean (2009), Impact of the atmospheric coastal jet off central Chile on sea surface temperature from satellite observations (2000-2007), *J. Geophys. Res.*, 114, C08006, doi: 10.1029/2008JC005083.
- Renault L., B. Dewitte, P. Marchesiello, S. Illig, V. Echevin, G. Cambon, M. Ramos, O. Astudillo, P. Minnis and K. Ayers (2012), Upwelling response to atmospheric coastal jets off central Chile: A modeling study of the October 2000 event. *J. Geophys. Res.*, 117, C02030, doi: 10.1029/2011JC007446.
- Ridway K.R., J.R. Dunn and J.L. Wilkin (2002), Ocean interpolation by four-dimensional least squares – Applications to the waters around Australia. *J. Atmos. Ocean Tech.*, 19(9), 1357-1375.
- Rutllant J. and V. Montecino (2002), Multiscale upwelling forcing cycles and biological response off north-central Chile. *Rev. Chilena Hist. Natural*, 75, 217-231.
- Saavedra N. and A. Foppiano (1992), Monthly mean pressure model for Chile. *International Journal of Climatology*, 12, 469-480.
- Saha, S., and Coauthors (2010), The NCEP Climate Forecast System Reanalysis. *Bull. Amer. Meteor. Soc.*, 91, 1015-1057.
- Shaffer G., O. Pizarro, L. Djurfeldt, S. Salinas, and J. Rutllant (1997), Circulation and low-frequency variability near the Chile coast: Remotely forced fluctuations during the 1991-1992 El Niño, *J. Phys. Oceanogr.*, 27, 217-235.
- Shaffer G., S. Hormazábal, O. Pizarro, L. Djurfeldt, and S. Salinas (1999), Seasonal and interannual variability of currents and temperature over the slope off central Chile. *J. Geophys. Res.*, 104, 29951-29961, doi: 10.1029/1999JC900253.
- Shaffer G., S. Hormazábal, O. Pizarro and M. Ramos (2004), Circulation and variability in the Chile Basin. *Deep-Sea Res. I*, 51, 1367-1386.
- Shchepetkin A., and J. McWilliams (2003), A method for computing horizontal pressure-gradient force in an ocean model with nonaligned vertical coordinate, *J. Geophys. Res.*, 108(C3), 3090, doi: 10.1029/2001JC001047.
- Shchepetkin A., and J. McWilliams (2005), The regional oceanic modeling system (ROMS): A split-explicit, free-surface, topography-following-coordinate oceanic model, *Ocean Modell.*, 9, 347-404.
- Silva, N. and S. Neshyba (1979), On the southernmost extension of the Perú-Chile Undercurrent, *Deep-Sea Res.*, 26, 1387-1393.
- Smith W., and D. Sandwell (1997), Global seafloor topography from satellite altimetry and ship depth soundings, *Science*, 277, 1957-1962.
- Sobarzo, M., L. Bravo, D. Donoso, J. Garces-Vargas, and W. Schneider (2007), Coastal upwelling and seasonal cycle that influence the water column over the continental shelf off central Chile. *Prog. Oceanogr.* 75, 363-382.



- Sobarzo, M., L. Bravo and C. Moffat (2010), Diurnal-period, wind forced ocean variability on the inner shelf off Concepción, Chile. *Cont. Shelf Res.*, 30, 2043-2056, doi:10.1016/j.csr.2010.10.004.
- Song Y. and D. Haidvogel (1994), A semi-implicit ocean circulation model using a generalized topography following coordinate system. *J. Comput. Phys.*, 115, 228-248.
- Stewart, R. (2008), *Introduction to Physical Oceanography*. Department of Oceanography, Texas A & M University, Texas.
- Strub T. and C. James (2000), Altimeter-derived variability of surface velocities in the California Current System: 2. Seasonal circulation and eddy statistics. *Deep-Sea Res., II*, 47, 831-870.
- Strub, P., P. Kosro, A. Huyer, and C. Collaborators (1991), The Nature of the Cold Filaments in the California Current System, *J. Geophys. Res.*, 96(C8), 14743-14768.
- Strub P.T., M. Mesias and, C. James (1995), Altimeter observations of the Perú-Chile countercurrent, *Geophys. Res. Lett.*, 22, 211-214, doi:10.1029/94GL02807.
- Strub P.T., V. Montecino, J. Rutllant, and S. Salinas (1998), Coastal ocean circulation off western south America, in *The Sea*, vol. 11, *The Global Coastal Ocean: Regional Studies and Syntheses*, edited by A. R. Robinson and K.H. Brink, pp 273-314, John Wiley, New York.
- Vega, A., Y. du-Penhoat, B. Dewitte, and O. Pizarro (2003), Equatorial forcing of interannual Rossby waves in the eastern South Pacific, *Geophys. Res. Lett.*, 30(5), 1197, doi:10.1029/2002GL015886.
- Veitch J., P. Penven, and F. Shillington (2010), Modeling equilibrium dynamics of the Benguela Current system, *J. Phys. Oceanogr.*, 40, 1942-1964, doi: 10.1175/2010JPO4382.1
- Veneziani M., C. A. Edwards, J. D. Doyle, and D. Foley (2009), A central California coastal ocean modeling study: Forward model and the influence of realistic versus climatological forcing *J. Geophys. Res.*, 114, C04015, doi:10.1029/2008JC004774.
- Wentz, F.J., C. Gentemann, D. Smith and D. Chelton (2000), Satellite measurements of sea surface temperature through clouds. *Science*, 288, 847-850, doi: 10.1126/science.288.5467.847.